3D-printing and characterization of PEEK bioactive composites for craniofacial applications

Faisal Manzoor

Faculty of Computing, Engineering, and the Built Environment

Ulster University

Thesis submitted for the degree of Doctor of Philosophy

August 2022

I confirm that the word count of this thesis is less than 100,000 words

Table of Contents

List of Figures

List of Tables

Acknowledgments

Apart from my hard work, the success of my project depends upon the encouragement and motivation of many people around me. I take this opportunity to thank all those who have been helpful in the successful completion of this project.

Firstly, I want to extend my sincere gratitude to my supervisor Dr. Atefeh Golbang who guided and motivated me from time to time to accomplish this tough journey. I deeply appreciate her encouragement, invaluable advice, support, expertise, and knowledge which have made to complete my degree with a great experience. I would also like to send prayers to my second supervisor Dr. Dorian Dixon (Late) for his assistance and support. I am also thankful to Dr. Elena Mancuso who provided me with her valuable pieces of advice.

I would like to thank Prof. Eileen Harkin-Jones for providing me with this opportunity. I am thankful to Prof. Alistair for his kind support throughout this project. I would also like to acknowledge Dr. Adrian Boyd for providing me the trainings of XRD equipment and HA synthesis.

I am forever indebted to my family; my Mother, Father, Brothers, and Sister for their kind support during this journey. Special thanks to my wife and children (Sobaan and Mirha) for their understanding, showing endless patience, and tolerance when it was most required. Also, a bundle of thanks to my colleagues and friends here at Ulster University as well as back in Pakistan.

Finally, I would like to acknowledge Evonik for providing PEEK material, the North West Centre for Advanced Manufacturing (NWCAM) for their funding and Axial 3D company for their guidance.

Abstract

This research investigated the 3D printing of PEEK bioactive nanocomposites with Strontium (Sr) and Zinc (Zn) doped hydroxyapatites. Doped hydroxyapatites were synthesized by wet chemical precipitation method and incorporated into polyetheretherketone (PEEK) up to 30 wt.% and processed by a novel approach i.e., fused filament fabrication (FFF) 3D printing for the production of patient specific cranial implants with improved bioactivity and the required mechanical performance. PEEK nanocomposite filaments were produced via extrusion and subsequently 3D-printed using FFF. In order to further improve the bioactivity of the 3D-printed parts, the samples were dip-coated in polyethylene glycol-DOPA (PEG_{1000}-DOPA) solution. The printing quality was influenced by filler loading but was not significantly influenced by the nature of doped-HA. Hence, the printing conditions were optimized for each sample. Micro-CT and Scanning Electron Microscopy (SEM) showed a uniform distribution of bioceramic particles in PEEK. Although agglomeration of particles increased with increase in filler loadings. Differential Scanning Calorimetry (DSC) showed that the melting point and crystallinity of PEEK increased with an increase in doped-HA loading from 343 °C to 355 °C and 27.7% to 34.6%, respectively. Apatite layer formation was analyzed on the surfaces of 3D-printed samples after immersion in simulated body fluid (SBF) for 7, 14 and 28 days via SEM, X-ray diffraction (XRD) and Fourier Transform Infrared Spectroscopy (FTIR). The tensile strength and impact strength decreased from 75.1 MPa to 51 MPa and 14 kJ/m^2 to 4 kJ/m^2, respectively, while Young's modulus increased with increasing doped-HA content from 2.8 GPa to 4.2 GPa. However, the tensile strengths of composites remained in the range of human cortical bone i.e., ≥50 MPa. In addition, the mechanical strengths of the samples after 28 days immersion in SBF were measured. Water contact angle showed that the hydrophilicity of the samples improved after coating the 3D-printed samples with PEG_{1000}-DOPA. Hence, based on the results, the 3D-printed PEEK nanocomposites with 20 wt.% doped-HA is selected as the best candidate for the 3D-printing of craniomaxillofacial implants

Publications

1. Faisal Manzoor, Atefeh Golbang, Swati Jindal, Dorian Dixon, Alistair McIlhagger, Eileen Harkin-Jones, Daniel Crawford, and Elena Mancuso, '3d Printed Peek/Ha Composites for Bone Tissue Engineering Applications: Effect of Material Formulation on Mechanical Performance and Bioactive Potential', Journal of the Mechanical Behavior of Biomedical Materials, 121 (2021), 104601. https://doi.org/10.1016/j.jmbbm.2021.104601

2. Faisal Manzoor, Atefeh Golbang, Dorian Dixon, Elena Mancuso, Usaid Azhar, Ioannis Manolakis, Daniel Crawford, Alistair McIlhagger, and Eileen Harkin-Jones, '3d Printed Strontium and Zinc Doped Hydroxyapatite Loaded Peek for Craniomaxillofacial Implants', Polymers, 14 (2022), 1376. https://doi.org/10.3390/polym14071376

3. Swati Jindal, Faisal Manzoor, Niall Haslam, and Elena Mancuso, '3d Printed Composite Materials for Craniofacial Implants: Current Concepts, Challenges and Future Directions', The International Journal of Advanced Manufacturing Technology, 112 (2021), 635-53. https://doi.org/10.1007/s00170-020-06397-1

4. Faisal Manzoor, Atefeh Golbang, Alistair McIlhagger, Eileen Harkin-Jones, Daniel Crawford, and Elena Mancuso, 'Effect of Zn-NanoHA Concentration on the Mechanical Performance and Bioactivity of 3d Printed Peek Composites for Craniofacial Implants', Plastics, Rubber and Composites (2022), 1-7. https://doi.org/10.1080/14658011.2022.2108986

Abbreviations

Å	Armstrong
A	amperes
AD	after death
a.u	arbitrary units
β	beta
BC	Before Christ
HCO_3^-	bicarbonate ions
Cl^-	chloride ions
C	carbon
CAD	computer aided design
CAM	computer aided modelling
cm	centimeter
cm^2	centimeter square
C=O	carbonyl
Ca/P	calcium to phosphorous ratio
Ca^{+2}	calcium ions
°C	degree centigrade
CT	computed tomography
g	grams
≥	greater than and equal to
GPa	giga pascals
h	hours
OH	hydroxyl

HA	hydroxyapatite
HPO_4^{-2}	hydrogen phosphate ions
IR	infrared
ISO	international standards organization
kJ/m^2	kilo joule per meter square
kg	kilograms
kV	kilo volts
µ	micro
µL	micro liter
mA	milliamperes
mm/s	millimeter per seconds
Mg^{2+}	magnesium ions
MPa	mega pascals
mM	millimolar
mm	millimeter
ml/min	milliliter per minute
MRI	magnetic resonance imaging
nm	nanometer
N	newton
O	oxygen
PO_4	phosphate
K^+	potassium ions
cm^{-1}	per centimeters
RPM	revolutions per minute

SO_4^{2-}	sulphate ions
Na^+	sodium ions
Sr	strontium
Sr^{+3}	strontium ions
SBF	simulated body fluid
SrHA	strontium doped hydroxyapatite
STL	Standard Tessellation Language
θ	theta
TCP	tri calcium phosphate
T_d	degradation temperature
T_c	crystallization temperature
T_g	glass transition temperature
T_m	melting temperature
Ti	titanium
TRL	Technology Readiness Level
UK	United Kingdom
US	United States
USD	United States Dollar
vol.%	volume percent
wt. %	weight percent
w/w %	weight by weight percent
Zn	zinc
ZnHA	zinc doped hydroxyapatite

1 Chapter 1: Introduction

1.1 Overview

The human brain is a very sensitive and vital organ of the body which controls various body functions such as vision, breathing, hunger, memory and every process that regulates our body [1]. This sensitive organ is protected by a hard skull which is made up of various kinds of bones. The bones of the skull are tightly packed and strong enough to bear any impact forces. Every type of skull bone has different mechanical properties. The main purpose of the skull is to protect the brain from any kind of injury which usually takes place due to falls, road accidents, extreme sports, or anti-social behaviors [2]. Usually, the forces act during these kinds of injuries are impact forces and applied on a single point. For example, a collision between two persons during any sports related events or a road accident. Apart from injury, sometimes a planned defect is created during surgical procedures. In that case, the skull bone does not undergo impact forces and the forces strongly dependent on cutting tool speed depth of cut and cutting angle [3]. The human body can heal small fractures or loss part of the bone. However, if the size of the defect is greater than the critical size defect then the human body cannot heal it. Hence, an external material is required to repair that defect [4]. The surgical repair of the bone defect in the skull resulting from a previous injury or operation is known as cranioplasty. The history of cranioplasty dated back to 7000 BC. Since that time, various materials have been tried to repair the defects ranging from metals, gourds, animal horns and animal bones. Still, the surgeons have not found an ideal material which can fulfill all the requirements to replace craniofacial bone [5]. Various materials have been experimented with for that purpose, but each material has its own limitations. For example, metals are strong, but their mechanical properties mismatch with the bone and cause a stress shielding effect, ceramics are bioactive, however they are brittle and cannot be molded into complex shapes, and polymers are either not very strong or not bioactive. Scientists are investigating the polymeric composites to overcome the shortcomings and produce an ideal material that can mimic the properties of the human bone [6].

In the past few decades, polyether ether ketone (PEEK) has been considered a reliable candidate alternative to other materials for cranial and maxillofacial bone repair [7]. PEEK is a semicrystalline thermoplastic polymer with elastic modulus (3-4 GPa) much lower than Ti, biocompatible, radiolucent, and stable in sterilization with gamma irradiation [8]. However, its surface is hydrophobic due to the presence of aromatic rings and polyester functional group,

so it is a bioinert material and hence, does not offer adhesion to the surrounding tissues [9]. Hence, ideal biomaterial should have adequate mechanical properties as well as bioactive surface for integration. The bioinert property of PEEK can be altered by the incorporation of bioactive fillers such as hydroxyapatite or bioactive glass [10-13]. Hydroxyapatite (HA) is a synthetic bioceramic material which resembles chemically with the mineral part of the human bone [14]. Additionally, biological performance of HA can be enhanced by doping with other elements up to some limits which are already present in human bone and their amount vary with the tissue (i.e., bone, dentin, enamel) such as strontium (Sr), silicon (Si), magnesium (Mg), zinc (Zn), etc., in which each doped element in HA plays an important role in bone regeneration and biomineralization [15]. For example, Sr promotes bone growth and inhibit bone resorption [16], Si enhances bioactivity of HA and bone regeneration *in-vivo* [17], Mg enhances resorption of HA and is a key factor in the activity of several enzymes [18], Zn acts as a co-factor for several enzymes, promotes bone growth and have anti-bacterial properties [19].

PEEK and its composite implants have been traditionally fabricated using subtractive manufacturing techniques such as milling, injection molding and compression molding [20]. Since due to the high demand of PEEK and complexity of the implants, additive manufacturing (AM) has started to be used as a forming process for fabricating PEEK components. AM which is also referred as three-dimensional (3D) printing or rapid prototyping, is a manufacturing technique in which an object is formed after depositing material layer-by-layer [21]. AM is a revolutionary technology which provides excellent degree of design freedom with high dimensional accuracy i.e. it can produce complex shapes which are beyond the limit of conventional technologies [22]. Among different types of AM, PEEK and its composites can be processed either by selective laser sintering (SLS) or fused filament fabrication (FFF). SLS has high production cost, low penetration power and concentrated beam of laser restrict its use to construct large areas or laminates. On the other hand, FFF is most popular and fastest growing technology which can produce large size medical implants. FFF is considered as an alternative method for processing PEEK parts [23]. Fused filament fabrication (FFF) also referred as fused deposition modelling (FDM), technically there is not any difference between FDM and FFF. FDM is a trademarked name which is patented by Stratasys while FFF is a non-trademark name [24]. FFF/FDM is one of the most popular type of additive manufacturing (AM) due to its ease to use, low manufacturing cost, less material waste, environmentally safe materials, no need of supervision and ability to manufacture complex topologies [25, 26]. The technology has been serving in various discipline of science ranging from aerospace to

biomedical due to its adaptability and materials commercial availability [27]. This technology has revolutionized in healthcare sector where personalized implants are needed with high accuracy particularly in cranio-maxillofacial defects repair [28].

The maturity of the technology is determined by the Technology Readiness Levels (TRL). There are 9 TRLs where TRL1 is the lowest and TRL9 is the highest. TRL1 phase is the starting with an idea and the hypothesized tested in phase two which is consolidated in phase three. The proof-of-concept phases are four and five in which PoC is illustrated *in vitro/in vivo* conditions and additional advancement are done to evaluate the prototype's performance. The preclinical evaluation is completed in phase six. TRL phase eight is the technology transfer phase. The clinical evaluation phase starts at TRL phase eight, and at this stage, the device production and certifications are submitted and approved. Finally, TRL phase nine is a commercialization phase in which the technology is fully available [29]. Considering these phases, the current study lies in TRL phase eight in which clinical evaluation of 3D printed orthopedic implants has been completed. The TRL diagram which shows the description of each TRL is given below in Figure 1:

Figure 1 Technology Readiness Levels (TRL) diagram

This project was funded by the EU's INTERREG Programmes VA, total funding was €8.7m through the North-West Centre for Advanced Manufacturing (NWCAM). The partner universities involved were Ulster University, Institute of Sligo, Letterkenny Institute of Technology and University of Glasgow. This project was collaborated with a local company named Axial3D. Axial3D makes patient-specific 3D models for surgeons to visualize the defect physically and plan the surgery accordingly.

1.2 Aims and objectives

The overall aim of the project is to evaluate the 3D printability of bioactive nanocomposites of PEEK polymer. Furthermore, to study the effect of weight percent of bioceramic particles on mechanical properties and bioactivities of PEEK nanocomposites. The successful 3D printing of bioactive PEEK nanocomposites can be used for manufacturing patient-specific craniofacial medical implants. In order to achieve this aim, several core objectives were identified which have been listed below:

- Synthesis of HA, SrHA and ZnHA by wet chemical precipitation method
- Physico-chemical characterizations of raw materials
- Preparation of feedstock filaments for 3D printing via extrusion
- Investigate the distribution of bioceramic particles and study the thermal behaviour of nanocomposite filaments
- Optimization and 3D printing of PEEK nanocomposite samples
- Investigate the distribution of bioceramic particles in 3D printed parts
- Determine the effect of weight percent of bioceramic particles on *in-vitro* bioactivities
- Determine the effect of weight percent of bioceramic particles and apatite layer formation on the mechanical properties

1.3 Thesis structure

The structure of the thesis has explained below:

Chapter 1 briefly explains the introduction of the thesis including aims and objectives

Chapter 2 gives the detailed literature review covering history of cranioplasty, materials used in the past, limitations of conventional and advantages of latest technologies

Chapter 3 explains the materials and methods used in this thesis

Chapter 4 presents the detailed characterizations of raw materials

Chapter 5 gives the properties and characterizations of feedstock filaments

Chapter 6 explains the characterizations of 3D printed parts

Chapter 7 gives the conclusions and recommendations for future work

Chapter 8 & 9 contain supplementary information and references

2 Chapter 2: Literature review

In the human body, the head is the most important part and must be protected effectively [30]. The skull is a bony structure of the human skeleton and its function is to protect the brain, provide a cavity to the brain and provide structural support to the facial bones [31]. An adult human skull is made up of 22 bones and can be categorized into the cranium and facial bones. All bones are joined and provide a packed structure with very little movement except the mandible. The human braincase is formed with eight bones including two parietal bones, two temporal bones, one ethmoid bone, one frontal bone, one occipital bone and one sphenoid bone. Other fourteen bones support the facial bones and form splanchnocranium [32]. There are two types of craniofacial defects arise. Firstly, a defect occurs due to trauma and secondly, a defect created by cutting the bone for a planned surgery. In former case, a complex shaped defect is produced when a point impact loading occurs during the extreme events such as a collision during sports, road accident or fall [33].

In later case, the defects are created intentionally to repair cranial and facial defects for cosmesis and functionality [34]. Its objective is to restore the structure and function of the skull, promoting brain protection and optimizing cerebral hydrodynamic conditions and aesthetics [35-37]. Approximately, 69 million individuals suffer from traumatic brain injury every year around the world which is a great economic burden [38]. There are almost 2.5 million cases of traumatic brain injury annually in the European Union and this is a foremost cause of death and disability [39]. In England and Wales, around 1.4 million and in United States 1.7 million patients per year visit hospital due to head injury and it is the most common cause of death under the age of 40 years [40]. In 2016 only, 74,242 cases for traumatic head injury were reported in England [41]. The global Craniomaxillofacial devices market size was valued at USD 2.45 billion in 2018 and according to a new report published in May 2019 by Grand View Research, Inc. that market size is expected to reach USD 3.47 billion by 2030 [42]. The market is competitive in nature as the manufacturers are involved in new product developments to increase their market penetration. There is still no ideal implant available to the date in the market which would fulfil all the requisites for craniofacial surgery. Available implants do not possess adequate biocompatibility and show poor adhesion with the surround tissue.

2.1 Background

2.1.1 History

In the past, the skull bone was opened or pierced for healing or diagnosis. This process is called trephination and it is considered the oldest surgical procedure used by ancient civilizations [43]. The history of trephination of cranial vault is very old i.e. 10,000 BC and one ancient site found in France, burials included 40 out of 120 instances of trephination from around 6,500 BC [44]. In primitive cultures, trepanation was widespread around the world throughout time, and performed during Neolithic Period in Europe, the pre-Columbian period in Andean South America, and some coexistent Pacific and African tribes. Craniofacial surgeries were performed by many ancient civilizations such as Incas, Asians, North Africans, British and Polynesian populations with evidences dating back 7,000 BC [34]. Around 600 BC, an Indian practitioner Sushruta briefed operations for restructuring the nose [45]. Surgeon Paulus Aengineta (625 to 690 AD), during Roman Empire, described the revolutionary surgical procedures to repair nasal disorders and fracture in jawbone [46]. However, the first surgery in medical literature was reported by Fallopius and Petronius in 16th century, they used gold plates to repair cranium defects [47]. Bovine, canine and rabbit bones were also experimented for reconstruction of human bone defects [5]. Example of trephined skull is shown in Figure 2 below.

Figure 2 Trephined Skull discovered from late Iron Age cemetery of Münsingen-Rain in Switzerland [48]

2.1.2 Materials used in craniofacial surgery

Cranium defects result mainly from trauma and tumor surgery, but also from congenital defects, and usually create aesthetic and functional disturbances to the patients [49, 50]. The skull implants can range from a few cm^2 to larger than 100 cm^2. The implants should be designed to follow the contour of the defect and have fixation plates to attach to the surrounding skull bone. Unilateral implants are easy to design as the unaffected side can be used as a template for designing implant while biaxial implants are difficult to design as contour information is missing and mirroring is not possible. The thickness of bone is variable, hence anatomical location of the defect dictates variation in implant design [51]. Poukens et al. [52] have been classified cranial defects into six categories based on the complexity of designing, size and whether orbital rim is involved. Type I, II, II implants do not involve orbital rim while Type IV, V, VI implants involve orbital rim. The implants whose area is less than 5 cm^2 is Type I implants, greater than 5 cm^2 but less than 100 cm^2 are Type II implants, greater than 100 cm^2 are Type III implant, if area is less than 5 cm^2 with orbital involvement it is Type IV and Type V implants have area larger than 100 cm^2. Type VI implants have area greater than 100 cm^2 with crossing midline of the skull. Cranium implants are plates or meshes with high toughness to protect brain from the environmental forces and stresses. Puncturing holes in plates is a general practice to relieve pressure of brain and prevent hemorrhage [52]. The mechanical properties of cranial bone depend on the anatomical structure, bone type, gender and age group [53]. Human bone is a composite of collagen and hydroxyapatite [54]. Generally, tensile strengths of cortical bone in longitudinal and transverse directions are 65 MPa and 50 MPa, respectively. The compressive strengths in longitudinal and transverse directions are 170 MPa and 50 MPa, and Young's moduli in longitudinal and transverse directions are 15 MPa and 10 MPa, respectively [55-58]. Julie et al. [59] measured the bending strength of right parietal, left parietal and frontal bones. It was reported that right parietal, left parietal and frontal bones had bending strengths 82.98 MPa, 78.15 MPa and 102.60 MPa, respectively.

Bone grafting is the procedure to fill the gap or missing craniofacial part created after injury. It can be performed by various ways like autograft, allograft, alloplast and xenograft. *Autografts*, still considered as gold-standard for bone repair, are harvested from same individual but from different site, resulting another injured site so it is mostly not preferred. In *allografting*, bone is taken from other individual of same specie but there is always risk of infection or immunological reactions. *Xenografts* are taken from different species so there are high chances of immune rejection which limit its use while *Alloplast* are synthetically made

materials either metals, polymer, ceramics or composites which are used as bone scaffolds [60-62].

Autografts have been used historically for craniofacial defect repair due to their quite positive immune response, osteogenic cells retention and assisted / enhanced healing activity [63, 64]. They are still considered as gold standard for repair, although injury at donor site, costly surgeries, high probability of graft resorption, chances of infection at donor and/or receptor site, low availability of graft and extended operation times are the major limitations for their use [65-67].

Throughout the years, surgeons have attempted to repair craniofacial defects with animal tissue. In 1668, Van Meekeren successfully performed bone grafting from canine into human which was opposed due to the ethical issues [68]. After that bone grafts from rabbit, eagle, ape, calf and goose have been grafted in humans but they have high infection rate. Bone was often boiled to make it porous prior to placement into patients. Marchand et al. in 1901, reported that animal horns could be accepted by human tissues. Buffalo horn, ox horn and ivory were applied in human tissues and found satisfactory results, although good success with autografts with low infection rates provided negligible justification for further xenograft applications [68].

In 1915, Morestin first reported the use of cadaver cartilage allograft for craniofacial repair [69]. It was thought cartilage would work because it was moulded successfully and resistant to infection. However, it was realized soon that cartilage was not strong enough and not suitable for cranial bone repair. In 1917, Dambrin and Sicard investigated potential of cadaveric skull for cranial reconstruction. The collected bone was treated with sodium carbonate, alcohol, xylol and ether and heat sterilized before implantation. This diminished the thickness of bone, with only the outer layer remaining, which then further made porous to use [36]. Due to bone resorption and high risk of infection, cadaver skull has been having limited application in craniofacial reconstruction. Autologous bone grafts have gained more importance than allografts because of the above-mentioned complications. However, lack of their availability restricted its applications.

In the last century, the era of world wars, non-biological prostheses became prevalent for bone repair. In World War I, metals such as silver and gold were considered best candidate while in World War II, there was a preference for titanium and is currently the basis of several modalities of cranial reconstruction [70]. Since 1950's, after the discovery of acrylic, non-metallic prostheses became preferred choice for non-load bearing applications in surgery.

Acrylic plates were prepared by two tedious steps, firstly mould had to be prepared to cast plate and then inserted into the cranial defect [71]. In 1954, Spence developed a single stage process in which poly (methyl methacrylate) (PMMA) plates were synthesized within the defect by polymerising PMMA powder with liquid monomer. The resulting reaction allowed PMMA to become soft and easily fit to the defect [72]. There were some disadvantages with this process such as exothermic reaction and non-sterile powders. Brittleness is the limitation of acrylic resins which results in the fracture of plate into fragments. These fragments can be embedded into the skull. In 1989, Malis proposed titanium mesh for cranial defect repair which had good strength and malleability [73]. The use of acrylic has been improved much in current practices due to the advancements in computer aided design (CAD) and computer aided modelling (CAM). Metallic implants are used to manufacture by mould casting [74], forging [75], lost-wax method [76] and hot isostatic pressing via powder metallurgy [77]. Hence, bioactive coatings were used to improve the bioactivity of the implants surface [78, 79]. High temperature and high pressure were applied to forge metals into implants made it unsuitable process [75]. Porosity could be induced on surface of implants with the help of powder metallurgy to enhance bone growth [79]. These techniques to be proved effective at that time, but they lacked precision control, pore size and distribution control and were not cost effective [74, 75, 77]. Thermoplastic polymer implants such as polylactic acid (PLA), poly glycolic acid (PGA), poly (lactic-co-glycolic) acid (PLGA) are used to manufacture by injection moulding, hot moulding, compression moulding and extrusion [80]. Limitations of these techniques are: they lacked variety, precision control, size limitations and expensive [81].

Nowadays, the implants are manufactured with biocompatible metals like titanium, polymers like polyetheretherketone (PEEK) and poly (methyl methacrylate) (PMMA) or bone substitutes like synthetic hydroxyapatite (HA). Titanium is a biocompatible metal, is used for craniofacial repair and implants can be constructed by additive manufacturing types i.e. Selective Laser Melting (SLM) and Electron Beam Melting (EBM) technology [82]. Mechanical properties of PEEK resemble with bone with advantage of low weight and radiolucent properties. Its implants for craniofacial repair are made from FFF and SLS.

The ideal craniofacial implant has following characteristics [83]:

- Geometrically fit and does not allow any gap
- Radiolucent
- Strong

- Bioactive
- Resist infections
- Sterilizable
- Easy to shape
- Ready to use
- Cost effective

Example of PEEK craniofacial implant model is shown in Figure 3 below.

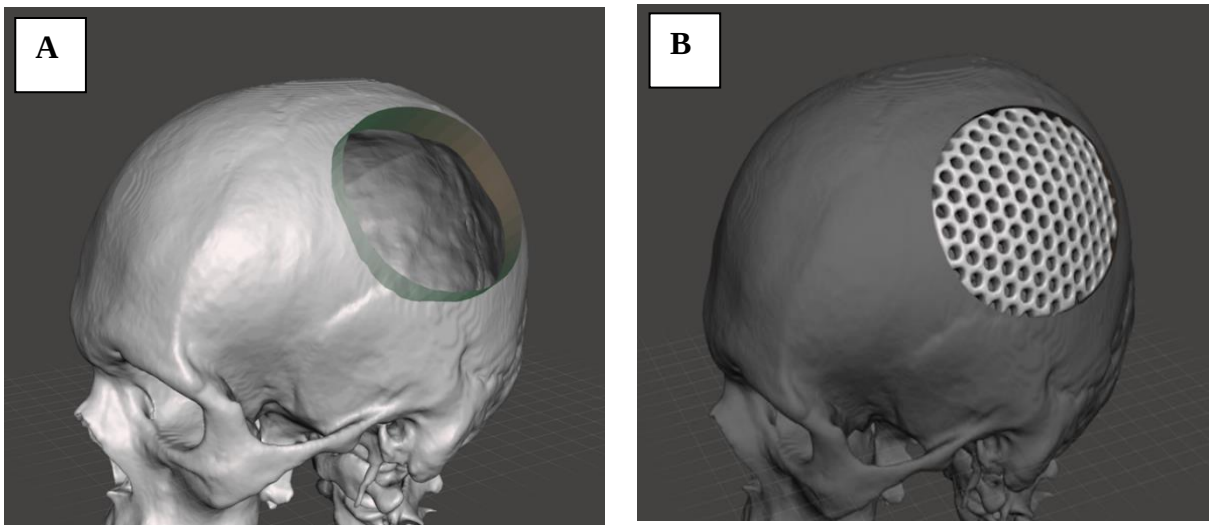

Figure 3 An example of PEEK craniofacial implant model, A) a skull model with a cavity, B) cranial implant fit into the skull cavity

2.1.3 Classification of Biomaterials

A biomaterial can be defined as “any material used to make devices to replace a part or a function of the body in a safe, reliable, economic and physiologically acceptable manner” [84]. Biomaterials for craniofacial repair can be either metals, polymer, ceramics or their combinations. They are described in detail below.

2.1.4 Metals

Metals such as aluminium, gold, silver, titanium and their alloys, were among oldest materials used to repair craniofacial defects, though many are abandoned today. Aluminium caused infectious complications and induced epilepsy in patients who had cranioplasty with aluminium [85]. Although, gold has low complication rates, but it is very expensive. Silver

having poor mechanical properties and high oxidation, made it unfavourable. Surgical titanium grade 5 (Ti-6Al-5V), usually referred as titanium, is still used in cranium fixation devices (like screws, plates), solid plates or mesh. Titanium is generally considered as corrosion resistant but there is evidence that trace amounts are released over time which may elicit a subtle immunologic response [86]. Titanium and its alloys have been widely used in human bone replacement surgery due to its biocompatibility, high corrosion resistance, good machinability and tremendous mechanical properties. Though clinical applications of titanium has been identified in 1966 [87] but in 1983 Branemark [88] pointed out the superior biocompatibility and mechanical properties of this metal. The only mismatch is the elastic modulus, as elastic modulus of titanium alloys is approximately 110 GPa which is much higher than cortical bone (10-30 GPa). This mismatch leads to stress shielding effect in the bone [89-91]. Stress shielding effects occur from shear stresses due to the mismatch of mechanical properties of bone and the implant [92]. The stress shielding effect can be minimized in metallic implants by lowering the Young's modulus, it can be done either by increasing beta phase as compared to alpha phase in Ti or making the implant porous. Titanium alloys with higher beta phase have good ductility and corrosion resistance [93, 94] which decrease the probability of ion release in blood. Other way to overcome stress shielding effect, titanium and its alloys are made porous [95, 96]. Conventional techniques for making porous metal implants are metal deposition, liquid metal solidification and solid metal sintering [97]. These techniques are suitable for manufacturing porous implants, but they do not have control over pores i.e., shape, size and distribution. Through additive manufacturing, pore size, shape and distribution can be controlled precisely [98-101].

Stainless steel had been used for craniofacial implants [102]. Austenitic stainless steels have been used in orthopaedic applications due to their non-magnetic nature. Biomedical grade of stainless steel is 316L (ASTM F55 and F138) which is an alloy of iron with chromium and nickel. Its major shortcoming is that it releases nickel and chromium ions in blood due to pitting and stress cracking corrosions [103] so it is rarely used now a days. The release of these ions results complications in the body like discomfort, skin changes, swelling etc. [104]. Mechanical irritation or insufficient perfusion of the overlying scalp flap (micro-plating and screws), may lead to infection, inflammation, seroma or implant fenestration through scalp [105]. The other factors that limit the use of metals in craniofacial surgery include their thermal conductivity, radiopacity and high cost [106].

2.1.5 Ceramics

Ceramics such as hydroxyapatite (HA), beta tricalcium phosphate (β-TCP) and their composites possess the similarity in chemical composition as of natural bone, and are considered favourable biomaterials for bone repairing [107-109]. Hydroxyapatite, chemically identical to the bone apatite [Formula= ($Ca_{10}(PO_4)_6(OH)_2$; Ca/P=1.67], is a member of orthophosphate family which has been investigated and used most widely. The structure of HA has been given in Figure 4. It is used to coat on inert implants, porous granules for defect filling, synthetic bone grafts and hard tissue scaffolds. Synthetic HA can be prepared using various methods such as precipitation technique, sol-gel approach, hydrothermal method, coral conversions and multiple emulsion technique. Additionally, bioactive glasses are also used as bone filler material. Making layer of mineralized HA is a unique characteristic of bioactive glasses which enhance chemical bonding with the bone [110]. Due to their excellent biological performance, these biomaterials have been applied for clinical bone defect repair [111, 112]. Due to its inferior mechanical properties, it is being used for small size defects only [113]. Moreover, anatomical shape and structural limitations for variable defects size making them unfit for clinical use where the critical-size defects are large [114].

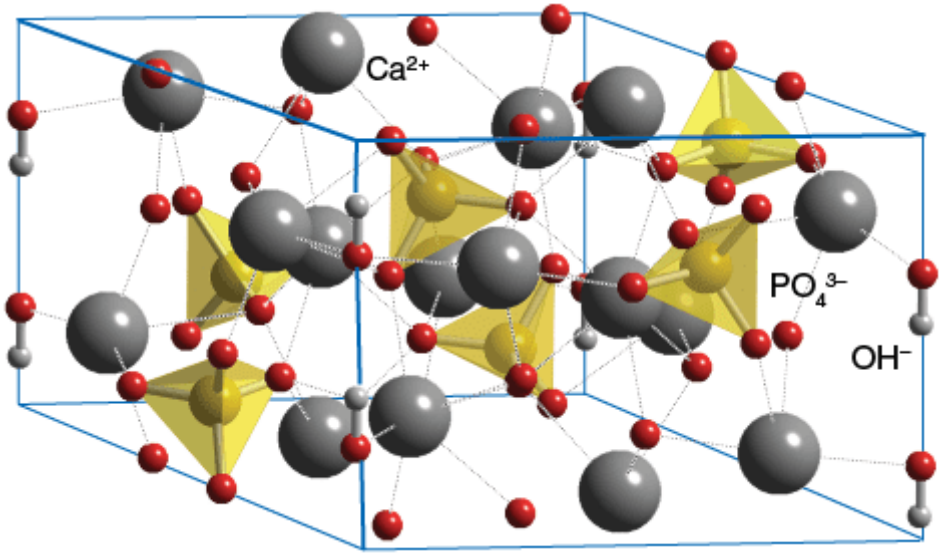

Figure 4 Structure of hydroxyapatite unit cell [115]

2.1.6 Polymers

In past, metals and their alloys have been used for many years for the production of medical and dental implants due to their high strength and high corrosion resistance; in the case

of some alloys such as titanium due to the formation of passive oxide layer on their surfaces. Particularly, their applications for the provision of range of load bearing medical devices is well established such as knee replacement, hip joint, fracture fixation and spinal stabilization. Even though these metals are classified as biocompatible, however they do not inherent bioactive properties, also release harmful metallic ions in blood, produce stress shielding effect, radiopaque, etc. [116]. Although, many attempts have been made to increase the bioactivity of metallic implants by coating with bioceramic materials such as calcium phosphates. Nevertheless, they are still not very successful due to the high percentage of implant failure caused by loosening or stress shielding which in most cases required revision surgeries to remove and replace those implants, causing a lot of trouble to the patients. On the other hand, polymers have few advantages over metallic implants such as polymers are radiolucent, strong, insulator, passive and inexpensive. Polymers that have been widely used for craniofacial defects repair are polymethylmethacrylate (PMMA), polyetheretherketone (PEEK), polyetherketoneketone (PEKK), porous polyethylene (PE), etc. There are few challenges that often arises for these polymers such as PMMA is bioinert, brittle, lack osteoinductive property and produce large heat when cast into cement [117, 118], inadequate cooling may damage bone or surrounding tissue. Porous PE may allow soft tissue ingrowth and collagen deposition through pores [119-121] however, it is too soft as compared to PMMA so it is only used in small defects [122, 123]. Among various potential polymers available for manufacturing medical implants, PEEK is gaining attention to be used as an orthopedic implant material for knee, shoulder, hip and spinal repair. Numerous studies have been demonstrated and documented the successful clinical applications of PEEK due to its various advantageous inherent properties such as mechanical properties, radiolucency, stable in gamma sterilization, processibility. PEEK has high strength to weight ratio and its modulus (3-4 GPa) is comparable to human bone (~6 GPa) therefore reducing the stress shielding effect and subsequently lowering the chances of implant loosening which is associated with other conventional materials especially with metallic implants. PEEK is considered as a high-performance thermoplastic implant due to its stability, resistance to degradation and resorption in in-vivo even in the presence of lipids [124]. The chemical structure of PEEK has been given below in Figure 5.

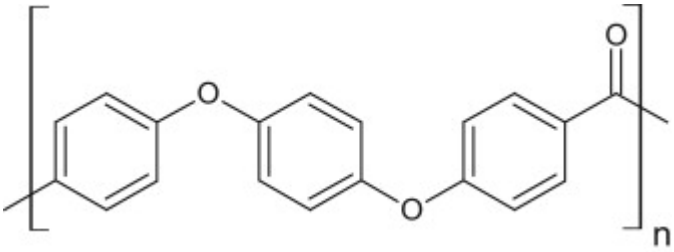

Figure 5 Chemical Structure of PEEK [125]

In recent days, the imaging technologies such as X-rays, MRI and CT have become significantly valuable for monitoring purposes, PEEK has exhibited various benefits over the use of conventional metallic implants such as Ti. As Ti is a radiopaque, interacts with X-rays and makes imaging difficult. On the other hand, PEEK is a radiolucent and does not interfere with X-rays so provides opportunity to investigate tissue-implant interaction, repair and growth. Moreover, PEEK being non-magnetic material, is suitable to use in MRI imaging without creating any trouble, thus making implant monitoring easy. Furthermore, PEEK does not produce imaging artifacts which is a common shortcoming of metallic implants, they produce shadowing during CT scans and hence make the imaging unclear to investigate [126, 127].

According to ISO 17665-1:2006, medical implants must be sterilized in order to inactivate the microbiological contaminants which may cause complication such as infection after implantation [128]. After sterilization process, the properties of designed materials for implantation in the human body should not be altered. However, some sterilization techniques may alter the chemical and mechanical properties of the material. As compared to other polymeric implant materials, PEEK can maintain stability after various sterilization techniques such as ethylene oxide, hot steam and gamma radiation [129]. It can be sterilize thermally as well as by irradiation and no changes in the mechanical properties were noted even after multiple exposure of the processes [130]. PEEK does not produce any free radical in the gamma radiation sterilization process while other polymers do [131]. It can be sterilized repeatedly which is ideal for medical implants [132, 133]. Furthermore, PEEK is a semi-crystalline polyaromatic thermoplastic polymer and its chemical formula is $(–C_6H_4–O–C_6H_4–O–C_6H_4–CO–)_n$. It was commercialized in 1980 while in 1998, it was proposed as a material for biomedical applications by Invibio Ltd. (Thornton-Cleveleys, UK). PEEK-OPTIMA, a medical grade of PEEK satisfying the requirements of Food and Drug Administration (FDA), was introduced in the same year as a long-term implantable material by Victrex PEEK business

(Imperial Chemistry Industry, London UK) and has been used in various clinical applications such as craniofacial reconstruction, total joint replacement and spinal cage fusion. PEEK or its composites can be processed by different techniques like injection moulding, hot pressing or additive manufacturing. Starting raw material can be either powder or pellets, can be used directly or after making filament for additive manufacturing. PEEK LT1 grade is a medical grade and often contains different amount of hydroxyapatite or beta-tricalcium phosphate. It can serve as an alternative to conventional ceramic or metallic implants. PEEK is a chemically inert polymer, soluble only in 98 % sulfuric acid, and insoluble in all conventional solvents at room temperature.

At room temperature, PEEK is sparingly soluble in water i.e., only 0.5 w/w%. Its elastic modulus (3-4 GPa) resembles with the human cortical bone (7-30 GPa). Its glass transition temperature is 143 °C, melts at 334 °C and crystallization temperature is 345 °C. PEEK has properties like strength, stiffness and radiolucency comparable to the cortical bone [134]. Due to its inert nature and hydrophobic surface, its binding ability with surrounding soft tissue is very low [135, 136]. PEEK is non-allergenic and has high heat and gamma ray tolerance, allowing freedom for sterilization [137]. It remains stable and shows negligible interaction with electron beam and gamma radiations. Li et al. [138] reported that the free radicals produced after treating PEEK with gamma radiations (600 kGray), have lifetime less than 20 minutes. Therefore, after gamma sterilization, secondary irradiation of PEEK is not required. Radiographic assessment of PEEK through MRI is easy because of its natural radiolucent properties. Due to its radiolucent property, bone remodelling, resorption and integration with the implant can be easily monitored after surgery. The combination of these properties of PEEK has made it a suitable candidate in bone tissue engineering.

As, pure PEEK is a bioinert material and offers no adhesion to the surrounding soft tissues. Its bioactivity can be increased by number of ways like making surface rough, inducing porosity, surface treatments and making its composites with suitable bioactive materials. Many researchers have reported various methods to improve its bioactivity which is achieved by adopting different routes [139].

2.1.7 Composite biomaterials

Composite materials are composed of two or more materials, in the form of polymer-polymer blends, or polymer-ceramic mixtures which are not chemically bonded [140]. Furthermore, composite biomaterials can capitalize on the advantages of each component when

properly balanced; for example, integration with poly(lactic-co-glycolic acid) can improve brittleness linked with bioceramic materials alone [141]. PEEK has good mechanical strength close to the bone, but it is bioinert while hydroxyapatite is bioactive ceramic, but it is brittle. Recently, efforts have been made to enhance the fixation mechanism between the implant and tissue. The best way to do that is by making PEEK bioactive so that it can attach with the surrounding tissue. In order to improve the bioactivity of PEEK, bioactive material such as hydroxyapatite or doped hydroxyapatite is used either directly mixing with it or coated on it. The bioinert nature of PEEK can be altered either by the incorporation of bioactive fillers such as hydroxyapatite, bioactive glass [10-13] or by coating with a suitable material [142-144]. Hydroxyapatite (HA) is a synthetic bioceramic material which chemically resembles the mineral component of human bone [14]. Additionally, the biological performance of HA can be enhanced by doping with other elements, such as strontium (Sr), silicon (Si), magnesium (Mg), and zinc (Zn), which are present in human bone in various amounts depending on the type of tissue (i.e., bone, dentin, enamel). These doped elements play an important role in bone regeneration and biomineralization [15]. For example, Sr promotes bone growth and inhibits bone resorption [16], Si enhances the bioactivity of HA and bone regeneration in-vivo [17], Mg enhances HA resorption and is a key factor in the activity of several enzymes [18], while Zn acts as a co-factor for several enzymes, promotes bone growth and has anti-bacterial properties [19]. Additionally, PEEK has been coated with various materials to improve its hydrophilicity [145-147]. A compound, l-3,4-dihydroxyphenylamine (DOPA) has exceptional adhesive characteristics and it produces biocompatible hydrogel when conjugated with polyethylene glycol (PEG) [148]. The structure, synthesis and characterisation of the compound used (PEG_{1000}-DOPA) for coating the 3D-printed PEEK and PEEK nanocomposites in this study have been described in detail elsewhere [143]. In brief, PEG_{1000}-DOPA is a linear homo-bifunctional oligo(ethylene glycol) with Mn = 1000 Da and catechol-modified chain-ends, from the reaction of a hydroxy-terminated PEG_{1000} precursor with l-DOPA.

Bioinert materials such as stainless steel, polyethylene (PE) etc., are known as “first generation” biomaterials while the materials aiming to interact beneficially with the body termed as “second generation” biomaterials and the bioactive as well as bioresorbable materials are termed as “third generation” biomaterials. HAPEX™ is a first commercially available “second generation” biomaterial which is a composite of PE containing 40 vol% HA. Due to its poor mechanical properties, it is only used as mid-ear implants [149]. The commercial materials containing PEEK as a matrix are available for making orthopedic implants by

Invivio® such as PEEK OPTIMA® Natural, PEEK OPTIMA® HA Enhanced, PEEK OPTIMA® carbon fiber Reinforced and PEEK OPTIMA® carbon fiber Ultra-reinforced. PEEK OPTIMA® Natural have been used widely and utilized in approximately 15 million medical devices. However, it is bioinert and does not offer adhesion to the surrounding tissue. Additionally, PEEK OPTIMA® carbon fiber Reinforced and PEEK OPTIMA® carbon fiber Ultra-reinforced are reinforced with short and continuous carbon fibers, respectively. However, they are also bioinert. On the other hand, the material PEEK OPTIMA® HA Enhanced contains dispersed HA and shows bioactivity in sheep model, hence offer a suitable material choice for making PEEK/HA bioactive medical implants [150]. However, in this study, 3D printing of PEEK with doped HA has been attempted. The role of various elements in the bone formation has been reported in the next section.

2.1.8 Role of elements in hydroxyapatite substitution in bone formation

Human bone is a composite of mineral bioapatite and collagen. Mineral phase is mainly hydroxyapatite, but it also consists of minor groups and elements (CO_3, HPO_4, Na, Mg) and trace elements (Sr, K, F and Cl) up to ppm level [151]. Their concentration varies among tissue type (bone, enamel, dentin), anatomical sites and type of bone [152]. These groups and elements play an important role in biochemical reactions linked with bone metabolism [153]. Age is also a factor which show compositional variations. These elements show a significant variation in bone with age for example CO_3 and Na concentrations increase with the age, however, concentrations of Mg, Cl and K decrease with age. Skinner [151] proposed crystallochemical formula for hydroxyapatite as $(Ca, Na, Mg, K, Pb, Sr)_{10}.(PO_4, CO_3, SO_4)_6.(OH, CO_3, F, Cl)_2$.

There are number of methods are reported to substitute ions in hydroxyapatite synthetically. HA substitution is important because each element has effect on HA crystal lattice and hence affects its rate of biodegradation. Moreover, some of them influence biological properties and hence affect the healing process.

Carbonates substitution lead to decrease in a-axis and c-axis of HA and hence making it less crystalline and increasing its solubility and bioactivity [152, 154]. Magnesium is an essential element in body because it plays an important role in the activity of various enzymes. Magnesium substitutes calcium in HA and is responsible for reducing the c-axis in HA lattice. It decreases the crystallinity of HA by inhibiting HA nucleation and thus destabilizes its structure. The solubility of MgHA is high because of its low crystallinity than stoichiometric

HA. In bone, Mg has significant effect on metabolic activity and growth, by influencing osteoblasts and osteoclasts. Hence, limited amount of magnesium in body causes osteopenia or fragile bone [155].

Fluoride (F) replaces hydroxide (OH) in HA and causes it to contract a-axis and c-axis parameters of lattice structure but the lowering magnitude in case of c-axis is small. Fluoroapatite and HA structures are very similar which result fitting of smaller F ion more precisely into the F/OH channels. Thus, giving lattice a strong symmetry due to that reason it is more stable and less soluble. F ions favour cell attachments but its low solubility results in low availability of Ca ions so retarding cell proliferation. Due to its stable structure it is considered as an anti-osteoporotic agent [152, 156].

Strontium (Sr) can be introduced in HA by both ways i.e., ionic substitution and ion exchange. The concentration of strontium plays a vital role for Ca. Large amount of Sr enhance crystal size and crystallinity while lower amounts decrease crystallinity and reduce crystal size, hence high concentration distorts crystal lattice which results in increased solubility. It is observed that the solubility can be increased further when it is co-substituted with carbonated-HA (CHA) as compared to pure HA. Incorporation of Sr also increases the mechanical strength of bone and referred as anti-osteoporotic agent [152, 153, 157]. Sr base drug i.e. strontium ranelate, has been used to reduce osteoporosis activity of bone, it supresses osteoclast activity by promoting osteoblast activity [152, 153, 158-161]. However, the drug was discontinued in 2017 due to the adverse health effects [162, 163]. In-vivo ability of strontium to support bone formation is reported by many researchers [157-159, 164]. However, higher concentration of Sr has shown various side effects in human body [165-168]. Aimaiti et al. reported that the optimum amount of Sr (25-500 µM) promoted the osteogenic differentiation of human adipose-derived stem cells (hASCs) while higher concentration (1000-3000 µM) significantly inhibited osteogenic differentiation of hASCs [169].

Silicon (Si) replaces phosphate group of HA in the form of silicate $(SiO_4)^{-2}$. This silicate precipitates out at the grain boundaries of apatite crystallite making apatite fine and thus promoting amorphous phosphate which decreases its crystallinity, thus increases its ability to be bioresorbable [153]. Significant biological effects have been reported in bone regeneration and in-vivo testing even at very low concentrations i.e. Si=1 wt.% [170].

Zinc is a trace element present in bone which replaces calcium and thus inhibits the crystallinity. It plays important role in body, even in a trace amount, it acts as co-factor for

various enzymes, it affects the metabolism activity of nucleic acids and favours bone formation and regeneration by supporting the osteoblasts activity and lessening the osteoclast activity [152, 153]. The normal concentration of zinc in serum is 10 to 130 microgram/deciliter [171]. However, its excess amount shows high toxicity to osteoblast cells [172-178]. The daily recommended zinc intake for an adult is 15 to 40 mg [179, 180]. A higher level of zinc inadvertently reduces the level of copper, copper deficiency may lead to anemia, neutropenia, osteoporosis and bone fracture [181]. Manganese is also present in trace amount, and it inhibits the crystallinity of apatite. Its different concentrations affect the morphology of HA and thus alter bioactivity. Manganese plays a vital role in bone regeneration and its co-substitution with carbonate has positive effect on osteoblasts activity [182, 183].

2.1.9 Additive manufacturing in medicine

The conventional forming techniques for metallic and polymeric implants had numerous limitations including variety, geometry, size and cost. In the past, manufacturing of complex shaped craniofacial polymeric implants was a big challenge but thanks to additive manufacturing technology by which intricate shapes can be produced with great accuracy and precision especially patient-specific implants which not only save time but also eliminate many complications which arise due to mismatch of craniofacial implants to the bone [184].

Additive manufacturing (AM), also referred as 3D printing, is a modern manufacturing technique by which objects are manufactured layer upon layer. The most complicated and complex geometries which are beyond the range of conventional techniques, can be fabricated by 3D printing [185]. A lot of research is going-on to make it more efficient and beneficial for all scientific areas. By taking patient specific computer tomography data, commercial providers manufacture implants externally. Due to unique anatomy and variety of defects, reconstruction of bone implant is very challenging, however, Computer Aided Design (CAD) combination with AM technology, patient specific implants can be fabricated with great precision and in very short time. Shorter time thus minimizing patient stress and reduce the healing time. Furthermore, time related changes and bone growth of the patient can be addressed. Within an AM process, generally 2D Digital Imaging Communication and Medicine (DICOM) of defected part are generated by CT or MRI scan of the bone and then using CAD software, DICOM is converted into 3D Standard Tessellation Language (STL) format [186-188]. STL is a widely accepted 3D data format compatible with CAD software for manipulation and 3D printers for printing of models. Basic design procedure for bone implant is as follows: DICOM

data is exported from CT scan, bone data extracted and soft tissues data is filtered out, bone data manipulated to design of 3D implant virtually by adapting a mirror image of unaffected bone structure in unilateral defect to the affected bone structure across the symmetry plane and then editing by the digital sculpting to fil in the defect [186]. This digital implant STL file is then transferred to a 3D printer of choice for manufacturing the implant directly. The schematic diagram for the steps involved in 3D printing is given below in Figure 6.

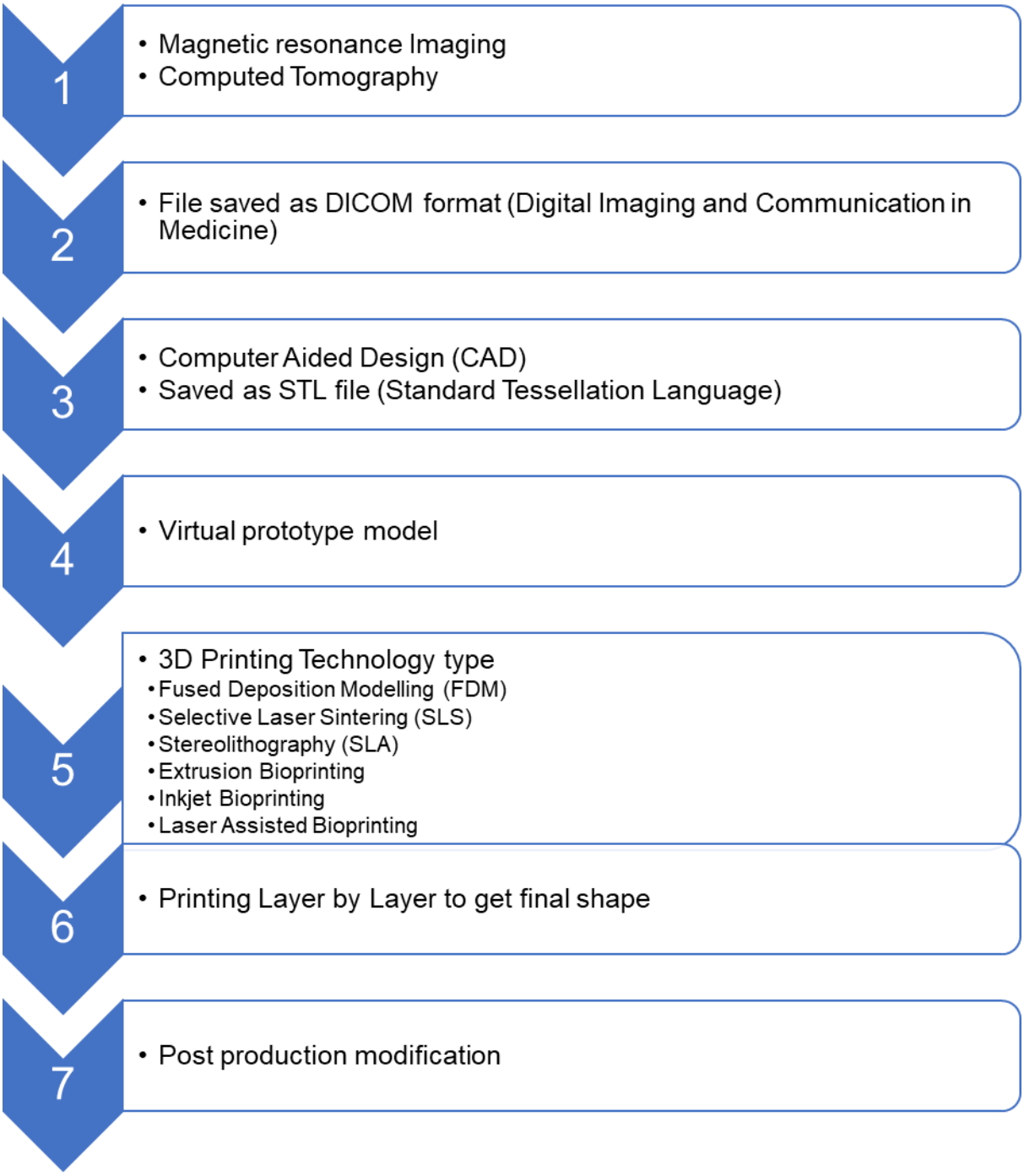

Figure 6 Schematic diagram of 3D printing procedure

2.1.10 Types of Additive Manufacturing

AM spans a variety of techniques including, but not limited to, fused filament fabrication (FFF), stereolithography (SLA), polyjet printing, powder bed fusion, laser sintering, electron beam melting (EBM), selective laser sintering (SLS), direct writing and inkjet deposition. Metallic craniofacial implants are often manufactured by additive manufacturing types, selective laser melting (SLM) and electron beam melting (EBM). The basic principle for both is same the only difference is the source of heating, laser in SLM and e^--beam in EBM. These technologies not only offer the adjustable modulus of elasticity of metallic implants but also provide the complex internal and external structure simply, rapidly and precisely [189]. Mostly metallic craniofacial implants in clinical practice are porous or in the form of mesh, they not only give the desirable elastic modulus and pores for cell proliferation but also provide low weight implant.

Yan et al. [190] reported an innovative clinical procedure in which workflow was done based on a complete digital design strategy combining the data from a CT scan and fabricating 3D Ti6Al4V scaffolds via EBM. Shi et al. [97] reported porous (65-88 % porosity) titanium alloy (Ti6Al4V) implant for biomedical applications with elastic modulus 12-18 GPa, close to human cortical bone. The implant was developed *via* SLM and the porous structure showed successful *in-vitro* proliferation of bone mesenchymal cells. Yan et al. [191] manufactured Ti6Al4V alloy bone implant by SLM with biomorphic designs, gyroid and diamond. They showed that modulus and porosity can be tailored by varying porosity to get optimum values. Yanez et al. [192] studied gyroid porous titanium structures developed by EBM, presented good and versatile strength and stiffness to be used for bone defects repair. Larosa et al. [193] manufactured and characterized Ti6Al4V custom-built implant by direct laser metal sintering (DMLS) technique for craniofacial reconstruction. El-Hajje et al. [194] prepared 3D printed titanium scaffolds with dual porosity: micropores (from burnt out of binder, PVA) and macropores (form CAD), for biomedical applications. The samples had 32-53 % porosity and Young's modulus (8 GPa) was comparable to the bone (8-13 GPa). Mishinov et al. [195] produced eight patient-specific craniofacial implant by Direct metal laser sintering (DMLS) for clinical practice, followed-up for 6-12 months and found no reaction or complication due to implant. Park et al. [196] presented case studies of 21 patients who received custom-made titanium craniofacial implants for calvarial defects produced by EBM, followed 6 to 24 months and found no complications, shorter the operating time, lower risk of operation and perfect anatomical alignment.

FFF is used for making polymeric implants with high strength at fast rate. It uses polymeric filament as a feedstock material which melts down after passing through a heated head and deposited layer after layer to form a final object. A schematic diagram of FFF process has shown in Figure 7. Wide range of thermoplastic materials can be used in this technology. It is inexpensive type of 3D printing with low running cost. The quality of the 3D parts depends on various printing parameters such as printing speed, layer thickness, raster angle, printing temperature, nozzle diameter etc. The schematic diagram of FFF process has been given below:

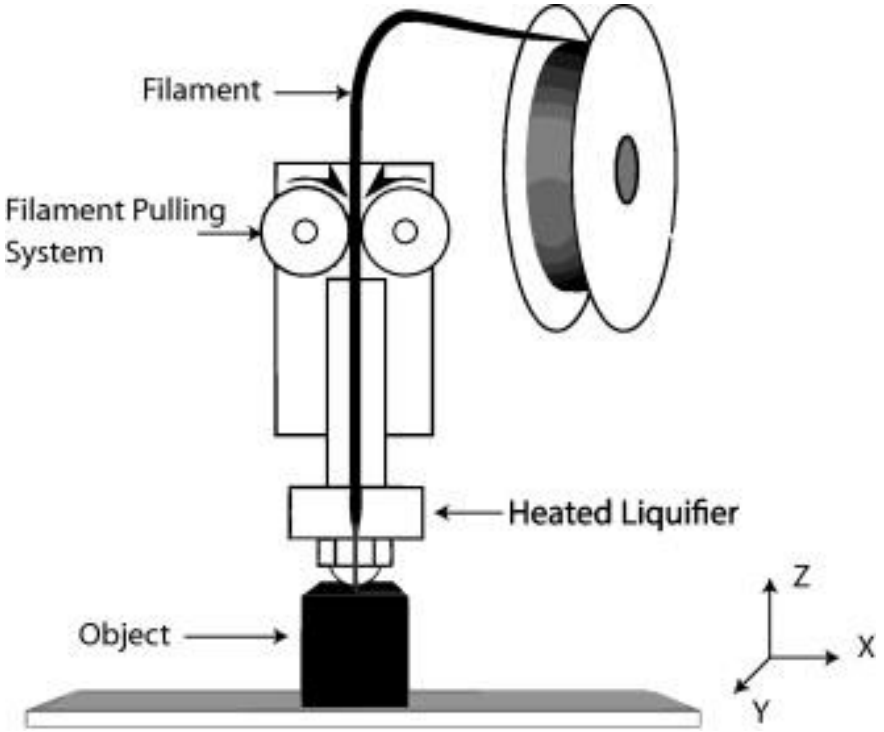

Figure 7 Schematic diagram of FFF 3D printing process [197]

Bioprinting is also a recent technology in which cells-laden scaffolds are prepared for the construction of anatomical structures (e.g., skin, organs, cartilage) [198]. Materials used in bioprinters need to meet specific requirements. One major drawback of bioprinting is the low viability of placed cells. It would also require resolving logistics, packaging, shipping, and quality control related issues. Although, much research is being conducted in this area, however, there is not yet regulatory approved clinical application for bioprinted constructs [199, 200]. Hence, due to the recent technology and initial phases, the TRL of bioprinting is quite low as compared to FFF technology (discussed in section 1.1). The summary of types of AM processes and their applications is given below in the Table 1.

Table 1 Summary of AM techniques with their applications

Technique	Principle & Materials	Applications, Pros and Cons	References
Extrusion Based			
Fused Filament Fabrication (FFF)	• A layer-by-layer molten thermoplastic polymer is deposited on a built platform to form an object • Polylactic acid (PLA), nylon, acrylonitrile butadiene styrene (ABS) and Wax	Orthopaedic implants, dental implants, screws, pins and plates, medical instruments, rapid prototyping and exoskeleton • Inexpensive process, widespread, wide range of materials can be used • Quality and accuracy dependent on nozzle radius, low speed, contact pressure to increase quality	[201, 202]
Bioprinting	• By means of pressure, biological material is extruded through nozzle and put down in consecutive layers to build scaffold • Alginate, collagen, chitosan, gelatine, fibrin	Biomedical applications such as heart valve, nerve, skin, musculoskeletal tissue	[31, 203, 204]

Powder bed sintering			
Selective Laser Sintering (SLS)	• Particles of powder are fused together to form an object by means of high-power laser • Nylon, polyamide, PEEK, PEKK, waxes, metal powders and ceramic powders	Orthopaedics, craniofacial and dental implants • Inexpensive, small technology: office size machine, large range of material options, good strength • Low speed, limited sizes, dependence on powder morphology, high cost, powdery surface	[205, 206]
Electron Beam Melting (EBM)	• EBM is similar to SLS instead high electron beam is employed to fuse powder particles • Titanium and its alloys, cobalt-chrome alloy		[206-208]
Photopolymerization			
Stereolithography (SLA)	• A UV light is used to selectively harden the photo-polymer resin in layers • UV curable resin and ceramic suspension	Prototypes, casting patterns, soft tooling, bone, dental models, dental implant guides, hearing aids • High resolution and accuracy, complex parts, smooth surface finish, large part size	[209, 210]
Digital Light Processing (DLP)	• It is similar to SLA, light is passed through a lens at the bottom and built platform raises upward		[211, 212]

	• Photopolymers	• Lacking in strength and durability, still affected by UV after print	
Material Binding			
Inkjet/Binder Jetting (BJ)	• A liquid binding agent selectively dropped to join powder particles • Gypsum or starch powder ABS, Polycarbonates, stainless steel	Blood vessel, skin, medical models, dental casts, dental implant guides, colour coded models for anatomy • High accuracy, low waste of materials, range of colours, different binder-powder combination for various mechanical properties • Limited materials, not suitable for structural parts, time consuming required post-processing	[213, 214]
Polyjet (PJ)	• Like Inkjet printing, photopolymer liquid is sprayed in layers on built platform and cured instantaneously by UV light instead of the binding agent. • Polycarbonate, polypropylene and polystyrene		[215, 216]

2.1.11 PEEK and its composites

Regardless of possessing biocompatible properties, PEEK is a bioinert material and offers negligible osseointegration in implants. Composites of PEEK are becoming popular to tailor and improve its mechanical and to enhance its bioactivity. Osseointegration can be improved by incorporating the porosity in PEEK based implants [217]. In PEEK composites LT1 medical grade is usually used. The composite of PEEK with 30 wt.% of randomly oriented short carbon fibers has similar elastic modulus as human cortical bone [218, 219]. A material is considered suitable for biomedical applications, if it has an elastic modulus that is close to the human cortical bone i.e. 18 GPa [220] to avoid stress shielding effect. Furthermore, tensile strength and compressive strength of human cortical bone is 50 to 151 MPa and 130 to 180 MPa, respectively [221-223]. PEEK is a suitable candidate to replace titanium and its alloys, Cr-Co-Mo alloys and bio-ceramics in bone tissue engineering due to close match of elastic modulus. Hence, tensile strength can be achieved by varying processing parameters [224].

In order to enhance activity towards living tissues, PEEK is sometimes blended with bioactive materials like hydroxyapatite, β-tri calcium phosphate (TCP) and bioactive glass. Many reports in literature show improvement in osseointegration and/or biomechanical properties of PEEK composites instead to pure PEEK [225]. On contrary with glass fibres and carbon fibres, HA and TCP show less affinity in mechanical properties and has negative effect on ultimate tensile strength (UTS). When HA is loaded 40 % in PEEK matrix, UTS decreased to 45 MPa by 45 % which is nearly equal to cortical bone. HA/PEEK composites show very less resistance to fracture [10]. In a study about PEEK/doped HA composites, PEEK composites with 40 wt.% nano-flourohydroxyapatite (nano-FHA) were prepared by compression moulding and then surface treated using TiO_2 blasting to study the effect of surface roughness. The authors reported excellent bioactivity, antibacterial properties, osseointegration and bone-implant contact which was attributed to the synergistic effect of surface roughness and nano-FHA particles [226]. Moreover, Wong et al. prepared PEEK/SrHA composites via compression moulding with varying amounts of SrHA ranging from 0 to 30 vol.%. They reported that as the vol.% of SrHA increased, the bending strength of the composite decreased while the bending modulus increased. A PEEK sample with 25 vol.% of SrHA showed enhanced apatite formation ability in SBF and enhanced MG-63 cell attachment ability as compared to 25 vol.% of pure HA with PEEK [227]. In another

study, electrostatically bonded PEEK composites were fabricated by the incorporation of 5 and 10 vol.% of SrHA via cold pressing and then characterized; it was reported that the compression strength and hardness of disc shaped samples increased while the modulus decreased. The samples showed apatite layer formation on the surface after incubation for 14 days in SBF [228].

Kim et al. [229] reported the composite of calcium silicate with PEEK. The authors incorporated spherical particles of calcium silicate (30%CaO–70%SiO) into PEEK LT1 grade. The concentration of particles varied from 0 to 50 % in PEEK and studied the mechanical properties of composite. They reported that the Young's Modulus initially increased with the increased percentage of filler particles. It was maximum at 20 % and then decreased sharply, similar behaviour was observed with bending strength of composite. They observed the agglomeration of filler particles in the fractured surfaces of composite samples.

PEEK composites with nanomaterials were also reported by many researchers. However, they processed PEEK composites by conventional technologies. Biomechanical properties of PEEK with strontium substituted hydroxyapatite (SrHA/PEEK) was enhanced as compared to classical PEEK Optima by using 15-30 % SrHA [227]. Nano-silica ($nSiO_2$) and nano-alumina (nAl_2O_3) were incorporated in PEEK by 20-50 %. Improved elastic modulus and tensile strength but decreased elongation of these composites as compared to PEEK, were reported [230]. Wu et al. [231] prepared composite of PEEK with nano-Titania ($nTiO_2$) by compression moulding technique. They observed the better biological properties of the composite i.e., enhanced cell attachment and increased osteoblast cell spreading. They reported bone regeneration around titania in the in-vivo studies.

Mechanical properties of samples prepared by FFF mainly depend on the infill density and raster angle while other minor factors are printing speed, layer height and nozzle diameter [232]. Kazi et al. [233] reported mechanical properties of PEEK samples at three different orientations i.e. 0°, 90° and mixed 0/90°. They reported tensile strength 73 MPa for 0°, 54 MPa for 90° and 66 MPa with mixed orientation. Compression strength for 0° and 90° were 81 MPa and 73 MPa, respectively. Flexural strength obtained for 0°, 90° and mixed 0/90° were 111 MPa, 80 MPa and 95 MPa respectively. Average impact energy absorbed by the specimen for 0°, 90°, and mixed 0/90° was 17 Nm, 1.4 Nm and 0.7 Nm, respectively.

Berretta et al. [234] manufactured the porous PEEK cranial implants produced by High Temperature Laser Sintering (HT-LS) and investigated the dimensional accuracy, weight and mechanical properties. Roskies [235] et al. prepared porous scaffolds of PEEK for craniofacial reconstruction via SLS and reported their viability for mesenchymal stem cells. They reported that the porosity in PEEK cells is beneficial for cell proliferation and growth. Wu et al. [236] investigated the effects of layer thickness (200, 300, 400 micron) and raster angle (0°, 30°, 45°) on mechanical properties of PEEK and ABS samples via FFF. Tensile strength and flexural strength of pure PEEK samples by using injection moulding are reported as 100 MPa and 163 MPa respectively. These values were decreased considerably when processed by FFF technique, the tensile strength and flexural strength reported as 56.6 MPa and 56.2 MPa, respectively. PEEK and HA composites developed by additive manufacturing are summarized in the Table 2.

Table 2 PEEK/HA composites manufactured by AM for biomedical applications.

Material	**Manufacturing technique**	**Composition (wt%)**	**Key Findings**	**References**
PEEK/HA	FFF	0 to 30 %	High mechanical properties (UTS upto 94.2 MPa) by using high ambient temperature	[237]
PEEK/HA	FFF	Up to 30 %	Effect of printing path on mechanical properties, best mechanical and bioactive properties were obtained with horizontal-90° and vertical-90°	[238]
PEEK/HA	FFF	Up to 30 %	Surface characterization of 3D parts, adhesion and growth of osteoblast like cell	
PEEK/HA composite scaffolds	SLS	10, 20, 30, 40 % HA in PEEK	Successfully prepared 3D scaffolds via SLS	[239]
PEEK/HA scaffold	SLS	10, 20, 30, 60 % HA in PEEK	SBF studies showed apatite layer formation in 28 days and human fibroblast cells studies showed cell adhesion and cell growth	[240]

PEEK/HA porous scaffold	AM + compression molding	Bioceramic paste, porous ceramic scaffold by AM, incorporation of PEEK (Optima) melt	Improved mechanical strength with incorporation PEEK melt in the pores of bioceramic scaffold	[241]
PEEK/HA porous scaffolds	Extrusion-compression molding and free forming	Up to 20 %	Good mechanical properties and cell studies due to the presence of HA	[11]

2.1.12 Bioactivity of PEEK and its composites

PEEK inherits bioinert nature due the presence of an aromatic backbone [242]. Many attempts have been made to alter its bioinert nature and make it bioactive such as surface modification or treatment and making its composites [243]. The surface can be modified either by a physical treatment such as plasma modification or wet-chemical treatment such as sulfonation. In plasma treatment, reactive particles are generated in closed low pressure system by excitation with electromagnetic waves, interact with the PEEK surface in a reactor and modify its physical and chemical properties without altering its most relevant properties such as mechanical, optical and electrical properties [244, 245]. The plasma can be generated by using a gas or a mixture of gases such as oxygen plasma, ammonia plasma, oxygen-nitrogen plasma, methane-oxygen plasma, oxygen-argon plasma, hydrogen-argon plasma, ammonia-argon plasma, hydrogen-argon plasma and accelerated neutral atom beam [243]. Chemically modified PEEK is obtained by wet surface chemistry and produce series of functionalized PEEKs such as sulfonation treated PEEK (SPEEK), hydroxylated PEEK (PEEK-OH), carboxylated PEEK (PEEK-NCO), aminated PEEK (PEEK-NH2), and aminocarboxylated PEEK (PEEK-GABA and PEEK-Lysine) [9]. Additionally, the bioactivity of the PEEK can be enhanced by coating with some appropriate bioactive material. The most common bioactive coating material is HA which is coated by various means such as cold spraying [228], spin coating [246], aerosol deposition [247] and radiofrequency magnetron sputtering [248]. Other than HA, Ti is also coated on PEEK and its composites to enhance its bioactivity by ionic plasma vapor deposition [249], plasma vapor deposition [250], electron beam deposition [251] and vacuum plasma spraying (VPS) [252]. Moreover, coating of titanium dioxide (TiO_2) has also been reported to enhance the bioactivity of PEEK and its composites. The other method to increase the bioactivity of bioinert PEEK is by making its composites with bioactive ceramic powders such as HA, calcium phosphates, bioglass, calcium silicate and glass-ceramics. The powders were mixed physically/mechanically and processed by various technologies such as SLS, FFF, injection molding and extrusion.

There are various methods reported to assess the bioactivity of PEEK and its composites such as in-vitro and in-vivo. In-vitro testing is taken place in the laboratory vessel or other controlled experimental environment while in-vivo testing is taken place within the living organism or natural setting [253]. The most common in-vitro testing is either by SBF immersion

or cell attachments. In SBF immersion, samples are immersed in SBF solution for up to 28 days. The formation of apatite layer on the surface of samples is observed via SEM which confirms the bioactivity of the samples. Other way, activities of osteoblast cells such as cytotoxicity, attachment and proliferation are observed when samples are in-contacted with them. However, in-vivo testing, the samples are implanted in living organisms such as rabbits, mice or humans for certain period of time and observed their interaction [10, 254, 255]. Hence, it has been reported widely that the in-vitro and in-vivo bioactivities of PEEK increased tremendously in the presence of HA or doped HA. The bioactivity of PEEK and its composites reported by various researchers have been summarized in the Table 3 below.

Table 3 Types of AM technologies with biomedical applications

Material	**Technology**	**Sample Shape**	**Biological Study**	**Duration of In-vitro studies (Days)**	**Reference**
PEEK/HA	FFF	Disks	Osteoblast like cells	7	[256]
PEEK	FFF	Disks	Cell culture using human osteosarcoma cell line SAOS-2 osteoblast	1, 3, 5	[257]
nHA/PEEK (HA 40 wt.%)	Injection moulding	Disks (15 mm diameter and 2 mm thick)	Human osteoblast-like MG-63 cells for attachment and proliferation	3, 7, 14	[258]
			Alkaline Phosphatase Activity	7, 14, 21	
MgP/PEEK filaments (15 vol.%)	Extrusion	2 mm diameter	Mouse pre-osteoblasts (MC3T3-E1) for attachment and proliferation	4, 7, 14	[259]
			Simulated body fluid	7	
			In vivo study in rats	12 weeks	

Material	Technology	Sample Shape	Biological Study	Duration of In-vitro studies (Days)	Reference
nHA/PEEK (nHA 15 vol.%)	Injection moulding	Disks	Cell attachment using Saos-2 cell lines	1, 3	[260]
			Analyse cell viability using MTT and WST-1 assays	3, 7, 10	
			Alkaline Phosphatase Activity	3, 7, 14	
			Biomineralization test by Simulated Body Fluid	21	
HA/PEEK	Spraying HA on PEEK	Disks (12 mm x 3 mm)	Cell attachment with human bone marrow mesenchymal stem cells	1, 3, 5	[228]
			Alkaline Phosphatase Activity	7, 21	
			Implantation in rabbits	4, 8 weeks	
	SLS	Disks	Simulated Body Fluid	28	[240]

HA/PEEK (HA 40 wt.%)			Cell attachment with Human fibroblast cells	1	
HA/PEEK (HA 30 wt.%)	Injection moulding	Disks (15 mm diameter and 2 mm thickness)	Apatite layer formation by Simulated Body Fluid	7, 14, 21, 28	[10]
			MC3T3-E1 cells were used for cell attachment and proliferation	1, 3, 7	
			Alkaline Phosphatase Activity	7, 14	
			In vivo studies in rabbits	8 weeks	
nHA/PEEK	Compression moulding	NA	Apatite layer formation by Simulated Body Fluid	7, 14, 28	[261]
			Cytotoxicity with RAW-264.4 and L-929celllines	NA	
SrHA/PEEK (25% SrHA by vol.)	Compression moulding	Cylindrical shape (D: 12 mm x H: 2 mm)	Simulated Body Fluid	1, 14	[262]
			Human osteoblast-like cell line MG-63	3, 7, 14	

Material	Technology	Sample Shape	Biological Study	Duration of In-vitro studies (Days)	Reference
HA/PEEK (20 vol.% HA)	Injection moulding	Cylindrical (10 mm x 8 mm)	Implantation in pigs	28 weeks	[263]
HA coated PEEK	Aerosol deposition	Disks	Cell attachment with MC3T3-E1 pre-osteoblast cells	1, 3, 5	[264]
			Alkaline Phosphatase Activity	10	
			Implantation in rabbits	4 weeks	
HA/PEEK	Hot pressing	Cylindrical	Implantation in rabbits	16 weeks	[265]
sPEEK	Sulphonation of PEEK	Disks	Simulated body fluid	10	[266]
			Cell attachment with MC3T3-E1 pre-osteoblasts	7	
			Implantation in rats	12 weeks	

2.2 Standards for material testing

Generally, the materials are handled, prepared and tested according to the standard protocols developed by either International Organization for Standardization (ISO) or American Society of Testing Materials (ASTM). The materials used in this study were handled and characterized according to various ISO standards. For example, PEEK was handled and processed as mentioned in ISO 23153. HA and doped-HA were characterized by using ISO 13779-3. *In-vitro* testing of samples was performed in SBF solution according to ISO 13779.

In this study, bioactive composites of PEEK with SrHA and ZnHA were processed via FFF 3D printing technology. Previously, these composites were processed via conventional technologies such as extrusion, injection molding, compression molding. The 3D printing process was optimized, and the samples were characterized by various scientific techniques in the following chapters.

3 Chapter 3: Materials and methods

3.1 Introduction

The properties of final product sometimes depend upon the route adopted for their manufacturing. Additionally, the quality of the final parts also depends upon the quality of the starting raw materials. Hence, it is important to understand the methods and techniques used to characterize the samples. In this chapter, the detailed information about the grade and quality of materials used and the methods adopted to produce samples for various characterizations have been described. PEEK powder used in this study was a commercial powder, however, bioceramic particles such as hydroxyapatite and doped hydroxyapatites were synthesized in the lab by a reported method. The main purpose of synthesizing doped-HA in the lab was that it was not available commercially. Furthermore, the chapter detailed about the manufacturing approaches and processing techniques used for making filaments and 3D printed samples, and the techniques adopted to characterize the samples such as physical, chemical, mechanical and *in-vitro* testing.

In this study, methods and equipment adopted by considering various factors. For example, wet-chemical precipitation method was adopted to synthesize the bioceramic particles because of the simplicity of the procedure and hence, reported widely. Additionally, desktop extruder was selected for filament extrusion instead of commercial extruder, which was large and hence, more wastage of material was expected during optimization. Moreover, FDM 3D printer was adopted to optimize and produce samples instead of SLS. As compared to SLS, FDM 3D printers are less costly and there is low material wastage during 3D printing.

3.2 Manufacturing approaches

3.2.1 Wet chemical precipitation method for the synthesis of HA and doped-HA

Hydroxyapatite and doped hydroxyapatite were synthesized by wet chemical precipitation method. All chemicals used were of analytical grade. Calcium hydroxide [$Ca(OH)_2$, ACS reagent ≥95 %] orthophosphoric acid (H_3PO_4, with 85 % purity), Ammonium Hydroxide (NH_4OH, 28-30 % w/w), Calcium Nitrate [$Ca(NO_3)_2.4H_2O$], Strontium Nitrate [$Sr(NO_3)_2$] and Zinc Nitrate Hexahydrate [$Zn(NO_3)_2.6H_2O$] were purchased from Sigma Aldrich. Deionized water (DI) was supplied by Fisher Scientific chemicals.

HA and doped HA were synthesized via the wet precipitation method, as reported elsewhere [267]. For synthesis of pure hydroxyapatite (HA), $Ca(OH)_2$ suspension was initially stirred in DI water at 400 RPM for 1 h at 60 °C. An aqueous solution of H_3PO_4 was added dropwise to calcium hydroxide solution at the rate of 4-5 ml/min. pH of the mixture was monitored after every 2-3 minutes and adjusted to ≥ 9 with NH_4OH solution. The mixture was further stirred for 2 h for complete mixing and left to age for 24 h. Then the settled precipitates were washed 3-5 times with DI water until neutral pH. Precipitates were ground to a fine powder with pestle and mortar after being dried at 80 °C in a drying oven for 24 h [267]. The chemical equation of the reaction has been given below:

$$10Ca(OH)_2 + 6H_3PO_4 \longrightarrow Ca_{10}(PO_4)_6(OH)_2 + 18H_2O\ldots\ (1)$$

In order to synthesize Sr (Sr, 5 % by wt.) and Zn (Zn, 5 % by wt.) doped HA, their respective salts $Sr(NO_3)_2$ and $Zn(NO_3)_2.6H_2O$, were mixed in an aqueous solution of calcium nitrate and allowed to mix separately for 1 h at 400 RPM by using hotplate/magnetic stirrer. Subsequently, aqueous solution of H_3PO_4 was added dropwise at the rate of 4-5 ml/min. After every 2-3 minutes, the pH of the mixture was monitored and adjusted to ≥ 9 with ammonia solution. To ensure homogenous mixing, the mixture was further stirred for 2 h and then left to age for 24 h. The precipitates were settled down and the liquid was decanted off. The collected precipitates were washed with DI water 3-5 times until neutral pH. The precipitates were dried in an oven at 80 °C for 24 h and then finally grinded with pestle and mortar. The chemical equations of the reactions have been given below:

$$(10\text{-}x)Ca(NO_3)_2.4H_2O + xSr(NO_3)_2 + 6H_3PO_4 \longrightarrow Ca_{(10-x)}Sr_x(PO_4)_6(OH)_2 + H_2O\ldots(2)$$

$$(10\text{-}x)Ca(NO_3)_2.4H_2O + xZn(NO_3)_2.6H_2O + 6H_3PO_4 \longrightarrow Ca_{(10-x)}Zn_x(PO_4)_6(OH)_2 + H_2O..(3)$$

The obtained powders were sintered in a furnace (Nabertherm, Model B400) under air atmosphere by heating from room temperature to 900 °C at the heating ramp 10 °C/min. and isotherm for 4 h at 900 °C. After isothermal conditions, the samples were cooled in the furnace. Furthermore, the sintered powders were grinded and sieved through 180 µm mesh size sieve. The samples were labeled as HA, SrHA and ZnHA. It is important to note here that 5 w/w % doped HA has been used throughout this study.

3.2.2 Extrusion of PEEK and its composite filaments

Filaments were prepared by mixing PEEK powder with HA, SrHA and ZnHA at different weight percentages. PEEK powder (VESTAKEEP®, grade 2000UFP, GmbH Germany) was supplied by Evonik. PEEK powder was mixed manually at following percentages: 10 wt.% HA, 10 wt.% SrHA, 20 wt.% SrHA, 30 wt.% SrHA, 10 wt.% ZnHA, 20 wt.% ZnHA, 30 wt.% ZnHA. The mixed powders were dried in the drying oven at 110°C by spreading on aluminum foil to remove any moisture present. The commercially available desktop extruder (3devo Composer 450) was used to prepare filaments of diameter 1.75 ± 0.05 mm. The obtained filaments were labeled as PEEK/10HA, PEEK/10SrHA, PEEK/20SrHA, PEEK/30SrHA, PEEK/10ZnHA, PEEK/20ZnHA, PEEK/30ZnHA.

3.2.3 Sample preparation by FDM 3D printing

The samples for tensile testing, impact testing and bioactivity testing were prepared by using commercial FFF 3D printer SpiderBot 4.0 HT. The samples for tensile testing were prepared according to ISO 527-2 Type 5A which had following dimensions: length ≥ 75 mm, width at gauge length = 4.0 ± 0.2 mm, thickness = 2.0 ± 0.1 mm. The unnotched samples for impact testing were prepared according to ISO 180:2000 with dimensions: length = 80 ± 2 mm, width = 10.0 ± 0.2 mm, thickness = 4.0 ± 0.2 mm. Additionally, disc shaped samples were prepared with diameter 10.0 ± 2 mm for bioactivity testing.

3.2.4 Optimization of 3D printing

The samples for tensile testing, impact testing and bioactivity testing were prepared via commercial FFF 3D printer SpiderBot HT 4.0 as shown in Figure 8. The printer was of cylindrical shape with closed chamber equipped with internal IR heaters and print-bed heating facility. The inside chamber temperature of the printer could be controlled by adjusting temperature of IR heaters which could heat up to 450 °C while the maximum limit to raise chamber temperature was 80 °C due to the electronic parts present at the top of the printer. Also, the temperature of print-bed which was made of aluminum could be heated up to 210 °C.

Figure 8 SpiderBot HT commercial FFF 3D printer for printing PEEK and its composite samples

Computer Aided Design (CAD) files were saved in STL format and then sliced in a free software named as CURA. That CURA software transformed the CAD files into the GCodes which contained all the information to control movement of printhead in XYZ direction, printing speed, layer thickness and printing temperatures. In 3D printing process, the polymeric material in the form of filament was passed through the heated printhead which is usually heated at the temperature greater than its melting point and after passing through the heated head the molten polymer comes out from a nozzle made of brass or stainless steel. The molten material deposited layer by layer and after each layer the printhead moved in Z-direction with a distance equal to the layer thickness. The molten layers fused together to form a final shape 3D object [268]. Hence, the samples were prepared after the optimization of various parameters such as layer thickness, printing speed, printhead temperature, bed temperature and chamber temperature. Each printing

parameter had effect on the print quality and mechanical properties. The adhesion of the first layer to the print-bed is very crucial because if it fails the print fails. In this study, the first layer was not adhering to the print-bed so various steps were applied for the successful adhering such as levelling of print-bed, cleaning with isopropanol, increasing the print-bed temperature, increasing the printhead temperature, adjusting the printing speed of first layer and applying a thin layer of adhesive material which can withstand at high temperature. The samples failed during the optimization of 3D printing process has shown in Figure 9 below.

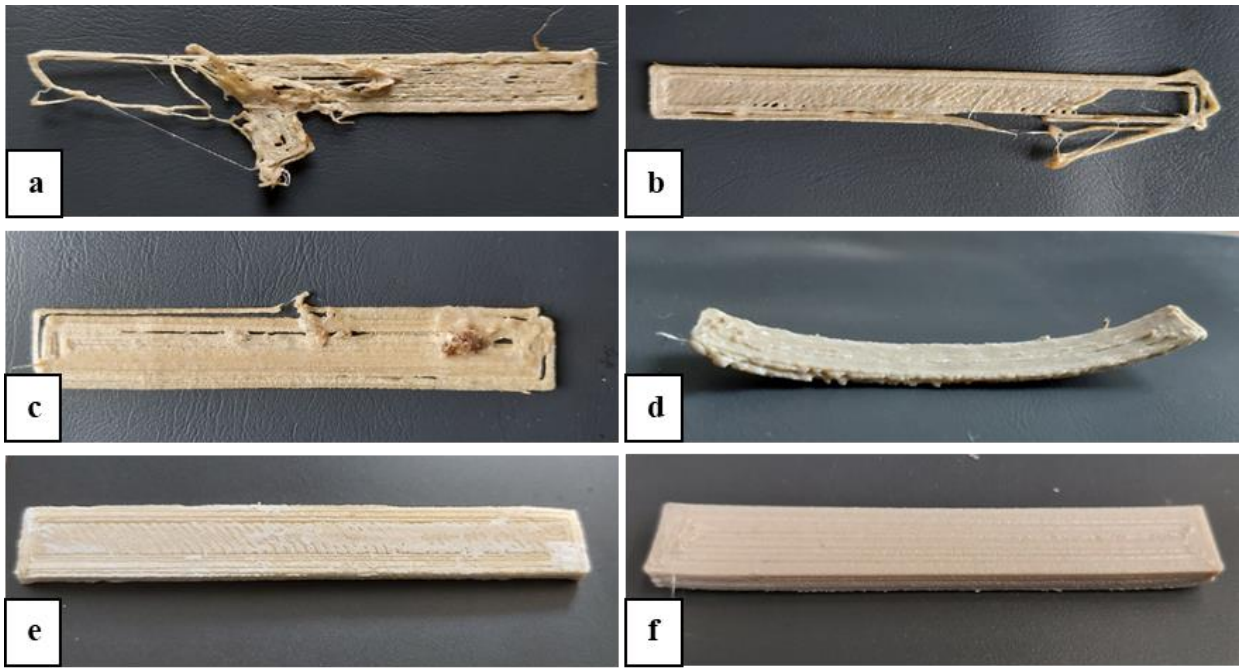

Figure 9 FFF 3D printing optimisation of PEEK nanocomposites at a) low nozzle temperature, b) low printing speed c) high printing speed, (d) low bed and chamber temperatures, e) & f) successful prints of impact testing samples

The most effective methods found were the combination of lowering the printing speed of first layer and by applying a thin layer of paper-glue. Initially, lower printhead, print-bed and chamber temperatures were used. However, the print failed during the 3D printing by detaching from the print-bed. It was observed that the detaching was happened due to the shrinkage of the polymer. Hence, the problem was overcome by raising printhead, print-bed and chamber temperatures gradually. For example, pure PEEK was initially tried to print at 360 °C, 120 °C and 60 °C with printhead, print-bed and chamber temperatures, respectively. However, the print fails every time so by gradually increasing those temperatures, optimum values were obtained at which

good quality samples were obtained. This method was applied with PEEK composite samples and obtained optimised parameters for each composite. The obtained tensile testing samples has shown in Figure 10. The summary of optimized parameters for each material have been reported in Table 4 below.

Table 4 Optimised parameters for 3D printing PEEK and its nanocomposites

	PEEK	**PEEK/10SrHA and PEEK/10ZnHA**	**PEEK/20SrHA and PEEK/20ZnHA**	**PEEK/30SrHA and PEEK/30ZnHA**
Nozzle temperature (°C)	390	410	420	430
Bed temperature (°C)	150	160	180	200
Chamber temperature (°C)	75	80	80	80
Layer thickness (mm)	0.2	0.2	0.2	0.2
Printing speed (mm/s)	30	30	30	30
Infill density (%)	100	100	100	100
Infill pattern	-45, +45	-45, +45	-45, +45	-45, +45
Nozzle diameter (mm)	0.5	0.5	0.5	0.5

Figure 10 Tensile testing samples of PEEK nanocomposites prepared at optimised conditions via SpiderBot FFF 3D printer

3.3 Characterizations

3.3.1 Physical

Particle size and morphology of the raw materials in the powder form were observed through SEM (FESEM HITACHI, Japan) at 10 kV under high vacuum with working distance ~5.5 mm. All samples were gold sputter coated before analysis. Prior to 3D printing, the distribution of the bioceramic particles in the filaments was investigated using micro-computed tomography (µ-CT; Microtomograph SkyScan 1275 Bruker USA) with source voltage 40 kV, source current 250 µA and pixel size 10 µm. The top view of the surface morphology and the distribution of bioceramic particles in the 3D printed samples were observed through field emission scanning electron microscopy (FESEM; HITACHI Japan). The samples were gold sputter coated prior to analysis and observed under high vacuum at 10 kV. Static water contact angle was measured to assess the samples hydrophilicity using a Surftens Basic contact angle instrument from OEG GmbH. The samples were placed on the observation stage and a droplet of deionised water (typically between 0.5-1.0 µL) was manually released onto the surface, using a Luer-lock glass syringe. The contact angle value was calculated from the obtained images using both sides of the droplet with Surftens Automatic 4.7 software, 5 droplets were measured for each sample type and the results are expressed as the average value ± standard deviation. The thermal properties (glass transition, melting and recrystallization temperatures) of the materials were analysed using Differential Scanning Calorimetry (DSC; Perkin Elmer). The tests were carried out in accordance with ISO 11357 at a heating rate of 10 °C/minute under flowing nitrogen. The samples were heated from 25 °C to 400 °C with a heat-cool-heat cycle. The crystallization temperatures were measured in the first cooling cycle whereas the melting temperatures were recorded during the second heating cycle to remove the influence of thermal history. The degree of crystallinity was calculated using the formula in equation (iv):

$$Xcw\ (\%) = \frac{\mathrm{Hm}}{\mathrm{Wf} * \mathrm{Hc}} * 100 \ldots\ldots\ldots\ldots\ldots\ldots\ldots\ldots (4)$$

where Hm is the melting enthalpy acquired from the DSC scan, Wf is the weight fraction of PEEK polymer in nanocomposites and Hc is the melting enthalpy of fully crystallized PEEK (130 J/g) [259].

The samples were dip-coated with PEG_{1000}-DOPA. Prior to the coating fabrication, the samples were wiped with acetone to remove any surface contamination. PEG_{1000}-DOPA was dissolved in Tris HCl aqueous buffer (pH 8.5) at a concentration of 2 mg/ml. The samples were then immediately immersed in this solution for 18 h at room temperature, using a laboratory dip-coater by Ossila UK. The samples were clamped and immersed vertically in the PEG_{1000}-DOPA solution using the dip-coater arm. After completing the coating process, the samples were removed from the solution, rinsed with distilled water to remove any unbound PEG_{1000}-DOPA molecules and dried under nitrogen flow for 2-3 minutes.

3.3.2 Chemical

The crystalline phases of the 3D printed composite samples were identified by X-ray diffraction (XRD; PANanalytical X'Pert Pro) in 2θ range 10° to 80° with Cu Kα radiation (λ=1.54 Å). The elemental composition, purity of the raw materials and distribution of doping elements in HA were analyzed using an EDX machine (Oxford Instruments Ltd.) with Aztec software at 20 kV. Samples were analyzed for functional groups using FTIR (Thermoscientific iD5) in Attenuated Total Reflection (ATR) mode with resolution 8 cm^{-1} and range from 4000 cm^{-1} to 550 cm^{-1}.

3.3.3 Mechanical

The tensile and impact properties of the 3D printed samples were determined according to ISO 527-2 type 5A (dogbone shaped samples, overall length ≥ 75 mm, gauge length = 20.0 ± 0.5 mm, thickness = 2.0 ± 0.2 mm) and ISO 180:2000 (rectangular samples, length = 80 ± 2 mm, width = 10.0 ± 0.2 mm, thickness = 4.0 ± 0.2 mm), respectively. Tensile testing was performed on an INSTRON (Model 5500R) at a cross head speed 5 mm/min using a 5 kN load cell. Impact testing was carried out on unnotched samples using an Izod impact testing machine with a 0.5 kg hammer weight and falling speed of 20 mm/s. 3D model for impact testing sample has shown in Figure 11.

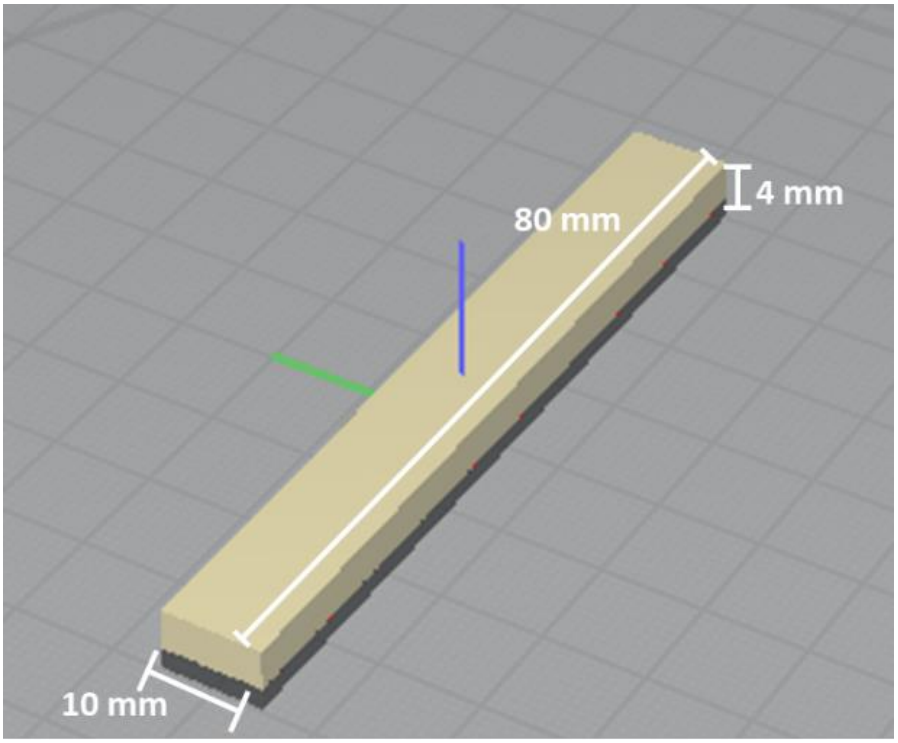

Figure 11 3D model of impact testing sample for 3D printing, labelled with dimensions

The bioactivity and the effect of apatite layer on the mechanical performance of the 3D printed samples were evaluated via a simulated body fluid (SBF) immersion test and prepared according to Kokubo's protocol [269]. The disk samples for bioactivity and dog-bone samples for mechanical evaluation were immersed in the SBF for 0, 7, 14 and 28 days. The apatite layer formation on the surface of samples was characterized via SEM, FTIR and XRD.

3.3.4 In-vitro testing

The ability of 3D printed samples to form a layer of apatite on its surface in SBF solution was assessed according to ISO 23317 [270]. SBF was prepared according to Kokubo's protocol [269]. The SBF prepared by this method has similar concentration of ions as of human blood plasma (Na^+ 142.0 mM, K^+ 5.0 mM, Mg^{2+} 1.5mM, Ca^{2+} 2.5mM, Cl^- 147.8mM, $HCO3^-$ 4.2mM, $HPO4^{2-}$ 1.0mM, $SO4^{2-}$ 0.5mM, pH 7.40 at 36.5 °C). The following reagents were used:

1. Sodium chloride (8.035 g), (NaCl, 99.5 %, for analysis, ACROS Organics™)
2. Sodium bicarbonate (0.355 g), ($NaHCO_3$, 99.5 %, for analysis, ACROS Organics™)
3. Potassium chloride (0.225 g), (KCl, trace metal basis 99.999 %, ACROS Organics™)

4. Potassium phosphate dibasic trihydrate (0.231 g), ($K_2HPO_4.3H_2O$, 99+ %, for analysis, ACROS Organics™)
5. Magnesium chloride hexahydrate (0.311 g), ($MgCl_2.6H_2O$, 99 %, for analysis, ACROS Organics™)
6. Calcium Chloride (0.292 g), ($CaCl_2$ Extra Pure, SLR, Fused, Granular, Fisher Chemical)
7. Sodium Sulfate Anhydrous (0.072), (Na_2SO_4, 99+ %, Extra Pure, Fisher Chemical
8. Tris-hydroxymethyl aminomethane Base (6.118 g) ($(HOCH_2)_3CNH_2$) white crystalline powder/Molecular Biology, Fisher BioReagents)
9. Hydrochloric Acid Solution 1 M (1 N) (0-5 ml), NIST Standard Solution for volumetric analysis, Fisher Chemical

Briefly, the reagents from 1 to 7 were dissolved completely one after the other in 700 ml distilled water whose temperature was maintained at 36.5 ± 1.5 ℃ with continuous stirring in a beaker placed over hotplate and magnetic stirrer. After that the distilled water was added up to the mark 900 ml and waited for temperature to maintain again at 36.5 ± 1.5 ℃. The pH electrode was inserted into the solution and pH was measured as 2.0 ± 1.0. The reagent 8^{th} (Tris) was added little by little and noted the change in pH. When the pH 7.30 ± 0.05 was achieved, then temperature of the solution was maintained at 36.5 ± 0.5 ℃. After that Tris and 1 M HCl was added simultaneously so that the pH of the solution was always in between 7.42 ± 0.01 and 7.45 ± 0.01. After dissolving all the amount of Tris, the pH of the solution was maintained at 7.40 at 36.5 ℃. When the pH was constant, the solution was cooled up to 20 ℃ and transferred in to 1000 ml volumetric flask. The more distilled water was added up to the mark 1000 ml. The solution was stored in plastic bottle at 5-10 ℃.

4 Chapter 4: Morphological, Thermal and Chemical Characterization of Raw Powders

4.1 Introduction

The investigation of the quality of raw materials was important because it was assumed that the mechanical and biological properties of final parts will greatly depend upon the structural and chemical nature of the precursors used. As described in the previous chapter, the PEEK powder which was used in this study was a commercial powder while HA, SrHA and ZnHA powders were synthesized in the lab by wet-chemical precipitation method. So, it was important to characterize as received PEEK powder and synthesized powders. Hence, raw powders such as PEEK, hydroxyapatite and doped hydroxyapatites were characterized by wide range of thermal, chemical and physical characterization techniques including SEM, EDX, TGA, DSC, FTIR, and XRD. The main purpose of characterizing the raw powders was to fully analyze the successful preparation of hydroxyapatite and doped-hydroxyapatite by the wet chemical precipitation method. The other purpose was to check for the phase purity and detect any impurity present before further using them in filament preparation and subsequently 3D printing which have been discussed in later chapters.

This chapter has provided a comprehensive characterization study of commercial PEEK powder, pure HA, SrHA (5 % w/w) and ZnHA (5 % w/w). SEM was used to analyze the morphological aspects of all the powders, EDX has provided the valuable information about the elemental composition, FTIR was used to confirm the presence of functional groups in the raw materials and XRD provided information about the phase purity. Thermal properties were determined by TGA and DSC where TGA measured the thermal degradation temperature of PEEK powder which was valuable to adjust the final range of working temperature. The glass transition temperature, crystallization temperature and melting temperatures were measured by DSC and helped in adjusting thermal parameters in filament preparation and 3D printing. In order to investigate the effect of extrusion and 3D printing on chemical and thermal properties, this raw material characterization data has been used as a control data and compared with the data which was obtained after extrusion and 3D printing. In this chapter, commercial PEEK powder, pure HA, Sr doped HA and Zn doped HA will be denoted as PEEK, HA, SrHA and ZnHA, respectively.

4.1.1 Morphological analysis

Particle size and morphology of PEEK, HA, SrHA and ZnHA powders were analyzed by SEM and shown in Figure 12 (A to H). In this study, the morphology of PEEK powder was not considered important due to its complete melting during extrusion process. Only particle size was taken into the account which played an important role in mixing with bioceramic particles, and it could physically mix with bioceramic powders homogenously before the extrusion process. It was assumed that the non-homogenous mixing of the powders would affect the overall performance of the final parts such as mechanical and biological properties. Generally, in the extrusion process of polymeric composites, the mixing of powders was taken place into two stages, firstly by physical mixing before the extrusion process while the second mixing had taken place during extrusion process in molten state [271]. There are various factors which affect the extent of first mixing such as mixing method and mixing time while the extent of second mixing mainly depends upon the distance travelled by the composites in molten state in the extruder which is normally equal to the length of the extruder. In this study, the length of the desktop extruder screw was not very large so there was a slight mixing during the extrusion process as compared to the commercial extruder machine which has a long extruder screw. Therefore, the powders were thoroughly mixed before using for extrusion. Additionally, it was assumed that the PEEK grade with larger particle size would not provide uniform mixing before extrusion process so fine PEEK powder grade was selected for this study to obtain homogenous mixing of powders before extrusion. As observed in Figure 12 A and B (A-low magnification image and B-high magnification image), the PEEK powder particles had an average particle size of ~10 µm. Furthermore, the particle sizes of HA, SrHA and ZnHA powders have shown in Figure 12 C to H. The shape of HA particles was spherical, and the average diameter of the particles were measured as ~40 nm. Additionally, the shape of SrHA and ZnHA particles were also spherical, and the particles had average diameter of ~80 nm and ~60 nm, respectively. As mentioned in previous chapter that the all the powders which were prepared by wet chemical precipitation method were sintered at 900 °C to obtain their crystalline structure. Hence, due to the sintering, the spherical particles of the powders were partly fused together and formed oval shaped elongated particles. Therefore, these particles joined together to form larger agglomerates [272, 273]. The sizes of the agglomerates were quite large and in the range of 100 micron to 500 micron. Those large agglomerates could block the nozzle during 3D printing. Hence, they were grinded and passed through a 180 µm sieve. Most of the

powder passed through the sieve while the powder which remained were grinded again and passed through again, the procedure continued until the whole powder passed through. From Figure 12 (C&D), it can be seen that the HA particles are spherical with a particle size in the range of 50 nm to 100 nm. The morphology of SrHA and ZnHA is shown in Figure 12 (E-low magnification image & F-high magnification image) and Figure 12 (G-low magnification image & H-high magnification image) respectively. The particles were originally spherical and in nanometer range however, due to sintering at high temperature (900 °C), the nanoparticles fused together to form agglomerates. This phenomenon was also reported elsewhere [272, 273]. The fusion of particles can be seen more prominently in the SrHA and ZnHA samples. This may be due to the presence of the doping elements (Sr and Zn). These powders were ground and sieved through a 180 µm sieve to avoid any nozzle blockage during printing.

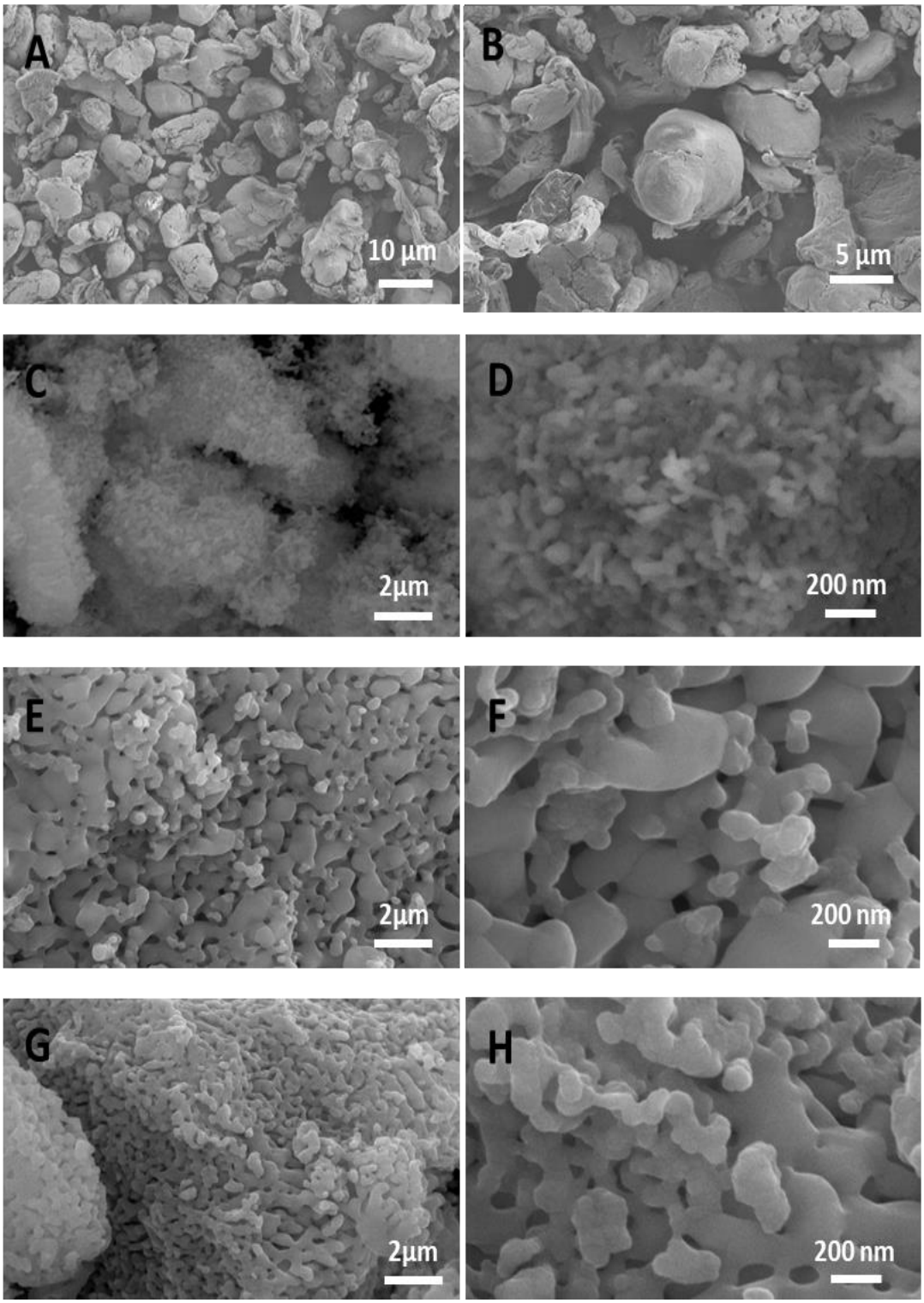

Figure 12 SEM micrographs of: raw PEEK powder (A&B), nano-HA (C&D), Sr doped nano-HA (E&F) and Zn doped nano-HA (G&H) synthesized by wet precipitation method and sintered at 900 °C (a low and a high magnification image of each)

4.1.2 Energy Dispersive X-ray Spectroscopy

EDX results of PEEK, HA, SrHA and ZnHA are shown in Figure 13. Three kinds of scanning were performed including point scan, area scan and mapping to confirm the presence of expected elements in the bioceramic particles. It can be seen that in pure PEEK sample, only carbon and oxygen were detected which was expected due to the organic nature of the polymer. These results were confirmed by area scan and mapping.

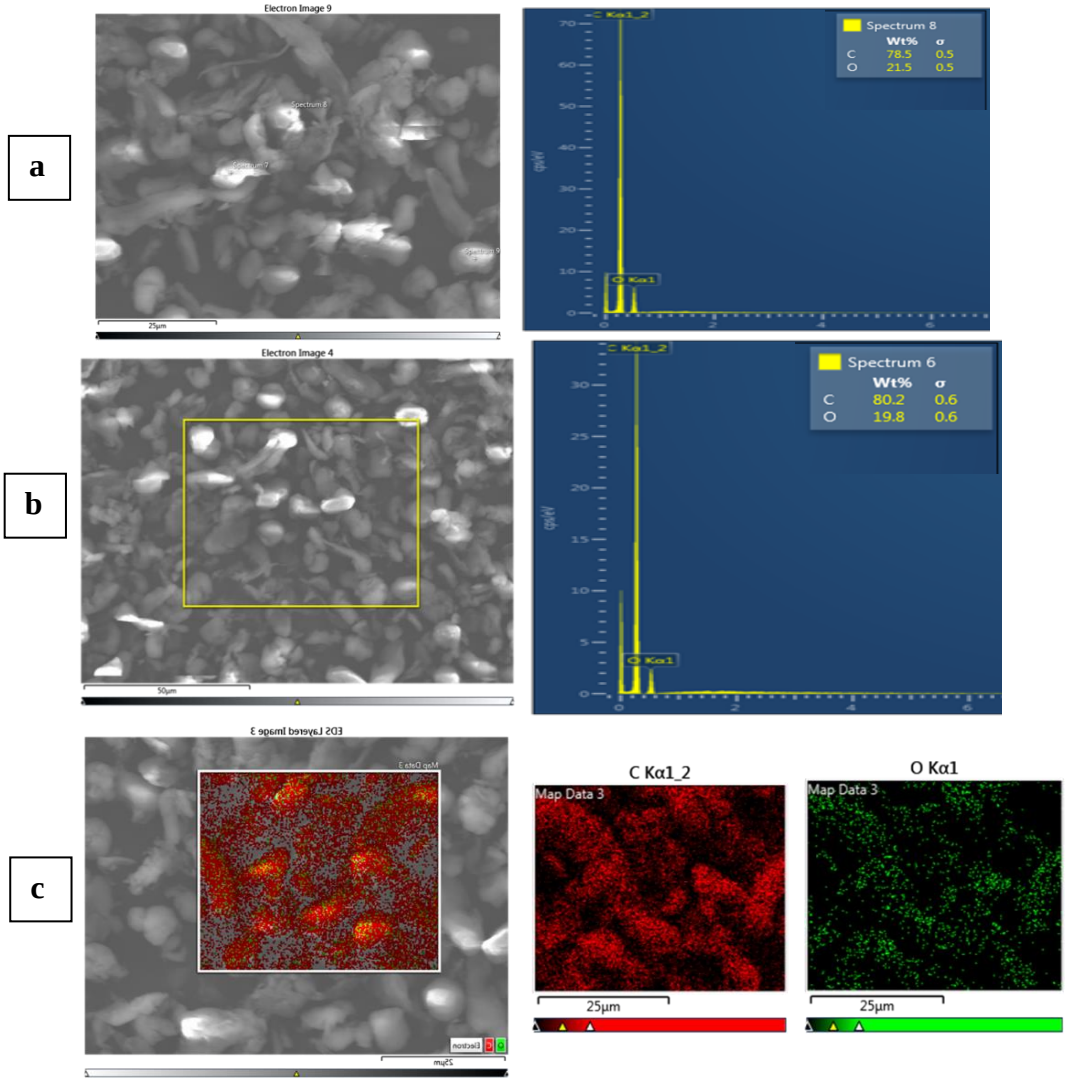

Figure 13 EDX analysis of PEEK powder for elemental composition, (a) point scan (b) area scan (c) mapping

For pure HA, the point scan at different regions detected the calcium (Ca), phosphorous (P) and oxygen (O) elements which was also confirmed by area scan of the powders [274]. Additionally, the distribution of the elements was observed by elemental mapping of Ca, P, O. The mapping results showed that the elements were present homogenously. Moreover, the presence of Sr in SrHA sample was detected by point scan along with Ca, P and O, these results were confirmed by area scan and mapping. The mapping also indicated the homogenous presence of Sr with other elements. Furthermore, the point scan of ZnHA sample detected the presence of Zn with Ca, P and O, their presence was confirmed by area scan and mapping of the sample. The uniform presence of Zn was confirmed by mapping analysis. The results have shown in Figure 14 and Figure 15 below.

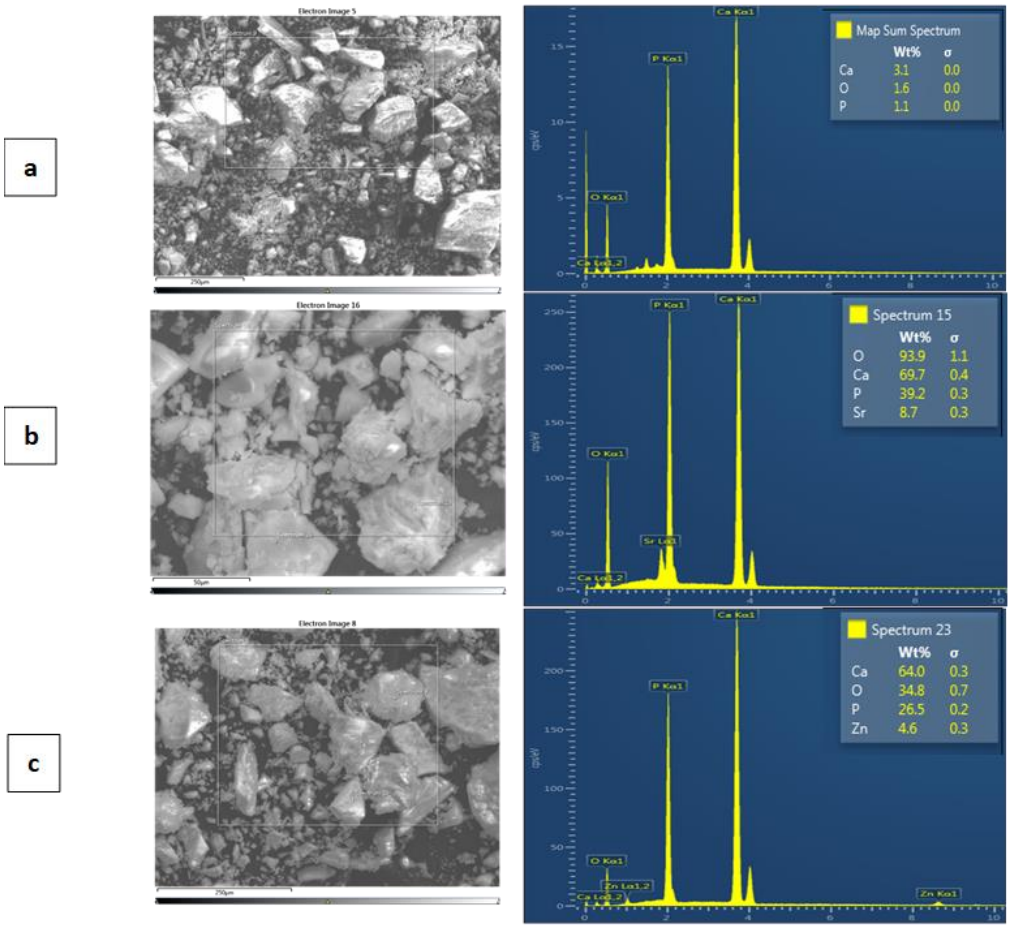

Figure 14 EDX analysis of sintered bioceramic powders produced via wet chemical synthesis (a) HA, (b) SrHA, (c) ZnHA

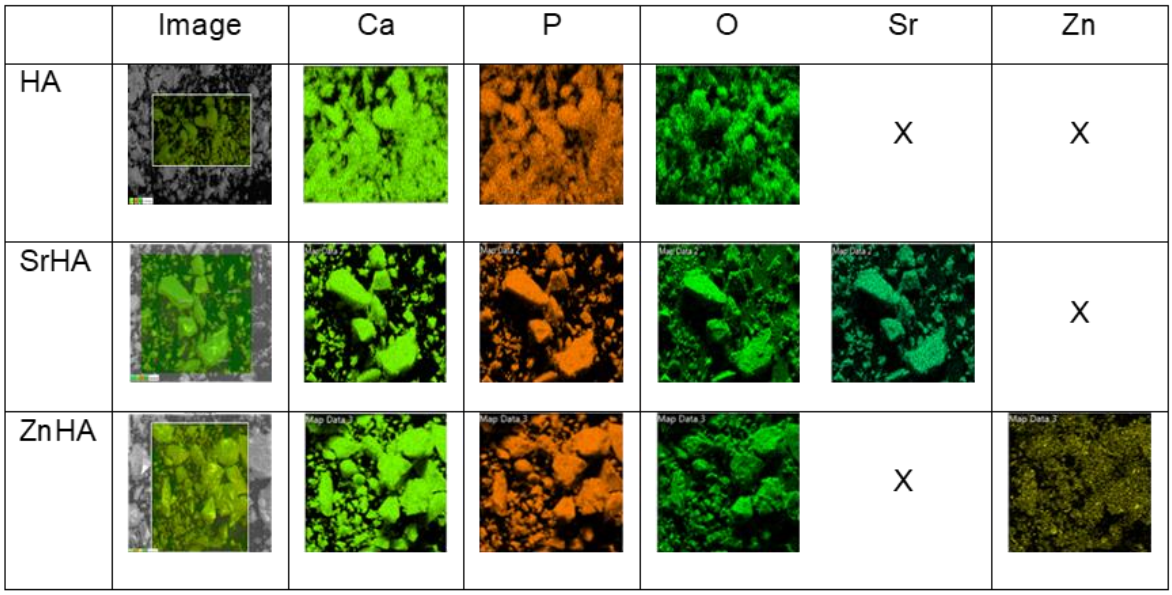

Figure 15 Elemental mapping of HA, SrHA and ZnHA synthesized by wet precipitation method, showing the elemental mapping by EDX analysis. Each colour in the figure represent specific element

Table 5 Ratios calculated in HA, SrHA and ZnHA through EDX analysis

	Ca/P	**Ca+Sr/P**	**Ca+Zn/P**
HA	2.8	--	--
SrHA	--	2.0	--
ZnHA	--	--	2.6

4.1.3 Thermal analysis

Figure 16 A and B show the TGA and DSC graphs of commercial raw PEEK powder, respectively. Figure 16 C and D show the TGA graphs of SrHA and ZnHA. The information in these graphs assisted to choose the extrusion and 3D printing temperatures which has been discussed in later chapters. TGA was performed to analyze the thermal stability and degradation temperature of the PEEK and bioceramic powders by heating the sample up to 700 C. In Figure 16A, it can be seen that the weight of the polymer was constant up to ~590 °C and degradation started after 590 °C (T_d). T_d provides the information regarding the maximum processing

temperature in extrusion and 3D printing of PEEK. The extrusion of filament and 3D printing of PEEK below T_d will not significantly degrade the polymer. Figure 16 B shows the DSC heat-cool-heat curve of PEEK powder. The first heating cycle was used to remove any thermal history present while in cooling cycle the crystallization temperature was measured. It can be seen from the curve shown in Figure 16 B that the crystallization of molten PEEK started at 285 °C and finished at 250 °C whereas the peak value of crystallization process was obtained at 270 °C. Furthermore, the glass transition temperature (T_g) of PEEK was measured as ~150 °C, the melting point was 345 °C and recrystallization temperature (T_c) was ~275 °C. This information helped in the selection of extrusion and 3D printing temperatures i.e., they should be between T_m and T_d. In Figure 16 C and 16 D, weight loss of SrHA and ZnHA samples have shown, respectively. The bioceramic powders are usually thermally stable [275-277]. Additionally, they were heat treated at 900 °C and any moisture present had been removed during that process. Hence, any wight loss detected was due to the removal of adsorbed water [275, 276]. The weight loss of SrHA and ZnHA powders heated up to 700 °C were measured as 1.57 % and 0.56 %, respectively which showed that they were thermally stale.

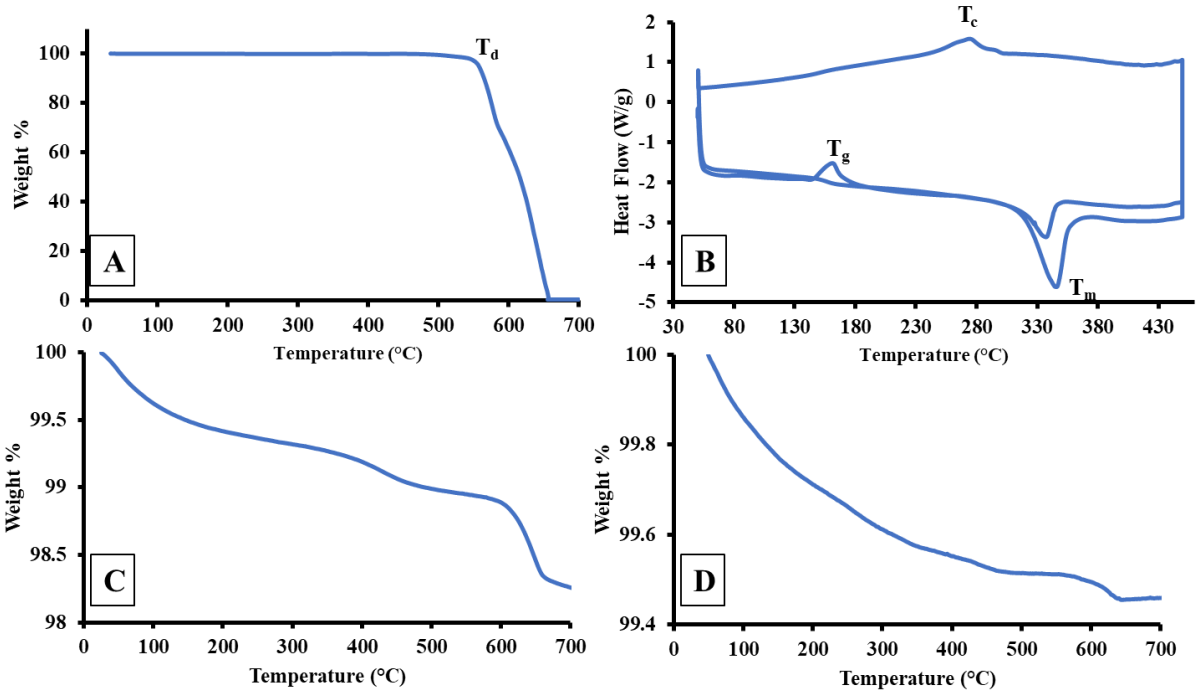

Figure 16 Thermal analysis of raw powders A) PEEK powder TGA curve up to 700 °C, B) PEEK DSC curve (heat cool heat), C) TGA curve of SrHA powder, D) TGA curve of ZnHA powder

4.1.4 Fourier Transform Infrared Spectroscopy

The FTIR of raw PEEK powder is shown in Figure 17. The carbonyl stretching vibration peak can be observed at 1655 cm^{-1}. The peaks at 1605 cm^{-1} and 1501 cm^{-1} are due to the in-phase vibration of the benzene ring [278]. The peaks due to the bending vibration of C-H out of plane appear at 920 cm^{-1} and 670 cm^{-1}. Several small sharp peaks in the region of 950 cm^{-1} and 1210 cm^{-1} are due to the in-phase bending of C-H while small and less intense peaks at 1750 cm^{-1} and 1240 cm^{-1} are due to the ketone and ether functional groups, respectively [279]. Aliphatic C-H vibrations can be observed at 2850 cm^{-1} and 3000 cm^{-1} [280].

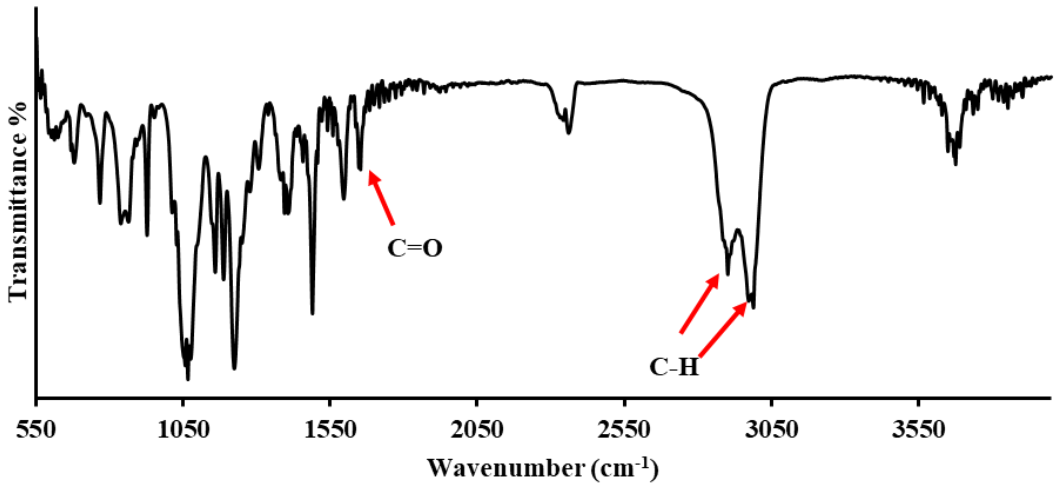

Figure 17 FTIR spectrum of PEEK powder obtained in ATR mode

FTIR spectra of synthesized HA, SrHA and ZnHA powders are shown in Figure 18. The vibrational modes of each functional group present in the powders were observed by FTIR which confirms the chemical composition and phase purity. The graph obtained by this technique is in the form of unique pattern which contains characteristic peaks of each functional group at specific wavenumber as well as intensity.

A typical FTIR spectrum of HA powder in the range of 4000 cm^{-1} t0 400 cm^{-1} has been given in Figure 18. In the spectra, a peak at 3565 cm^{-1} was correspond to the stretching of O-H functional group while peak at 635 cm^{-1} was due to the liberation vibration of O-H which was expected in accordance with the literature [14]. A broad band peak between 1600-1740 cm^{-1} was

due to the bending of O-H-O molecules of physically adsorbed water trapped in HA powder during its wet synthesis.

The vibrational modes correspond to P bonds are v_1, v_2, v_3 and v_4. The typical stretching vibration of the P-O bond can be seen at 1200 cm^{-1} and 900 cm^{-1}. The fundamental modes of PO_4 tetrahedron can be observed at 1025-1085 cm^{-1} (v_3), with a small shoulder peak at 960 cm^{-1} (v_1), O-P-O bending at 562 cm^{-1}, and 604 cm^{-1} (v_4) while v_2 vibrational mode appears at 475 cm^{-1} [281].

The stretching and bending mode of O-H appear at 630 cm^{-1} and 3550 cm^{-1}, respectively [282]. However, due to the presence of doping elements (Sr, Zn), a slight shift in peaks can be observed [283, 284] in Figure 18. A summary of the peak allocations is presented in Table 6.

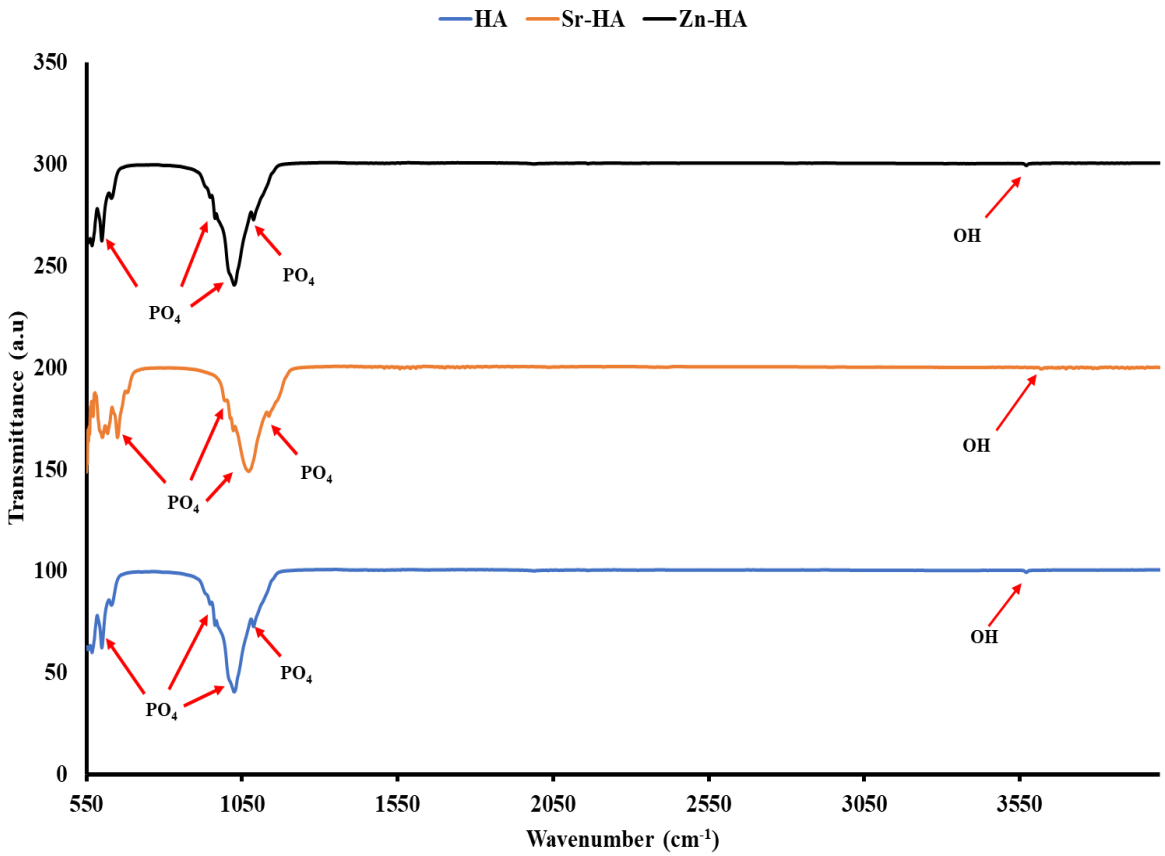

Figure 18 FTIR spectra of HA, SrHA and ZnHA synthesized by wet precipitation method and sintered at 900 °C

A typical FTIR spectra of SrHA has shown in Figure 18 is very similar with the spectra of HA, however there are few variations. In SrHA, the absence of the both stretching and bending of O-H-O molecule was observed. The stretching vibration of OH which is measured at 3570 cm^{-1} have clearly seen with decreased intensity while the liberation vibration which is typically appeared at 630 cm^{-1}, was absent in SrHA spectra. Additionally, the stretching band of OH appeared at higher wavenumber. The peaks appeared between 1400-1500 cm^{-1} represent SrHA at 1414 cm^{-1}, 1455 cm^{-1} and 1558 cm^{-1}.

The stretching peaks due to P-O were appeared at two different positions between 950-1100 cm^{-1}, more specifically at 1030 cm^{-1} and 1090 cm^{-1}. Relative to HA spectrum, this band has weaker peak intensity and appeared at lower wavenumber. Moreover, P-O stretching v_1 in phosphate was detected at 955 cm^{-1}. Finally, the peaks 560 cm^{-1} and 600 cm^{-1} are due to the bending mode of O-P-O. However, peak 560 cm^{-1} appeared at higher wavenumber as detected in HA i.e., 562 cm^{-1}.

The typical spectra of ZnHA was shown in Figure 18. The pattern was similar to that of HA, however there was slight variations observed. All characteristic peaks associated with HA appeared as expected. The intensity of O-H stretching peak (3550 cm^{-1}) was reduced as compared to HA (3565 cm^{-1}) while the peak associated with the liberation mode found to be absent. Additionally, there was no broad bands of O-H-O molecules detected due to its stretching or bending. The stretching modes of O-P-O bonds in phosphates appeared at two sites in the range of 1100-990 cm^{-1}, specially at 1100 cm^{-1} and 1035 cm^{-1} as compared to HA (1094 cm^{-1} and 1033 cm^{-1}, respectively), the peak at 1105 cm^{-1} appeared as a small shoulder peak due to Zn substitution. The other peak due to the stretching of P-O bond detected at 965 cm^{-1}. The peaks associated with the bending of O-P-O mode appeared at 565 cm^{-1} and 604 cm^{-1}. The presence of Zn in HA had shifted the wavenumber to higher values 1420 cm^{-1}, 1471 cm^{-1} and 1569 cm^{-1} as compared to the peaks of HA (1417 cm^{-1}, 1462 cm^{-1}, 1558 cm^{-1}).

Table 6 Summary of peak positioning of hydroxyapatite and doped-hydroxyapatite functional groups

Material	**$[PO_4]\nu_4$ cm^{-1}**	**$[PO_4]\nu_3$ cm^{-1}**	**OH cm^{-1}**
HA	562, 604	960, 1025, 1092	630, 3550
SrHA	570, 610	980, 1080, 1130	610, 3590
ZnHA	572, 610	975, 1080, 1130	610, 3590

4.1.5 X-Ray Diffraction

The crystallinity and phase purity of HA, SrHA and ZnHA powders have been observed by XRD analysis and the results have been shown in Figure 19. The XRD pattern of HA obtained after the analysis has been provided in Figure 19. The results showed that the synthesized bioceramic powders were mixture of HA and β-TCP. The HA diffractogram was compared with International Center of Diffraction Data (ICDD) files 00-09-432 and 00-09-169. The characteristic peaks of HA at 2θ values of 26.1°, 32.0°, 32.4° and 33.1° related to planes (002), (211), (112) and (300), respectively [285]. There were additional peaks which were related to β-TCP which were due the thermal decomposition of HA [286]. The sharp and well-defined peaks indicate that the structure of HA is crystalline. This pattern resembles biogenic HA that occurs naturally in bone and dentin [287, 288].

The XRD pattern of SrHA has shown in Figure 19. The peaks matched with the peaks that appeared in HA diffractogram, however, their intensity decreased. More prominent peaks of β-TCP were observed which showed its formation during sintering of SrHA sample. However, the peaks shifted to the lower 2θ values and with broadened area. Hence, Ca^{+2} in the HA lattice is replaced by Sr^{+3} which is evident in their respective spectra by observing peak shifting, reported elsewhere [283, 285]. The broadness of peaks related to crystal growth which was suppressed in the presence of Sr.

The XRD pattern for ZnHA powder has shown in Figure 19. The obtained peaks were matched with the β-TCP and HA pattern. The peaks corresponded to HA were less intense as

compared to the peaks corresponded to β-TCP. However, the peaks shifting to lower 2θ values and broadening of peaks confirmed the substitution of Zn^{+2} in HA by replacing Ca^{+2}. The slight shifting and appearance of small new peaks confirmed the successful doping of Sr and Zn in HA.

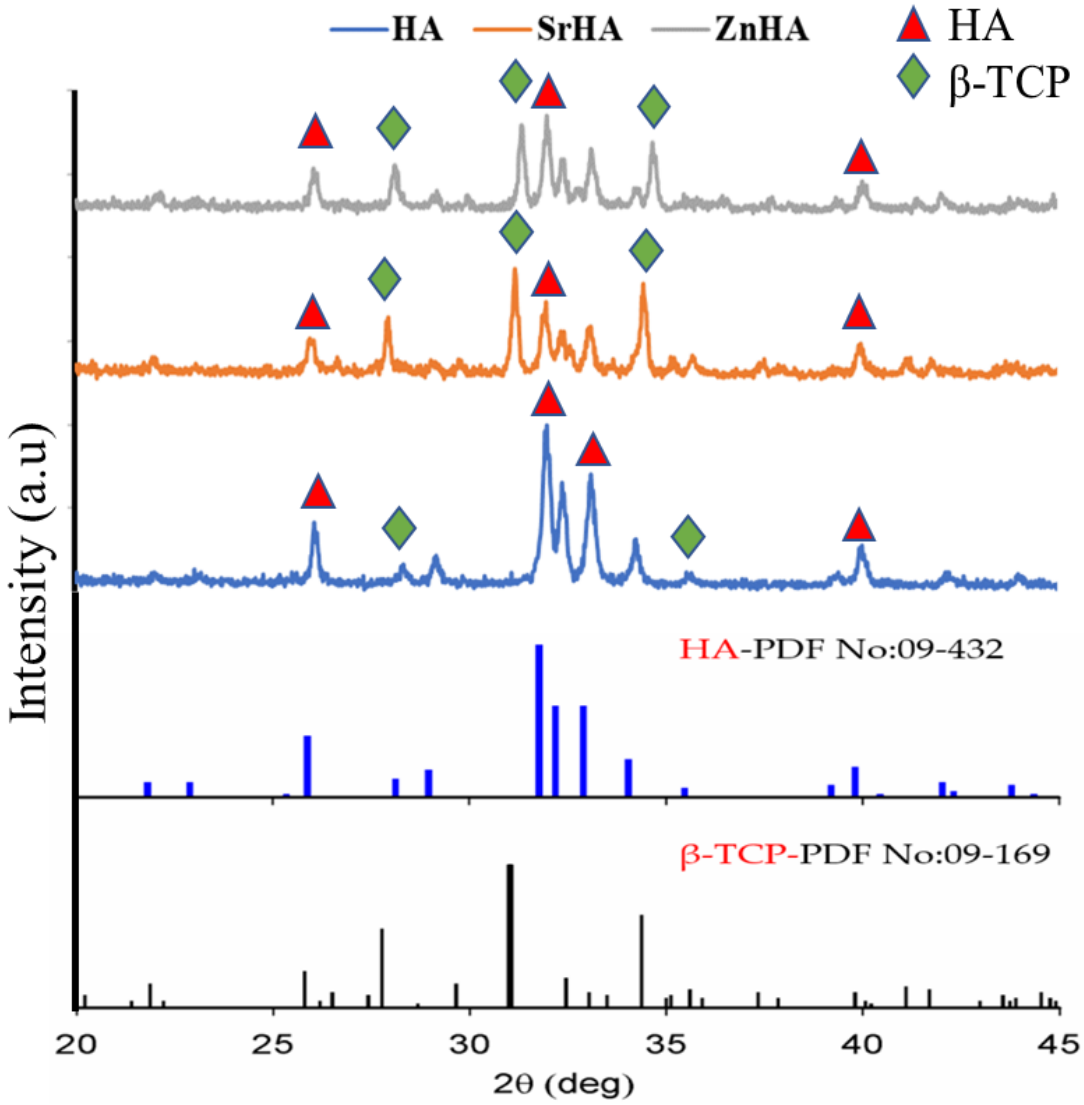

Figure 19 XRD spectra of bioceramic powders prepared by wet chemical precipitation method and sintered at 900 °C

4.2 Discussion

Chemically, HA resembles with the mineral phase of the human bone which constitutes 60 % and having size in the range of 5 to 60 nm [289]. It can be synthesized in the laboratory by several methods such as hydrothermal method, precipitation method, solvothermal method, spontaneous combustion method, ultrasonic synthesis method, bionic method and solid-state reaction method. Each of the method has its own advantages and limitations. In this study, HA and its doped forms were prepared by wet chemical precipitation method. Additionally, the beneficial effects of doping elements have been well documented in the previous studies. The increase in bioactive potential due to the presence of doping elements in HA have been recorded within the literature as well. In order to further investigate the chemical and physical properties of synthesized HA and confirming the presence of doping elements in HA, various techniques have been used. Initially, physical (SEM), thermal (DSC, TGA) and chemical (EDX, FTIR, XRD) properties were investigated to ascertain the quality of raw materials from which samples were produced. An in-depth understanding of main characteristics of each powder, with regard to each aforementioned analytical technique, began the formation of the solid foundation upon which knowledge could be built.

The morphology and particle size of the powders were investigated through SEM. Due to the procedure adopted for the synthesis of HA and doped HA, it was assumed that the particle sizes would be in the nanometer range which was confirmed by SEM. The particles of HA were observed round in shape with an average diameter of 40 nm and the particles were fused together due to the sintering of HA powder at high temperature (900 °C) which was required to make HA crystalline. This was aligned with the reported literature that the wet-precipitation method is an effective way of synthesizing HA nanoparticles which were in the range of apatite crystals sized present in human bone [267]. Apart from the apatite present in human bone being in the nanometer range, there are some additional advantages that nanoparticles offer over a bulk material such as large surface area, good dispersion in composites, offers good biological interactions, etc. Similarly, the morphology of SrHA particles was round, the average particle size was 80 nm which was slightly bigger than HA and ZnHA and they had fused together in a similar fashion due to the sintering.

The elemental analysis performed by EDX confirmed that there was not any major elemental impurity present that could affect the final properties of the materials. That was confirmed by acquiring data from various type of scans such as area scan, point ID scan and mapping. As PEEK is an organic compound so the scan confirmed that the as received PEEK powder was mainly composed of carbon and hydrogen. HA was synthesized by using various raw materials so there were chances of residual impurities due to the incomplete washing of HA precipitates. The powder was spread on the carbon conducting tape and the point scan was captured at different sites. Similarly, area scans were captured randomly at different sites. Hence, both the analysis showed that it was comprised of Ca, P and O which are the main constituents of HA. The mapping scan of HA showed the evidence of Ca, P, O present in the powder. Moreover, Sr element was detected at different sites of point ID and area scans which confirmed the presence of Sr in the SrHA powder along with Ca, P and O. The mapping scan of SrHA suggested that the Sr element was present uniformly in the powder where there was Ca, P and O were detected. Furthermore, ZnHA powder was scanned via point ID and area at different sites of the powder spread on carbon tape, it was observed that Zn was detected in those scans. The uniform presence of Zn along with Ca, P and O was observed by mapping scan which indicated the homogenous doping of Zn in HA. The stoichiometric HA has Ca/P ratio equal to 1.67. The value changed due its decomposition during sintering at high temperature. The decomposition of HA started at sintering temperature above 750 °C into β-TCP and CaO. The formation of β-TCP and CaO resulted in a Ca deficient and Ca rich HA, respectively [290]. In Table 5, Ca/P, Ca+Sr/P and Ca+Zn/P ratios greater than 1.67 were due to the decomposition of HA during sintering.

Thermal behavior of PEEK powder which was the point of interest, was observed by the TGA and DSC analysis. PEEK is a thermoplastic high-performance polymer with semi-crystalline structure. Semi-crystalline polymers have both the mixture of ordered and amorphous regions. Due to the high melting point of PEEK and the presence of aromatic rings, it is considered as thermally stable and chemically inert polymer, respectively. The thermal degradation of PEEK started at 580 °C measured by TGA which is quite high and thus provide a long range of serviceable temperature. That temperature gave an idea for setting its working temperature during filament extrusion and 3D printing of the samples. It was observed that the PEEK degraded at a faster rate after the degradation started and completely degraded at 660 °C. The DSC curve provided the information of T_g, T_m and T_c. PEEK is a semi-crystalline polymer, and the degree of crystallinity depends upon

crystallization kinetics of melting and recrystallization which in turn strongly dependent on the heating and cooling rates. In this study, the PEEK powder was heated and cooled at a constant rate of 10 C/min. The glass transition temperature was measured as 143 °C; it is the temperature at which the polymeric chains of a polymer started to move freely, and the solid material turned into soft rubbery material. Additionally, the melting peak was observed at 343 °C; it is the temperature at which crystalline regions melt into liquid state. When the molten polymer is cooled, it starts to crystallize again by releasing energy called heat of crystallization and the temperature is called crystallization temperature. For pure PEEK, it was observed that the recrystallization started at 280 °C with peak value at 275 °C and finally ended at 270 °C.

FTIR analysis showed the degree of chemical similarity between all PO_4 and OH band positions and intensities. The shifting of peak positioning, lowering of intensities and broadening of peaks in SrHA and ZnHA spectrum as compared to HA was due to the doping of Sr and Zn in HA.. Similarly, the peak shifting to slightly lower and higher wavenumbers in SrHA and ZnHA samples (as compared to pure HA) was due to the presence of Sr and Zn.

A number of trends within FTIR were found to correlate with XRD results for Sr and Zn powders. Although, the patterns of β-TCP and HA were matched with ICDD file numbers 00-09-169 and 00-09-432, however a considerable shifts of diffraction peaks were observed to lower or higher 2θ values. During sintering at 900 C, HA decomposed into β-TCP and CaO. Hence, all HA was not decomposed so less intense peaks were observed in the samples. The decomposition temperature of HA decreased in the presence of doping elements, due to that fact higher intensities of β-TCP peaks were observed in SrHA and ZnHA samples. The peaks also showed the decrease or increase in intensities which were due to the presence of Sr and Zn ions. The width of the peaks was remained almost constant which indicated that the d-spacing and crystallite size remained same, hence presence of Sr and Zn hardly affected the crystallinity. Additionally, the mergence of peaks at 2θ 27.1° and 28.6° was also the evidence of Sr and Zn incorporation in HA. Kavitha et al. [291] reported that the mergence was either due to the formation of nano sized crystallites or substitutional micro strain. The broad peaks in SrHA and ZnHA samples were due to the fact that the doping elements inhibit the crystal growth of HA. The EDX, FTIR and XRD results corroborated the fact that SrHA and ZnHA are not pure. There are peaks of β-TCP which are confirmed through XRD analysis. It has been reported that the HA starts to decompose into other

phases when heated above 800 °C [286, 292, 293]. Enhanced osteoblastic cell response was reported by TCP derived surfaces in terms of cell adhesion and cell proliferation [293]. The chemical equation for thermal degradation of HA into β-TCP has been given below:

$$Ca_{10}(PO_4)_6(OH)_2 \text{ ---------- } 3Ca_3(PO_4)_2 + CaO + H_2O \ldots\ldots\ldots\ldots (5)$$

5 Chapter 5: Characterizations of PEEK filaments and its bioactive composites

5.1 Introduction

Recently, strong emphasis has been laid on making prosthesis by material extrusion-based additive manufacturing, also called fused filament fabrication (FFF), fused filament fabrication (FFF) or simply 3D printing [294, 295]. In this type of 3D printing, a thermoplastic polymeric filament is used as feedstock. The quality of the final 3D printed parts depends upon the quality of the filaments used for 3D printing. Hence, evaluating the quality of feedstock filaments is essential [296]. The quality is affected by the presence of surface defects such as voids, pores or cracks as well as distribution of the particles and diameter of the filament. These defects could be present due to the presence of moisture or trapped air bubbles. As thermoplastic polymers absorb moisture at room temperature. It is more prominent especially in polymeric powders because powders have a high surface area and hence can absorb moisture easily. During the extrusion process at high temperatures, when the moisture leaves, it creates a small cavity or pore. Additionally, inappropriate selection of extrusion temperature results in a trap of air bubbles which cause surface defects. When the filaments containing defects are used in the 3D printing process, they transform these defects into 3D printed objects in the form of cavities thus reducing the mechanical properties of final 3D printed objects [297]. Moreover, the non-uniform distribution of the particles greatly affects the mechanical and biological performance of the part due to the agglomeration. Also, the inconsistent diameter of the filament can cause serious complications and can affect the quality of 3D printed parts. For example, the diameter smaller than 1.75 mm has lack of material and hence cause pores during 3D printing and vice-versa. Moreover, unexpected smaller diameter is not able to grip the filament because of lack of tension, causing extrusion stop. On the other hand, the larger diameter filament does not fit in the opening of the nozzle and unable to proceed. The gold standard of filament tolerance is +/- 0.05 mm in industry, sometimes 0.10 mm is also acceptable, however, lowest is the better [298]. In this chapter, the produced filaments are characterized by various techniques such as scanning electron microscopy (SEM) was used to analyze surface morphology and bioceramic particle distributions, energy-dispersive X-ray spectroscopy (EDX) was used to measure the elemental composition, micro-computed tomography (μ-CT) was used to analyze the internal porosity and distribution of the particles, Fourier transform infrared spectroscopy was used to detect the functional groups present in the composites, differential scanning calorimetry (DSC)

was used to find the melting, crystallization and glass-transition temperatures and thermogravimetric analysis (TGA) was used to find the thermal degradation with respect to temperature change.

5.2 Filament optimization

The dried mixtures of powders were used to prepare filaments with diameter 1.75 ± 0.05 mm with the help of commercial desktop extruder i.e., 3devo Composer 450, as shown in Figure 22. In order to prepare uniform diameter filaments, various extrusion parameters were optimised such as powder feeding rate, extrusion speed, temperatures of different zones, cooling rate, puller wheel speed and nozzle diameter. All the parameters have positive or negative effect on the final diameter of the filaments such as increasing the powder feeding rate, extrusion speed and cooling rate increase the final diameter while increasing the speed of puller wheel decreases the diameter. The powder was fed into the extruder through a hoper. However, due to the low density of the powder, it did not go into the extruder by its own. Hence, the powder was fed manually with continuous and constant rate. Inappropriate and non-uniform pressing (feeding rate) resulted in a non-uniform diameter filament. The filaments obtained during and after optimization have shown in Figure 20 and Figure 21 below, respectively.

Figure 20 Non-uniform diameter of PEEK nanocomposite filaments obtained during optimisation via 3devo desktop extruder

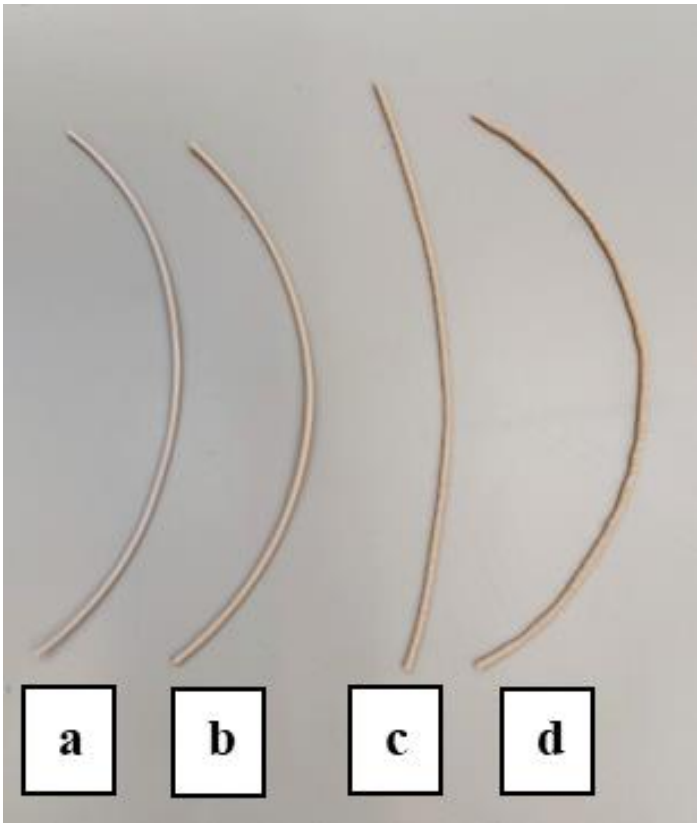

Figure 21 PEEK nanocomposite filaments prepared after optimisation via 3devo desktop extruder; a) PEEK, b) PEEK/10SrHA, c) PEEK/20SrHA, d) PEEK/30SrHA

Moreover, the fine control of temperature was very crucial as the viscosity of the melt depend on the temperature as well as filler content. The fed powder had passed through four different heating zones which were present in the extruder and labeled as H1, H2, H3, H4. The temperature of each heating zone was controlled manually. The H1 heating zone was close to the powder feeding hoper while the H4 heating zone was close to the nozzle where the material left the extruder in molten form. The temperature of the H1 heating zone was set just above the melting point of the powder and then gradually increased so that it had appropriate viscosity when coming out from the nozzle. The air bubbles were seen in the filaments when the temperature of the H1 zone was quite high such as 370 °C. The nozzle of the extruder was pointed downward so that material came out easily due to gravity.

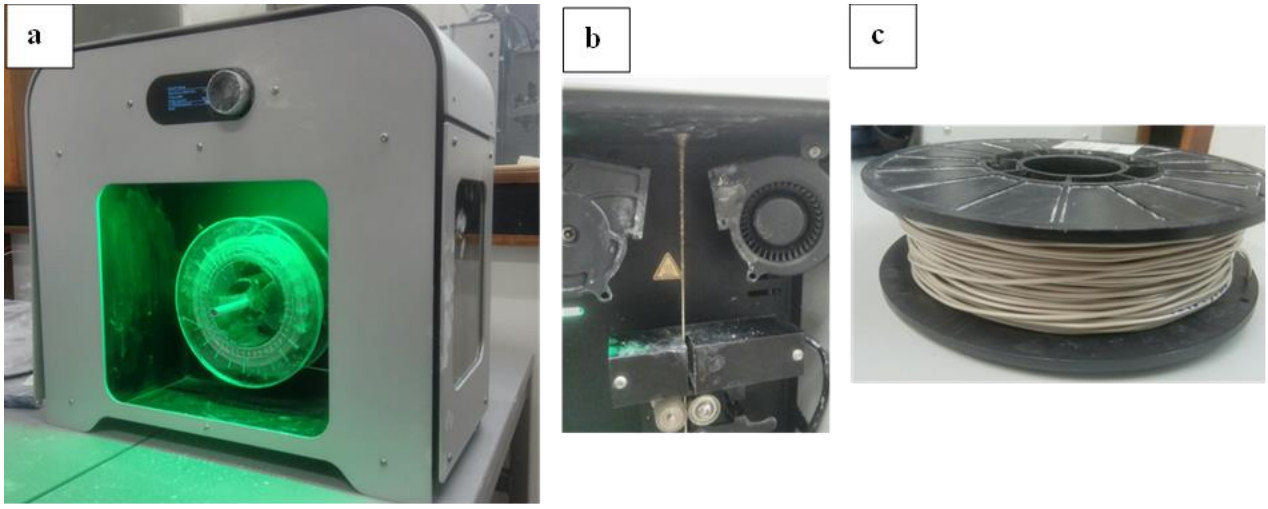

Figure 22 Production of filament via extrusion process, (a) desktop extruder, (b) molten polymer coming out from nozzle, (c) final filament

Furthermore, the material after passing through the cooling zone fed into the puller wheels. The cooling rate of the molten material was controlled by the speed of cooling fans located near the nozzle which propelled air on the molten material and solidified it. The puller wheels directly pulled the material from the nozzle and directed to the spool where it wound. Hence, the diameter of the filaments was controlled by adjusting the speed of the puller wheels. The non-uniform diameter of filaments with beads were produced when the cooling rate and the speed of puller wheels were inappropriate. Hence, by carefully adjusting all the parameters as discussed above, constant diameter filaments were produced. In Table 7 below, summary of final optimized parameter has been provided.

Table 7 Optimised parameters for preparing 1.75 ± 0.05 mm diameter filaments for PEEK and its nanocomposites using a desktop extruder

Parameters/ material	**PEEK**	**PEEK/10SrHA and PEEK/10ZnHA**	**PEEK/20SrHA and PEEK/20ZnHA**	**PEEK/30SrHA and PEEK/30ZnHA**
Temperature (°C) Z_1, Z_2, Z_3, Z_4	355, 365, 375, 390	360, 370, 380, 400	365, 380, 400, 410	380, 400, 410, 420
Feeding rate (g/min)	3.3	2.8	2.3	2.1
Extruder Screw speed (RPM)	5.5	5.5	5.5	5.5
Cooling fan speed (%)	100	90	80	80
Nozzle diameter (mm)	12	12	12	12
Puller wheel speed (RPM)	1100	1000	950	900

5.3 Optimization of 3D printer with polyetherimide

3D printing of high-performance polymers is challenging due to its very high processing temperatures. Prior to the 3D printing of PEEK, polyetherimide (PEI) was selected for the optimization of printing parameters via SpiderBot 4.0 HT FFF 3D printer. As discussed in previous section that PEEK is a semicrystalline polymer and exhibits high shrinkage in cooling so that is

why its 3D printing is challenging. On the other hand, PEI is a high performance amorphous thermoplastic polymer. Due to its amorphous nature, it is less susceptible to the shrinkage during its cooling. PEI Ultem 1010 filament was purchased from 3d4makers for optimization purpose. The samples were printed on PEI print bed. Initially, the first layer was not adhering to the print bed; hence, a thin layer of paper glue was applied to solve this problem. Another problem that was arising that the prints were failed during the printing due to the detaching from the print bed. Hence, higher bed temperature was used to solve that problem. For example, initially the prints were failed at 90 °C, however, the problem was overcome when bed temperature was raised gradually up to 120 °C. Additionally, the samples were shrinking at the set temperatures i.e., 360 °C and 50 °C printhead and chamber temperatures, respectively. Hence, this problem was overcome by increasing head and chamber temperatures up to 370 °C and 60 °C, respectively. After successful 3D printing, the samples were characterized by Scanning electron microscopy (SEM), energy dispersive X-ray spectroscopy (EDX), thermogravimetric analysis (TGA), differential scanning calorimetry (DSC), compression testing and impact testing. The optimised 3D printing parameters for PEI polymer have been summarized in Table 8 below.

Table 8 Optimised 3D printing parameters of PEI samples

Parameters	**PEI**
Nozzle temperature (°C)	360
Bed temperature (°C)	120
Chamber temperature (°C)	50
Layer thickness (mm)	0.2
Printing speed (mm/s)	30
Infill density (%)	50, 100
Infill pattern	Concentric
Nozzle diameter (mm)	0.5

5.4 Scanning Electron Microscopy

The distribution of bioceramic particles, agglomeration, surface voids and surface morphology of the composite filaments were observed via SEM. Any moisture present in the raw materials before processing and inappropriate extrusion temperature settings could cause the presence of voids. In order to avoid these, the raw powders which were used for processing filaments were completely dried and the extrusion temperature was optimized. The quality of filaments was confirmed via SEM as shown in Figure 23. In Figure 23 A, the surface of pure PEEK filaments showed the absence of any bioceramic particles, as expected. Additionally, it was observed that the surface was free from any major voids or pores. The slight roughness on the surface was due to the extrusion process itself. The SEM images of the pure PEEK filament surface has shown in Figure 23 A.

Figure 23 (B to G) shows the SEM images of PEEK composite surfaces. Figures 23 B and Figure 23 E show the surfaces of PEEK with 10 wt.% of SrHA and ZnHA, respectively. It was observed that the bioceramic particles were well dispersed on the surfaces without any significant agglomeration. Additionally, the surfaces were free from surface defects such as pores or cracks.

Figure 23 C and Figure 23 F show the surfaces of PEEK with 20 wt.% of SrHA and ZnHA, respectively. It can be seen that the extent of bioceramic particles increased as compared to 10 wt.%. The dispersion of the particles was uniform and not any significant agglomeration was observed. Also, the surface was mostly uniform without the presence of surface defects such as pores or voids.

The surfaces of PEEK composites with 30 wt.% of SrHA and ZnHA has shown in Figure 23 D and Figure 23 G, respectively. The amount of bioceramic particles was maximum as can be seen by the white phase. In some areas, the agglomeration can also be seen. This shows that the percolation threshold is between 20 wt.% and 30 wt.% of bioceramic particles.

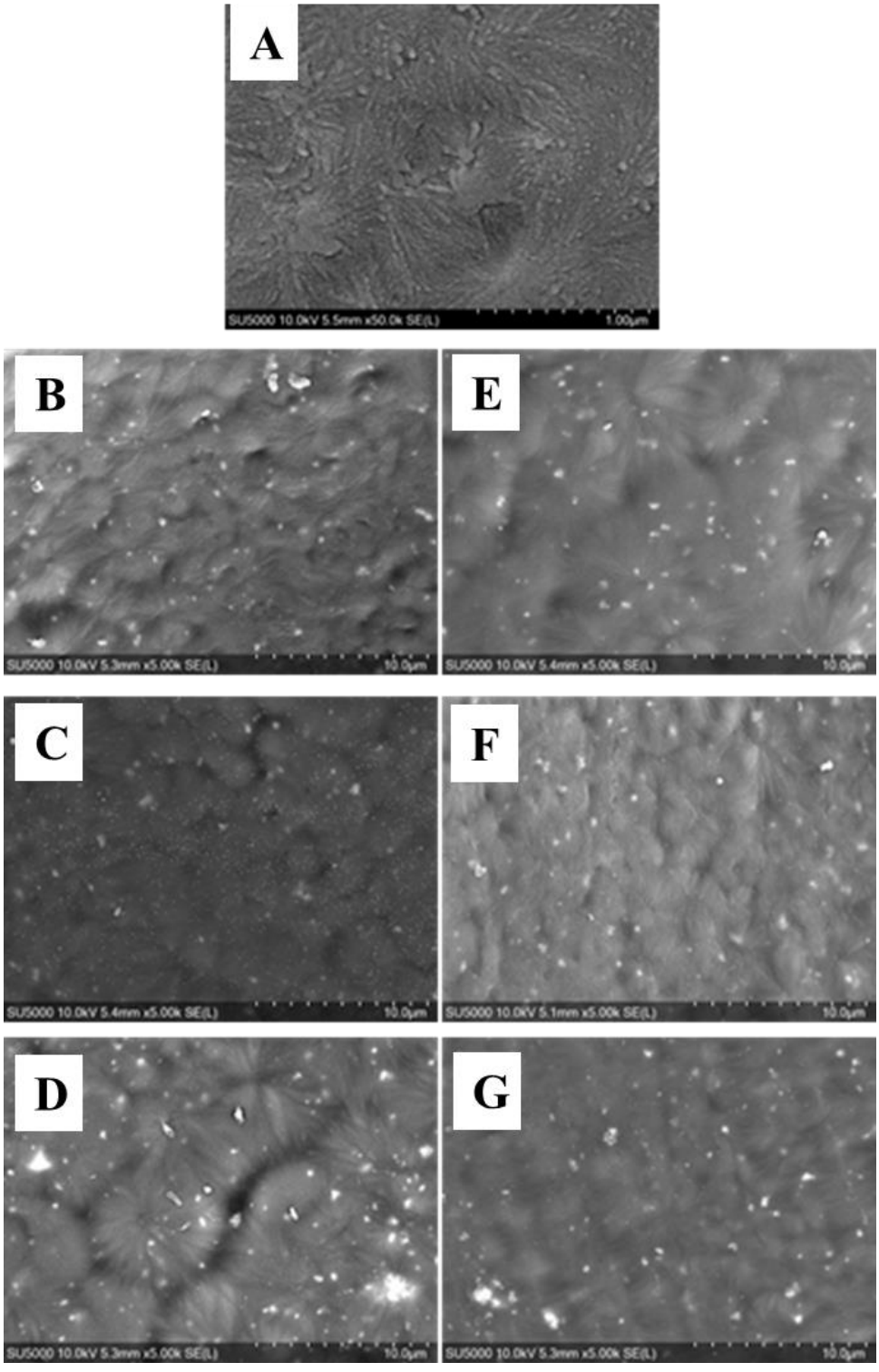

Figure 23 SEM analysis of top surfaces of filaments, (A) PEEK, (B) PEEK/10SrHA (C) PEEK/20SrHA (D) PEEK/30SrHA (E) PEEK/10ZnHA (F) PEEK/20ZnHA (G) PEEK/30ZnHA

5.5 Energy Dispersive X-ray Spectroscopy

EDX analysis confirmed the elemental composition and distribution of the bioceramic particles in the PEEK composite filaments. This was done by performing point scan, area scan and mapping scan as shown in Figure 24. For pure PEEK filament samples, it has been observed that the samples showed the presence of C and O, as expected due to the organic nature of the polymer. Additionally, no other unwanted elements were detected after processing the powder by extrusion technique. For PEEK with 10 wt.% HA composite sample, point scan and area scan confirmed the presence of Ca, P and O due to HA and C and O due to PEEK polymer. The mapping scan confirmed the uniform distribution of HA in the PEEK matrix. Moreover, PEEK with 10, 20 and 30 wt.% SrHA samples were analyzed, and it was observed that the Sr was detected in all samples along with other elements such as Ca, P, O and C by point and area scans taken at different regions. The mapping analysis showed that the SrHA particles were uniformly distributed. The intensities of elemental peaks belong to SrHA such as Ca, P and Sr were increased, and the elemental analysis of the peak belong to PEEK polymer such as C was decreased by increasing the percentage of bioceramic particles from 10 to 30 wt.%. However, no significant variation was detected in the O peak, this could be due to that O was present in both SrHA and PEEK. These results were aligned with the mapping scans. The mapping showed that the amount of particles increased on the surface as the weight percent of particles increased from 10 to 30 wt.%. Additionally, some clusters of particles were detected on the surface of 30 wt.% sample. These results were corroborated what was observed in SEM analysis. Furthermore, the point and area scans of ZnHA composite filaments samples detected the presence of Zn along with Ca, P, O, C in PEEK/ZnHA composite samples. Similar trend was observed that the elemental peak intensities corresponded to Ca, P, Zn were increased while C peak was decreased as the weight percent was increased from 10 to 30 wt.%. Also, the bioceramic particles cluster were detected on the surface of the sample contained 30 wt.% ZnHA as observed in SEM analysis.

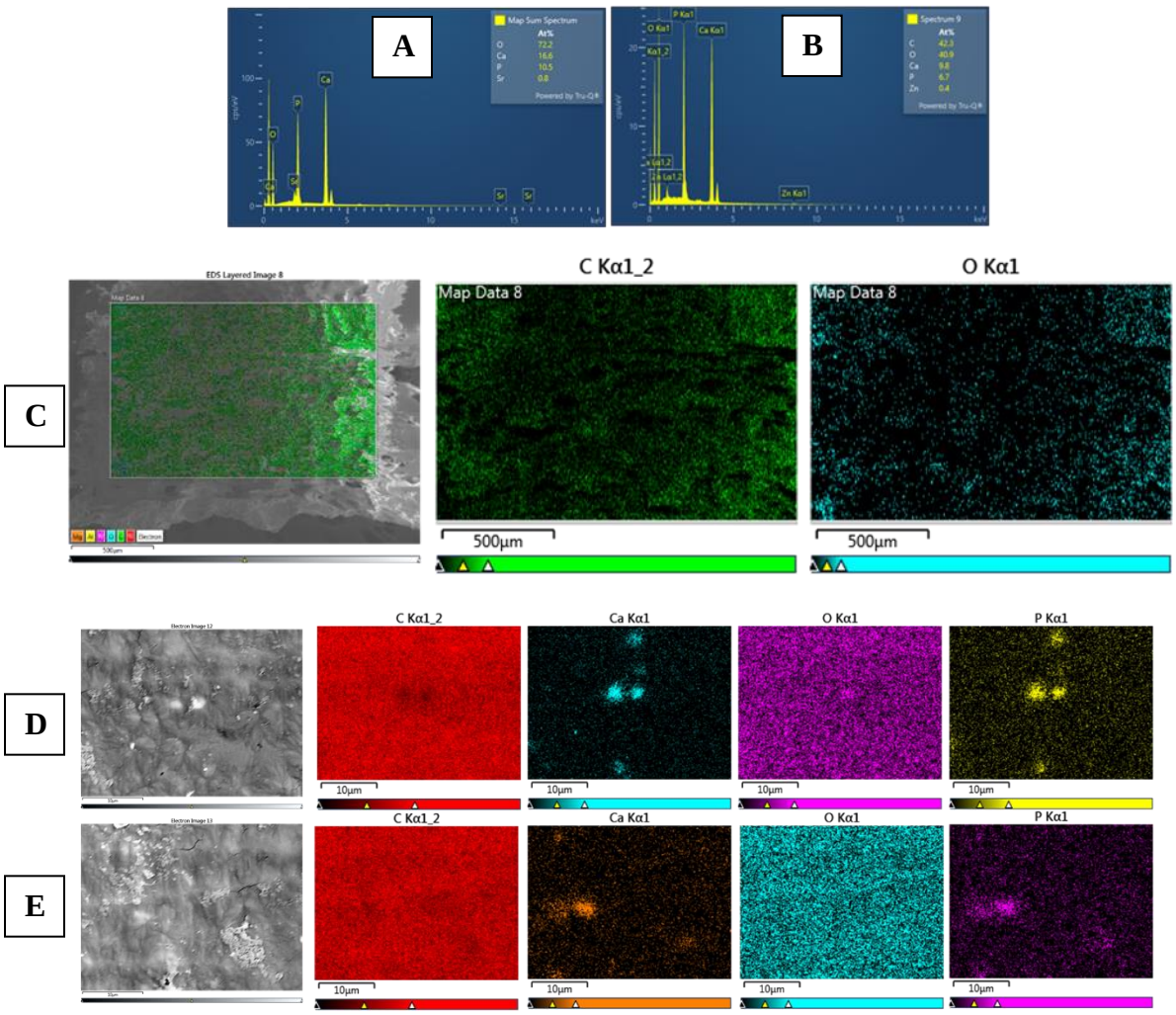

Figure 24 EDX results of PEEK and its composites obtained after point, area and mapping scans, A) PEEK/10SrHA area scan, B) PEEK/10ZnHA area scan, C) PEEK mapping, D) PEEK/10SrHA mapping, E) PEEK/10ZnHA mapping

5.6 Micro-Computed Tomography

The internal structure of the filaments such as bioceramic particle distribution, agglomeration and the presence of internal pores or voids can be observed via µ-CT as shown in Figure 25. Three samples for each material at different locations were analyzed to check the repeatability of the results. The filaments of pure PEEK showed smooth surface without the presence of any particles and there was negligible porosity. However, the presence of bioceramic particles can be seen in 10 wt.% SrHA and ZnHA filament samples, as expected. The increased

amount of particles can be seen in 20 wt.% and 30 wt.% samples. Additionally, some agglomeration was observed in 30 wt.% SrHA and ZnHA samples. The agglomeration of nanoparticles is a common problem in nanocomposites and is more prominent when their percentages in the polymeric matrix increase. It has some negative effects on the final mechanical and biological properties of samples. This arises due to the interaction between the particles through van der Waal's forces. These are the weak forces and particles are loosely bound together and are more prominent when the percentage of particles is high. The µ-CT results were aligned with the results which were observed in SEM.

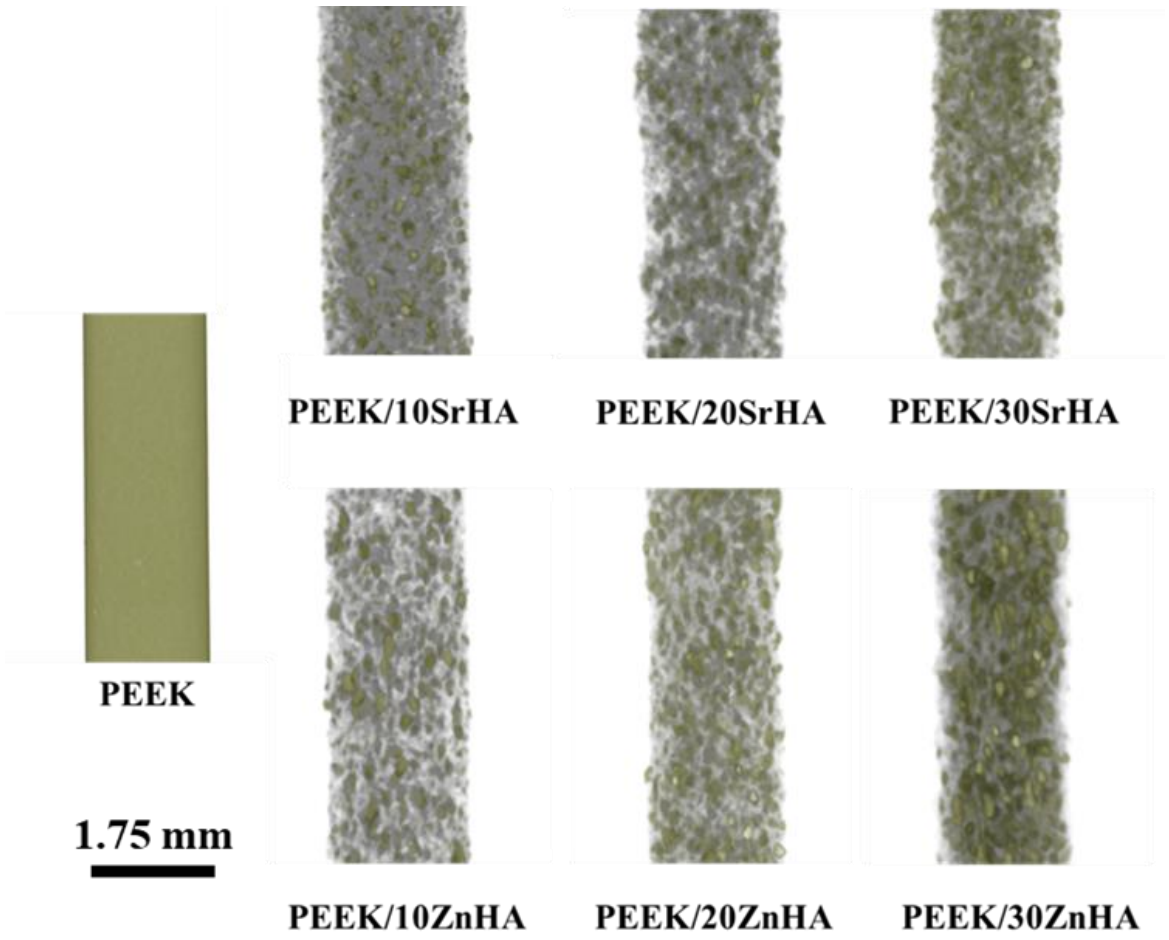

Figure 25 µ-CT of PEEK filament and PEEK/doped-HA filaments produced via extrusion, showing a uniform distribution of bioceramic particles, tiny grey dots represent bioceramic particles

5.7 Thermal analysis

5.7.1 Thermogravimetric analysis

The thermal degradation study is important because in this study the PEEK polymer and its nanocomposites have undergone heating and melting twice, once during extrusion and secondly during 3D printing. TGA curves have shown in Figure 26. TGA analysis confirms the expected composition of bioceramic in PEEK (0 to 30 wt.%) as well as the degradation temperature of nanocomposites. Leftover bioceramic particles, remaining after oxidative decomposition of organic fraction (PEEK) corresponds very close to the amount of bioceramic particles mixed with PEEK in the preparation of the samples. The changes in the weight of nanocomposites correspond to a function of temperature given in the form of TGA curves. It can be seen the weights of nanocomposites remain constant or very slight change when heated upto 500 °C. PEEK is a hygroscopic material and absorbs a fair amount of moisture at room temperature which plays a negative role in extrusion and 3D printing processes by creating voids. Hence, complete drying is necessary, so the nanocomposite filaments were completely dried prior to the TGA analysis. It can be seen in the graphs that there was not any noticeable weight change detected in the range of 80 to 120 °C which also confirms the effectiveness of the drying method adopted in this study. As the bioceramic particles were thermally stable, so the weight loss measured in composite samples was due to the degradation of polymer matrix [275, 276]. After 545 °C, the degradation started and a sharp decrease in weight was observed and a total weight loss of almost 50 % occurred at 620 °C for pure PEEK, 640 °C for PEEK/10HA, 650 °C for PEEK/10SrHA and 660 °C for PEEK/10ZnHA. This behavior also indicates that the thermal stability of PEEK is enhanced in the presence of hydroxyapatite particles [299]. The abrupt weight decrease is indicative of decomposition of PEEK as reported by Hay and Kemmish [300] who found that degradation occurred by random chain scission process at the ether and/or carbonyl linkages in the oxy-1,4-phenylene-oxy-1, 4-phenylene-carbonyl-1, 4 phenylene repeat unit of the polymer chain and by the transfer reaction that can occur. This results in the formation of volatile decomposition products including furan consisting of oligomers, phenol and dibenzofuran. Additionally, carbon dioxide (CO_2) and carbon monoxide (CO) have also been identified as evolving rapidly over this temperature range [301, 302]. Meenan et al. [303] reported that the complete degradation of PEEK polymer occurred without leaving behind any solid residue at 800 °C under an oxidative

environment. The same phenomenon has been observed in this study as 100 % weight loss was detected for pure PEEK. However, weight remained was detected for nanocomposite materials which were due to the presence of bioceramic particles such as HA, SrHA and ZnHA because they do not degrade up to 800 °C. The TGA has shown that the physical blending has indeed produced blends with the correct weight percentages.

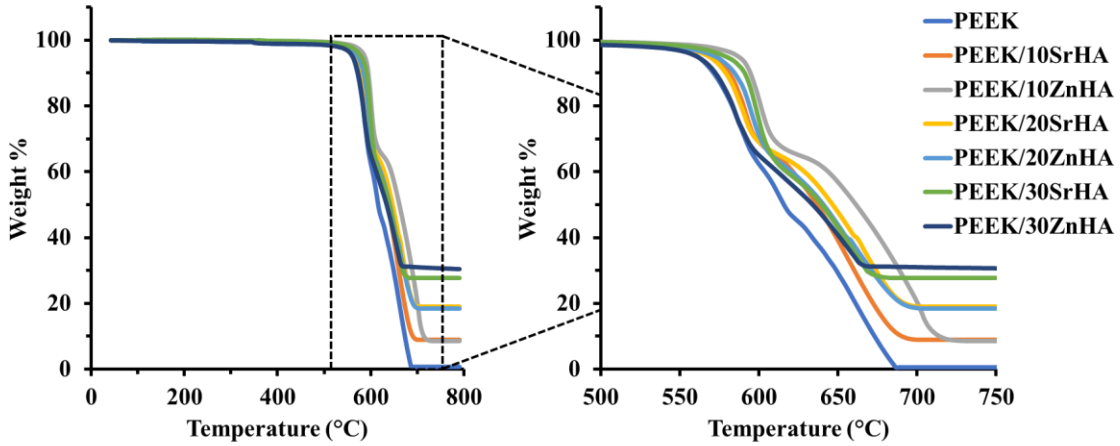

Figure 26 Thermal analysis of PEEK and its composites; The effect of temperature on weight loss studied via TGA, A) TGA curves of PEEK and its composite filaments, B) The enlarged region showing the detailed weight loss of the samples.

5.7.2 Differential scanning calorimetry

The study of thermal properties is important because the polymer and its composites have to undergo melting during the filament extrusion process and then 3D printing. Figures 27 (a) and (b) show the melting temperatures (T_m) and crystallization temperatures (T_c) of the PEEK nanocomposite filaments, respectively. It was observed that the melting point increases and the crystallization temperature reduces as the loading level of bioceramic particles increases, which can be ascribed to the nucleating effect of doped-HA particles leading to increased crystallization [304, 305]. The melting point of PEEK increases from 343.3 °C to 348.3 °C, 351.5 °C, 356.7 °C for PEEK/SrHA and 347.5 °C, 350.1 °C, 355 °C for PEEK/ZnHA containing 0, 10, 20 and 30 wt.% filler particles, respectively. In addition to their nucleating effect, presence of the bioceramic phase in the PEEK matrix hinders polymer chain mobility and increases melt viscosity [306]. This resulted in the need to optimize the extrusion and 3D printing parameters for the doped HA loaded samples.

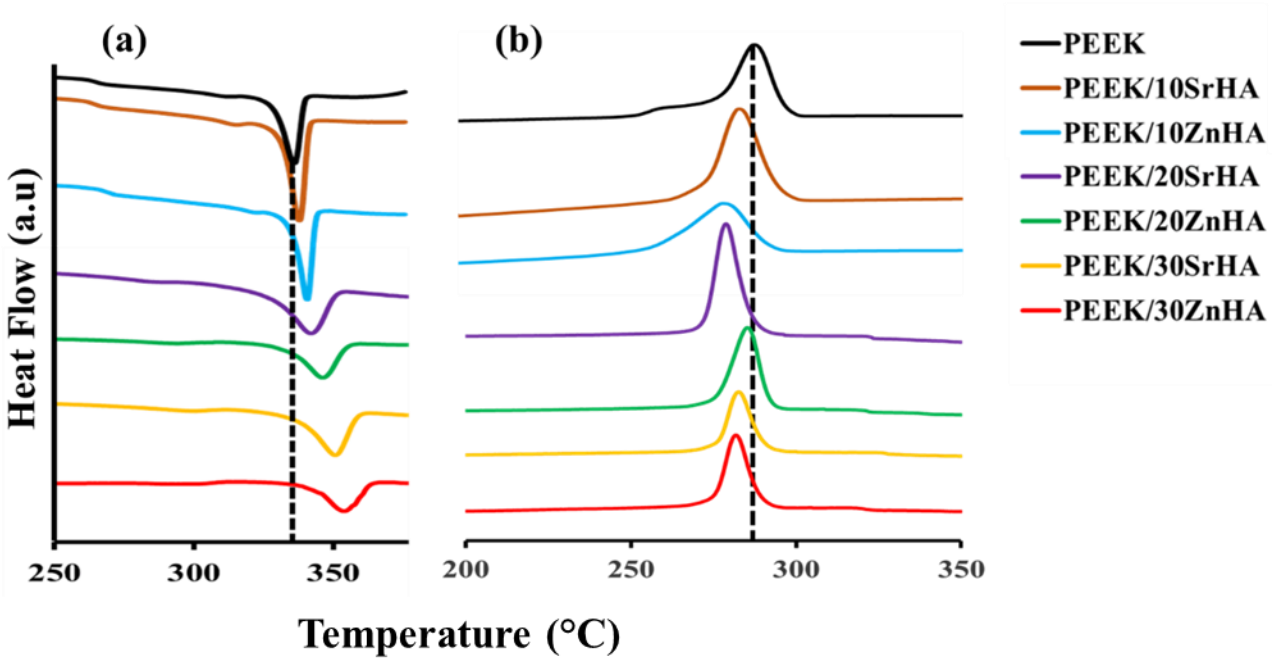

Figure 27 Thermal properties of filaments, (a) represents the Tm and (b) represents the Tc of PEEK, 10SrHA, 10ZnHA, 20SrHA, 20ZnHA, 30SrHA, 30ZnHA

Figure 27 (b) shows the crystallization behavior of PEEK and its nanocomposite filaments during the cooling cycle. It has been reported in previous studies that the crystallization behavior in polymer composites can be affected by two main factors i.e., heterogenous nucleation and mobility of polymer chain portions. The combination of both these phenomena be responsible for a broad range of crystallinity in the PEEK composites [306]. If heterogenous nucleation dominates in the crystallization process, then T_{pc} (peak crystallization temperature) will shift to higher temperatures. On the other hand, if the polymer chain mobility is a dominant factor, then T_{pc} will decrease with the addition of ceramic particles. Figure 27 (b) shows the peak crystallization temperatures of PEEK and its composites. In this study, the crystallization temperature (T_c) is decreased as the weight percent of bioceramic in PEEK is increased which shows that the blocking polymer chain phenomenon is dominant and delayed the start of crystallization process in cooling cycle. For pure PEEK, crystallization starts at approximately 285 °C and it is suppressed in the presence of bioceramic particles. For example, it reduces with bioceramic percentages 10, 20, 30 wt.% to 283.3 °C, 277.5 °C, 275.8 °C for SrHA and 279.4 °C, 278.2 °C, 276.2 °C for ZnHA, respectively. A summary of thermal properties is given in Table 9.

Table 9 Thermal properties of PEEK and its nanocomposite filaments measured by DSC

	T_g, mid-point (°C)	T_m (°C)	T_c (°C)	X_c (%)
PEEK	143.3	343.1	285.8	27.7
PEEK/10SrHA	144.1	348.3	283.3	28.1
PEEK/10ZnHA	143.2	347.5	279.4	28.7
PEEK/20SrHA	146.7	351.5	277.5	30.5
PEEK/20ZnHA	144.4	350.1	282.2	31.5
PEEK/30SrHA	148.1	356.7	276.8	32.3
PEEK/30ZnHA	145.3	355.0	277.2	34.6

5.8 Discussion

In this chapter, the filaments of PEEK and its composites were optimized and characterized for physico-chemical and thermal properties such as SEM, EDX, µ-CT, FTIR, TGA, DSC. The first and foremost optimizing parameter during filament extrusion was the extrusion temperature. The extrusion temperature was adjusted after knowing the melting temperature of PEEK powder via DSC analysis. By keeping all other parameters constant, the temperature was increased gradually until a uniform molten material started to come out from the nozzle. After obtaining uniform molten material, other parameters (extrusion speed, cooling rate, puller wheel speed) were adjusted and their effect on the filament diameter was monitored carefully and tuned accordingly until uniform diameter was achieved. Similarly, the procedure of optimizing was repeated for other types of compositions and get their filaments with consistent diameter. The obtained filaments were characterized by various techniques. For example, the presence of surface defects was analyzed via SEM and internal structure of filaments were observed via µ-CT. Additionally, the homogeneity of filler particles was investigated because the non-uniform distribution of the bioceramic particles is detrimental to the mechanical properties and improper handling of raw materials causes the inclusion of impurities which can affect the biological performance of the final parts. Furthermore, uniform diameter of filaments ensures the constant mass flow rate during 3D printing. However, thin diameter filament lack of polymer mass and creates defects such as

cavities. On the other hand, thicker diameter results in the excessive mass and hence alter the geometry of the 3D printed parts [298]. The filaments in this study are prepared by using a desktop extruder which has an optical diameter sensor and the dynamic puller system which work together to achieve a precise diameter. In order to ensure the accuracy, the diameter was also measured manually with Vernier Calipers after every 2-3 meters of extrusion. SEM analysis of the filaments showed the surface morphology and presence of bioceramic particles. The surface of pure PEEK filaments was smoother than its composites. It was observed that the roughness of the surface was increased as the weight percentage of bioceramic particles was increased. The filaments contained 10 wt.% SrHA and ZnHA showed a good dispersion of particles with no detectable voids or pores present on their surfaces. However, the surface of the filaments contained 20 wt.% SrHA and ZnHA were rougher than former, however, still there were not any surface defects were observed and the images showed a good dispersion of particles without any significant agglomeration. Additionally, even more rough surfaces were observed when the weight percentage of the bioceramic particles were increased to 30 % and the particle were joined in the form of cluster. The agglomeration of nanoparticles is a common phenomenon due to having high surface free energies. In order to decrease their surface free energies, the nanoparticles decrease their surface areas by physically adhering to other nanoparticles and thus form agglomerates [307, 308]. The adhesion of these particles is due to a weak force to form micro-sized particles which can be easily separated. However, when mixing is done with their higher percentages, these particles adhere again and form micro sized agglomerates. These agglomerates can affect the properties of final parts.

EDX detect the elemental composition qualitatively and quantitatively as well as the distribution of the bioceramic particles. Pure PEEK filament sample showed only carbon (C) and oxygen (O) which were expected due to the organic nature of PEEK polymer. Ca, P and O were detected in all the composite samples along with Sr in SrHA samples and Zn in ZnHA samples. The mapping scan confirmed that the elements were uniformly distributed on the surface of 10 and 20 wt.% samples. However, agglomeration was detected in the samples contained 30 wt.% samples. The results of particle distribution were matched with what observed in SEM images. The internal structures of the filaments were analyzed by μ-CT. Pure PEEK filaments showed a smooth structure with negligible porosity. As porosity is detrimental to the mechanical properties which usually came by selecting inappropriate processing temperatures and other extrusion

parameters. Additionally, porosity comes with the incomplete drying of raw powders before processing. PEEK is highly susceptible to moisture adsorption and this susceptibility increased in powder form due to the high surface area of the powders [309]. The absence of porosity and voids confirm that the quality of filament is good, and the optimization parameters are correctly selected. The distribution of the particles was uniform in the samples contained 10 and 20 wt.% bioceramic particles. The number of particles in 20 wt.% samples were more as compared to in 10 wt.%. It was confirmed through μ-CT that the bioceramic particles were distributed in the internal structure of filaments uniformly as detected with SEM on the surfaces of filaments. However, 30 wt.% contained some agglomeration due to the highest weight percent and combining of the particles due to weak Van der Waal forces. PEEK polymer has high melting point, so it requires high processing temperatures and high thermal coefficient of expansion which results in a shrinkage during cooling. Additionally, in the presence of particles in its composites, the viscosity become high. Due to these, processing of PEEK is quite challenging so the understanding of the complete thermal profile of the PEEK and its composites is important [310]. TGA confirmed the thermal decomposition of all the materials. The by-products after the decomposition were only due to the decomposition of PEEK because bioceramic particles remained stable up to 800 °C. The thermal degradation of the PEEK polymer started after 545 °C so it was concluded that the processing of PEEK is safe below 545 °C. Jonas and Legras [311] reported that the thermal degradation of polymers can also take place at lower temperatures by increasing the holding time and decrease the peak temperature of crystallization. The degradation process consists of homolytic random chain scission, producing radicals that can attack the neighboring polymer chains to form branches and finally crosslinks. Moreover, the presence of bioceramic particles in the PEEK matrix delayed the degradation start temperature and hence increased its thermal stability. T_d for 10, 20, 30 wt.% of SrHA and ZnHA were around 550, 556, 561 °C, respectively. This suggested that the T_d had not affected the type of bioceramic particles (either SrHA or ZnHA), however, only depended upon their weight percentage. The main by-products for the PEEK and its composites were CO and CO_2 due to the organic nature of PEEK [125]. These were gases and left no mass of polymer which was evident from the end-mass that was nearly similar to the weight percent of bioceramic particles i.e., 10, 20 and 30 wt.%.

Moreover, these filaments were used as a feedstock for optimizing the 3D printing parameters to obtain a good print quality and acceptable mechanical properties samples. In the

following chapter, the characterization of 3D printing samples has been discussed in detail by analyzing the distribution of bioceramic particles after 3D printing via SEM, EDX and µ-CT, mechanical properties such as tensile strength and impact strength, bioactivity of the samples in SBF solution, the effect of SBF on the mechanical properties and effect of PEG_{1000}-DOPA coating on surface hydrophilicity. These characterizations were performed to test the material's ability to be used for manufacturing orthopedic implants particularly craniofacial bone implants.

6 Chapter 6: Characterization of 3D-printed PEEK and its composites

6.1 Introduction

PEEK being a semicrystalline polymer has high shrinkage values during cooling, due to this property, its processing via FDM is challenging. The level of difficulty further increases when a filler material is incorporated into it to make its composite which increases its viscosity. One of the aims of this study is to investigate the processibility of PEEK composites in FDM 3D printing by optimizing various 3D printing parameter, most importantly printhead temperature, built-plate temperature and chamber temperature to overcome shrinkage. Furthermore, layer thickness, printing speed and infill pattern are analyzed to obtain optimum mechanical properties which could be used for craniofacial implants. In this chapter, it is hypothesized that the 3D printed bioactive samples of PEEK composites could be produced via FFF technology. The effect of filler content on the 3D printing processing parameters are examined. Furthermore, bioinert nature of PEEK does not allow biological molecules to attach on its surface due to its hydrophobic nature. The filler particles have high wettability, so their incorporation can enhance the wettability of the composite. Additionally, coating of composite samples with biocompatible and hydrophilic material would enhance its wettability. The samples are characterized for their physico-chemical properties, mechanical strength and bioactivity. It is assumed that the technology does not alter the chemical properties of the composite samples, the printed samples have adequate mechanical strength so that it can be used for non-load bearing craniofacial medical implants, samples demonstrate bioactivity in SBF solution and coating with PEG_{1000}-DOPA enhances the hydrophilicity of the samples.

6.2 Characterization of 3D printed samples

The 3D printed samples were characterized by various scientific techniques such as XRD, µ-CT, SEM, EDX, FTIR, hydrophilicity, mechanical and biological testing. These techniques helped to detect the physical and chemical changes, compare the mechanical properties of 3D printed parts with the literature and human bone and analyze the bioactivity in SBF solution after 7, 14, 28 days of immersion. Also, on the basis of the results obtained, it would be concluded either FFF technology is suitable for producing patient-specific bioactive 3D printed medical implants or not.

6.2.1 X-ray Diffraction

The crystalline phases and related characteristic peaks of PEEK, SrHA and ZnHA powders, as well as of the PEEK nanocomposite 3D printed samples were observed by X-ray diffraction. The XRD results for the 3D printed PEEK/doped HA samples are illustrated in Figure 28. The characteristic peaks of SrHA and ZnHA confirm the presence of bioceramic particles in the PEEK nanocomposites. The major diffraction peaks of PEEK were detected at approximately 19.1°, 21.3°, 22.8° and 28.1° with crystal planes (110), (111), (200), (211) respectively, while the major peaks of HA were detected at approximately 25.7°, 31.6°, 32.8° and 34.1° having crystal planes of HA as (002), (211), (112), (300), (202) in accordance to International Centre for Diffraction Data (ICDD) File number 09-0432 [283, 312, 313], with slight variations due to the presence of Sr and Zn doping elements [283, 314]. In the PEEK nanocomposite samples, the intensities of SrHA and ZnHA peaks gradually increase while the intensities of peaks representing PEEK gradually decrease as the bioceramic content increases from 10 to 30 wt.% [238].

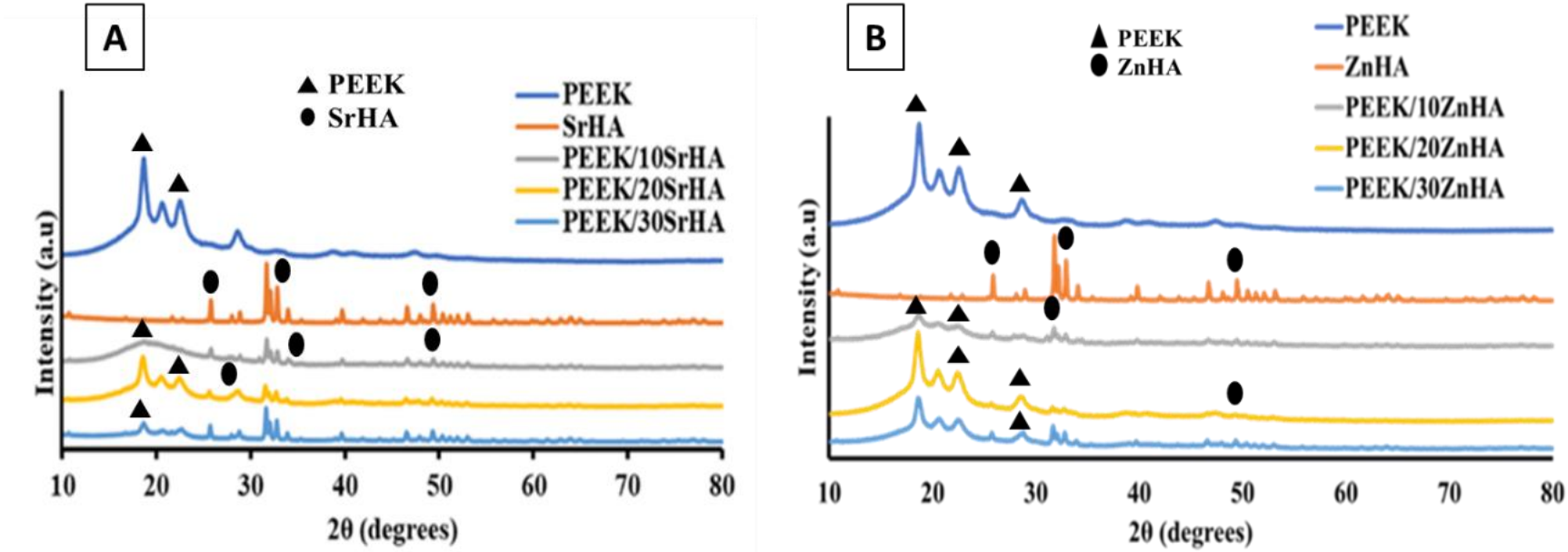

Figure 28 XRD analysis of PEEK and its nanocomposites with A) SrHA and B) ZnHA, produced via 3D printing

6.2.2 Scanning Electron Microscopy

The top surface morphology of the 3D printed samples was evaluated via SEM as shown in Figure 29. The doped HA particles on the surface can act as bioactive sites for apatite formation and for other biological integration activities [12, 13, 315]. Moreover, the addition of HA renders the PEEK surface more hydrophilic, which could help cells to attach to the surface of an implant and hence promote bone growth [228, 316]. The SEM images of pure PEEK sample showed absence of particles while the top surfaces of composite samples showed a uniform distribution and good dispersion of 10 and 20 wt.% bioceramic particles in the 3D printed PEEK samples. However, the agglomeration was detected on the surfaces of samples contained 30 wt.% of bioceramic particles. The agglomeration in nanoparticles is a common phenomenon because they have a high surface activation energy, and lowered them by combining with other nearby particles, thus form agglomerates. They are joined by a weak Van der Waal's force and can easily breakable [317]. However, if the concentration of the particles is high then it is difficult to keep these particles apart. They join with other particles as they come in contact during mixing, extrusion or 3D printing when their concentration is high. In this study, it was observed that the percolation threshold of these particles in PEEK matrix is between 20 % to 30 %. Additionally, the SEM images of the top surfaces of 3D printed samples showed that the surfaces were free from significant surface defects such as gaps which appeared due to the incomplete fusion of the layers.

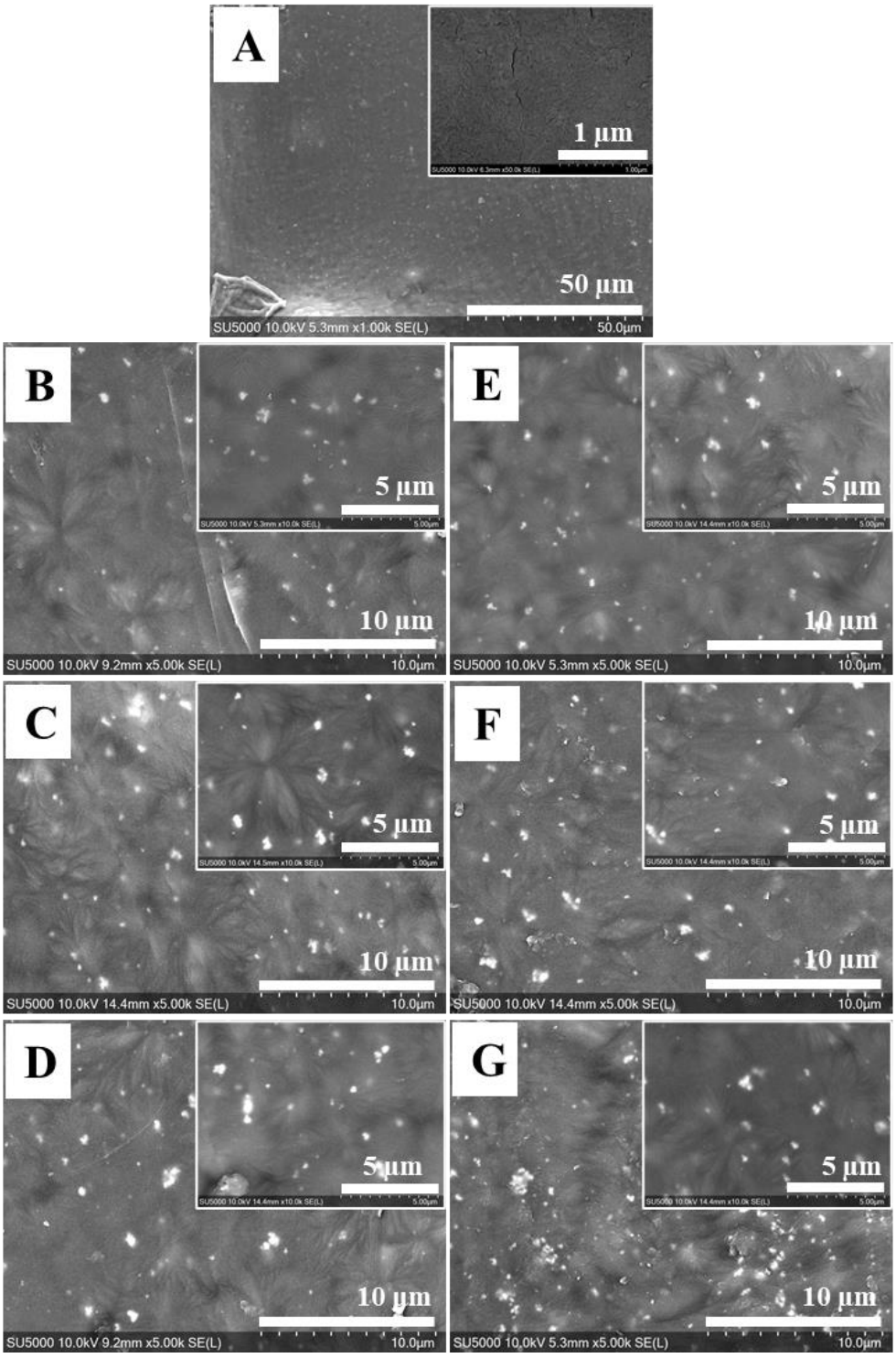

Figure 29 SEM images of top view of 3D printed samples showing the distribution of bioceramic particles tiny white-dots represent the bioceramic particles, A) PEEK, B) PEEK/10SrHA, C) PEEK/20SrHA, D) PEEK/30SrHA, E) PEEK/10ZnHA, F) PEEK/20ZnHA, G) PEEK/30ZnHA

6.2.3 Energy Dispersive X-ray Spectroscopy

The presence of bioceramic particles and their distribution on the surfaces of 3D printed samples were analyzed by EDX as shown in Figure 30. Different types of scans were performed on the samples to confirm the results such as point scan, area scan and mapping. The point, area and mapping scans of pure PEEK sample were detected the presence of C and O, as expected due to the organic nature of the PEEK polymer. This confirmed that no additional unwanted elemental impurity was included during the 3D printing of the samples. EDX also detected the elements corresponded to SrHA, ZnHA and PEEK in the composites. The peak intensities of the elements in doped HA increased while PEEK decreased as the weight percent was increased from 10 to 30 wt.% measured by area and point scans. There was not any additional unwanted elemental impurity detected after the 3D printing of the samples. The distribution of the bioceramic particles were observed by mapping scan. It was observed that the distribution of the particles was uniform in 10 and 20 wt.% samples. However, agglomeration detected in the samples contained 30 wt.% samples. These results were aligned with the SEM images.

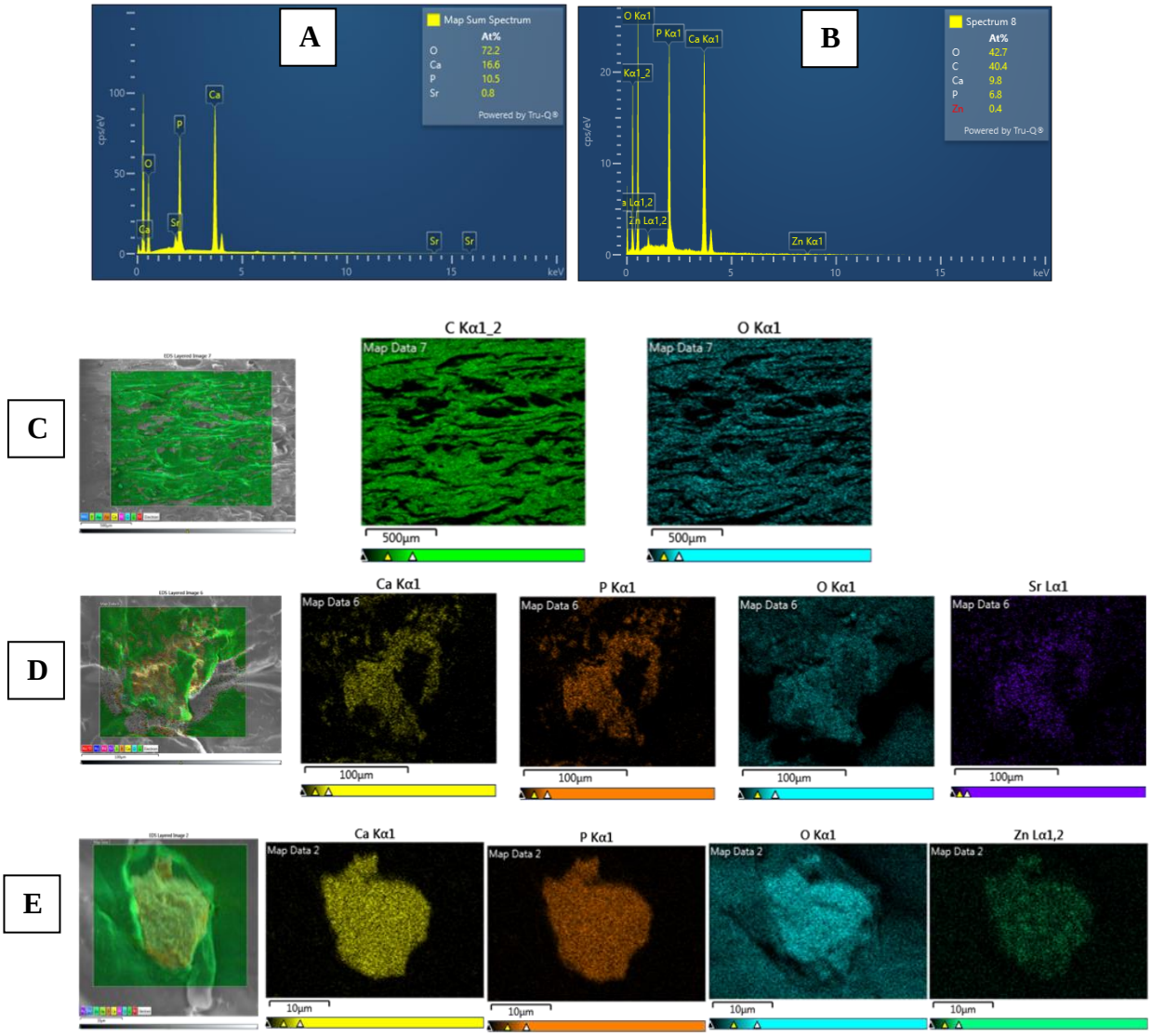

Figure 30 EDX analysis of 3D printed samples A) PEEK/30SrHA, B) PEEK/30ZnHA, C) PEEK mapping, D) PEEK/30SrHA mapping, E) PEEK/30ZnHA mapping

6.2.4 Micro-Computed Tomography

The internal structure and distribution of the bioceramic particles were observed via µ-CT. The images of the samples have shown in Figure 31. It was observed that the 3D printed sample of pure PEEK did not contain any particles, as estimated. Additionally, there was not any significant internal defects were observed. Moreover, the presence and distribution of the bioceramic particles were observed in PEEK composite samples. The presence of bioceramic particles was increased as the weight percent was increased, as expected. Internally, there were not

significant internal defects were detected and the distribution of the particles were uniform. Additionally, the particles were uniformly distributed in the PEEK composites contained 10 and 20 wt.% bioceramic particles, however agglomeration of the particles were detected in the samples contained 30 wt.% of bioceramic particles. The results were aligned with the results which were obtained after SEM and EDX analyses. Moreover, the distribution of the particles was not altered significantly as was detected in the composite filaments.

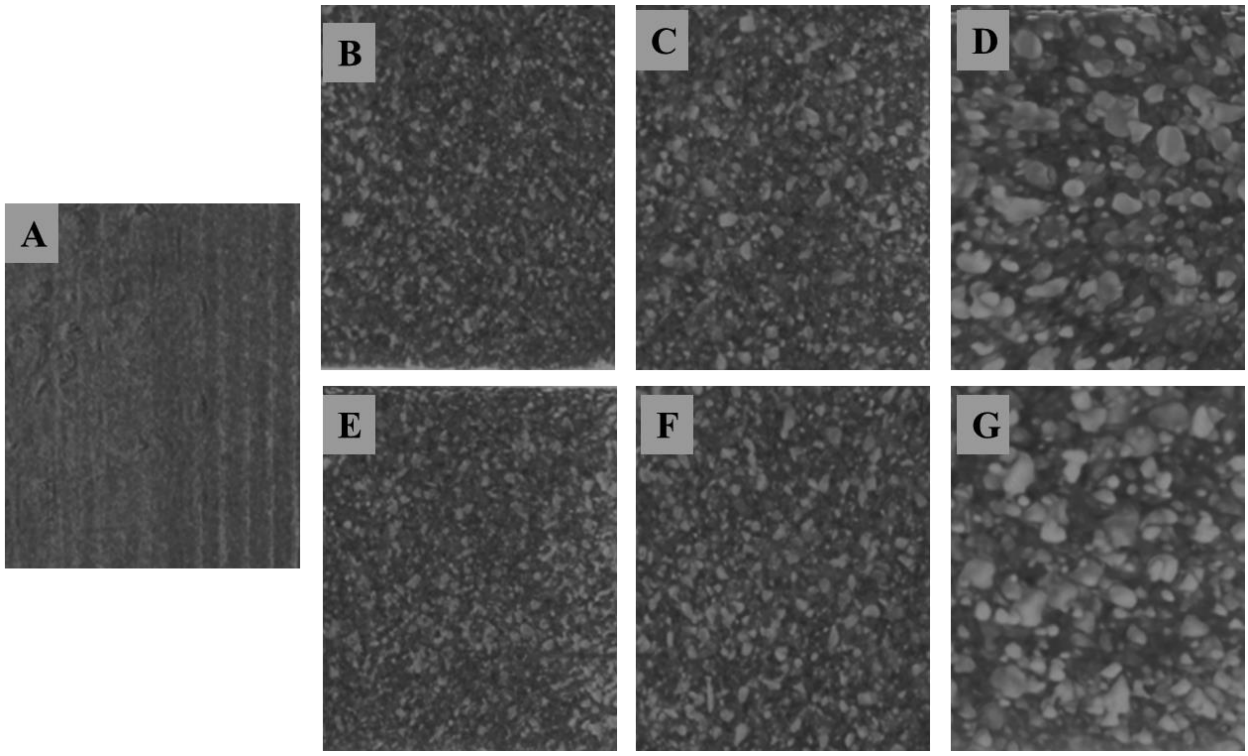

Figure 31 μ-CT analysis of 3D printed samples (A) PEEK, (B) PEEK/10SrHA (C) PEEK/20SrHA, (D) PEEK/30SrHA, (E) PEEK/10ZnHA, (F) PEEK/20ZnHA, (G) PEEK/30ZnHA

6.2.5 Water Contact Angle

The hydrophilicity of sample's surfaces was measured by water contact angle measurements. The measurements were taken from the samples without coating and after coating of PEG_{1000}-DOPA. The explanation of both kind of samples are given below:

6.2.5.1 Uncoated samples

Osseointegration on the surface of a material can be predicted by its wettability [318]. Together with surface porosity, surface roughness and presence of functional groups, hydrophilicity plays a key role in the interaction with biological molecules. A hydrophilic surface is favorable for basic cell interaction mechanism such as cell attachment and proliferation [304]. The surface of the pure PEEK polymer is hydrophobic and hence not directly favorable for cell attachment. The hydrophilicity of the PEEK surface is improved in the presence of bioceramic particles, particularly with an increase in the weight percent of bioceramic particles. The contact angle reported in literature for pure PEEK is between 70° and 90° [46, 47]. As shown in Figure 32, the contact angle for pure PEEK was measured at 85.0° ± 2.2°. The angle slightly decreased to 73.6° ± 2.8° for PEEK/10SrHA and 77.7° ± 3.5° for PEEK/10ZnHA. A further decrease in contact angle was detected with 20 wt.% bioceramic particles. The lowest values were observed for PEEK/30SrHA and PEEK/30ZnHA which were 54.9° ± 3.4° and 56.3° ± 2.4°, respectively. Hence, the presence of bioceramic particles increased the hydrophilicity of the surface, which is likely to result in improved osteointegration [319, 320].

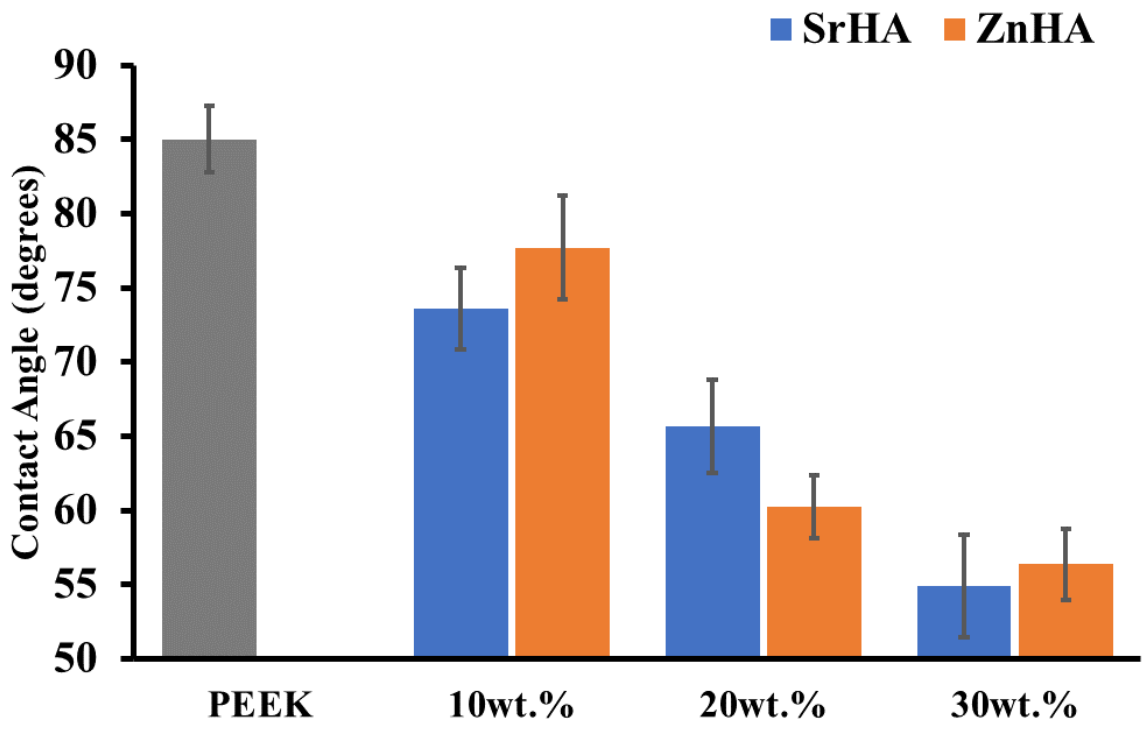

Figure 32 Water contact angle on the 3D printed surfaces of PEEK and its nanocomposites

6.2.5.2 Coated samples

The water contact angle of the PEEK control and 20 wt.% samples after coating with PEG_{1000}-DOPA is reported in Figure 33. The coating on the PEEK and PEEK/20SrHA samples significantly improved their surface hydrophilicity. However, only a small change in contact angle was measured for the PEEK/20ZnHA sample. That could be due to the nature of ZnHA which may have hindered the PEG_{1000}-DOPA coating on its surface. However, further characterization is needed to fully investigate the effect of coating on other properties. The improvement of hydrophilicity of the samples after PEG_{1000}-DOPA coating can be beneficial for increasing the biocompatibility of craniomaxillofacial implants.

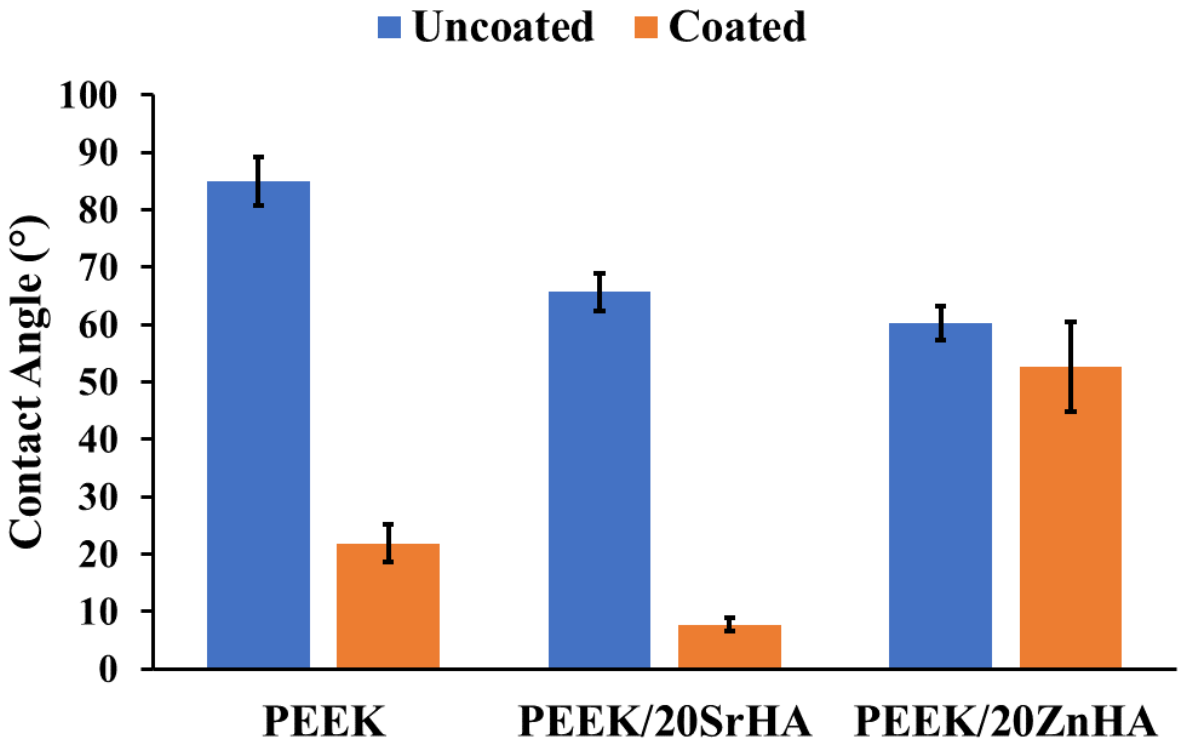

Figure 33 Water contact angle measurement after coating of PEG_{1000}-DOPA on PEEK, PEEK20SrHA and PEEK/20ZnHA samples

6.2.6 Bioactivity testing

The bioactivity of the samples was assessed using a simulated body fluid (SBF) immersion test. The SBF immersed samples were characterized for apatite layer formation by SEM, XRD and FTIR. SEM confirmed the characteristic morphology of apatite while XRD showed the apatite phase formation and FTIR showed the presence of functional groups. Figure 34 shows SEM images of the sample surfaces after immersion in SBF for 0, 7, 14 and 28 days. The SBF is a super-saturated solution with ion concentrations and pH approximately equal to human blood plasma [269] and it can be precipitated out on the surface by variations in number of factors such as pH, temperature and Ca^{+2} ions concentration [321] , thus, in order to avoid the precipitation and establishment of dynamic equilibrium, SBF solution was replaced with fresh solution after every 48 h. There was no apatite formation observed on the surface of pure PEEK even after 28 days, which confirmed its bioinert behaviour [10]. However, apatite formation started after only 7 days of immersion on the surfaces of PEEK nanocomposites. The degree of apatite formation depends on the amount of bioceramic loading and the immersion time. The lowest apatite formation was observed for PEEK/10SrHA and PEEK/10ZnHA nanocomposites after 7 days of immersion, while the maximum apatite layer was observed for PEEK/30SrHA and PEEK/30ZnHA nanocomposites after 28 days of immersion. It is proposed that the bioceramic particles on the surface of PEEK act as bioactive sites, and higher amounts of calcium and phosphate ions are captured by these bioactive sites from the SBF solution at higher HA loadings [12]. Moreover, longer immersion time allows higher amounts of calcium and phosphate ions to deposit on the surface. In comparison to our previous study of the bioactivity of PEEK/HA, both Sr and Zn doped HA show enhanced apatite formation in respect to pure HA [322]. Hence, incorporation of Zn and Sr doped HA is more effective for developing bioactive PEEK/HA cranial implants [312].

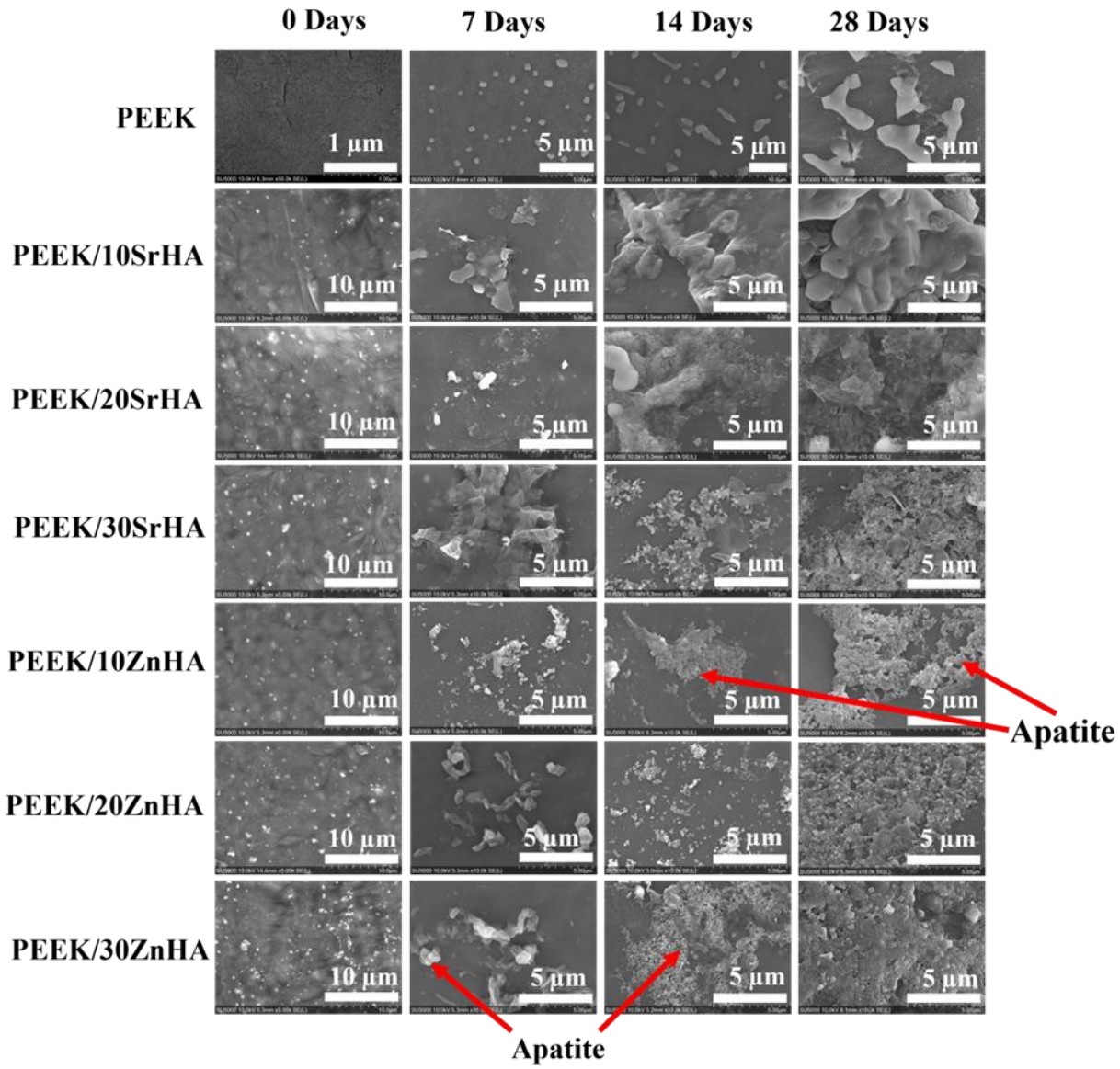

Figure 34 SEM images showing the apatite layer formation on the samples of PEEK and its nanocomposites after immersion in SBF for 0, 7, 14, and 28 days.

The XRD analysis of the SBF immersed samples were performed to detect any chemical change on the surface. Figure 35 shows the XRD analysis which was performed on PEEK/SrHA (Figure 35a) and PEEK/ZnHA (Figure 35b) after immersion in SBF for 7, 14, and 28 days. It can be seen that after immersion in SBF, no new phase was formed. The major peaks of PEEK polymer can be seen at 19.1°, 21.3° and 22.8° [296] which remain nearly same within the same composite. However, there was no conclusive evidence was made which confirmed the formation of apatite

layer after SBF immersion via XRD. On the other hand, the peaks of apatite vary with the immersion time. The major peaks of apatite appeared at 31.6°, 32.8° and 49.5° [283, 312, 313], which slightly increased as the immersion time in SBF increased from 7 to 28 days. This confirms that as the immersion time of the samples increases in SBF, the apatite deposition also increases [323]. In Figures 35a and 35b with 10 wt.% of SrHA and ZnHA, respectively, the peaks in the apatite region (shown by dotted lines) slightly increased as the immersion time increased from 7 days to 28 days. However, the peaks of PEEK region remained almost the same. The similar trend can be seen with 20 wt.% and 30 wt.% of SrHA and ZnHA. Hence, these XRD results showed that all composites formed apatite layer on their surfaces in SBF solution which was also confirmed by SEM results.

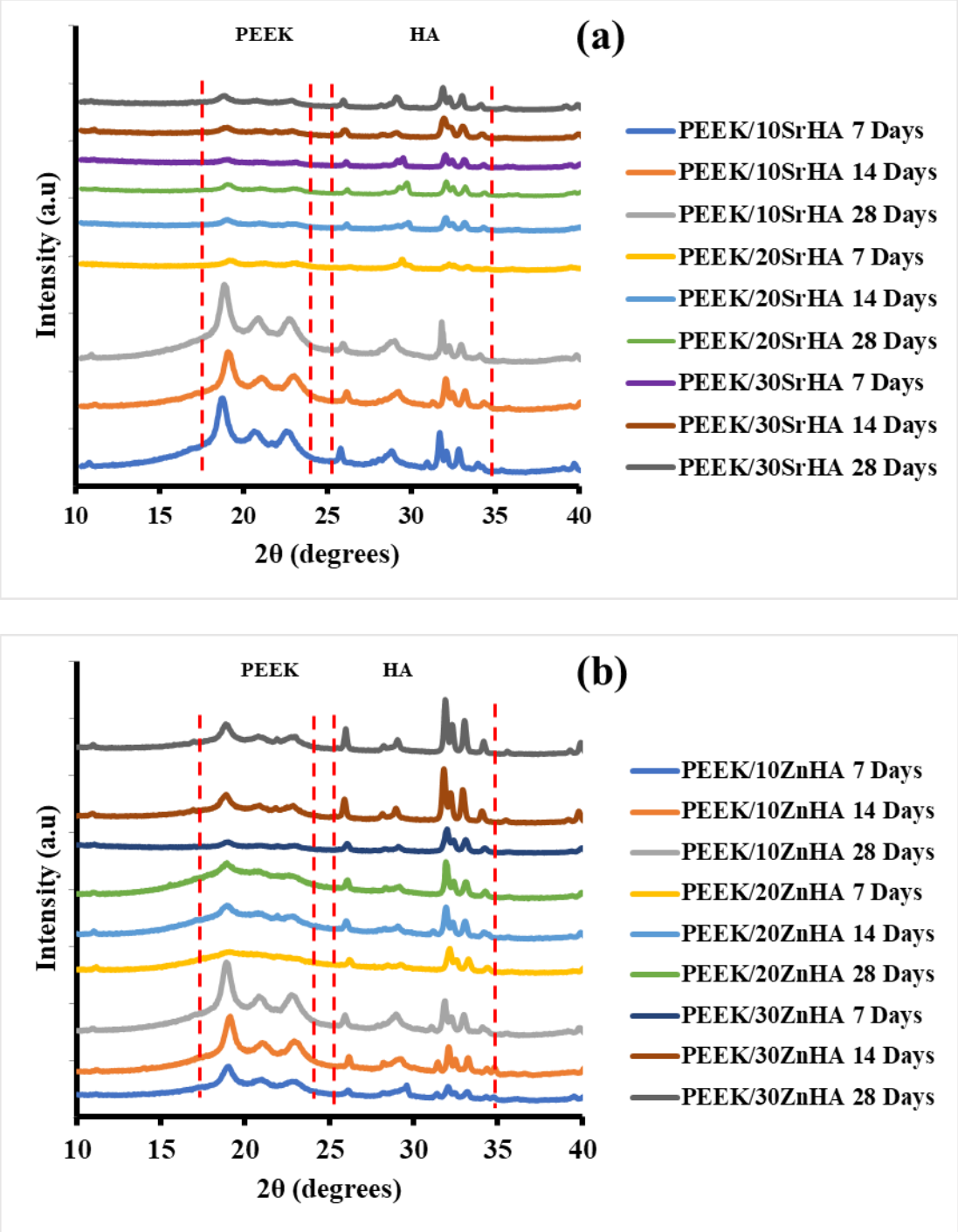

Figure 35 XRD of PEEK composites after immersion in SBF for 7, 14 and 28 days, PEEK with a) Strontium doped hydroxyapatite (SrHA), b) Zinc doped hydroxyapatite (ZnHA)

The formation of apatite on the surfaces of 3D printed PEEK composites has also been observed via FTIR and the spectra have been shown in Figures 36a and 36b. It was observed that the major peaks associated with the stretching vibration of the P-O bond due to the doped-HA appeared at 1200 cm^{-1} and 900 cm^{-1} while carbonyl stretching vibration peak due to PEEK polymer observed at 1655 cm^{-1} (the regions have been marked with dotted lines). The variation in the peak intensity of P-O bond was observed after immersing in SBF for 7, 14 and 28 days [324, 325]. However, no clear proof was produced that proved the formation of an apatite layer following SBF immersion using FTIR. This could be due to the fact that FTIR is not sensitive enough to detect an apatite on the surface of the samples. Additionally, the FTIR knob might be pointed on the surface where there is no apatite present. However, the presence of apatite has been confirmed via SEM, reported in section 6.2.6.

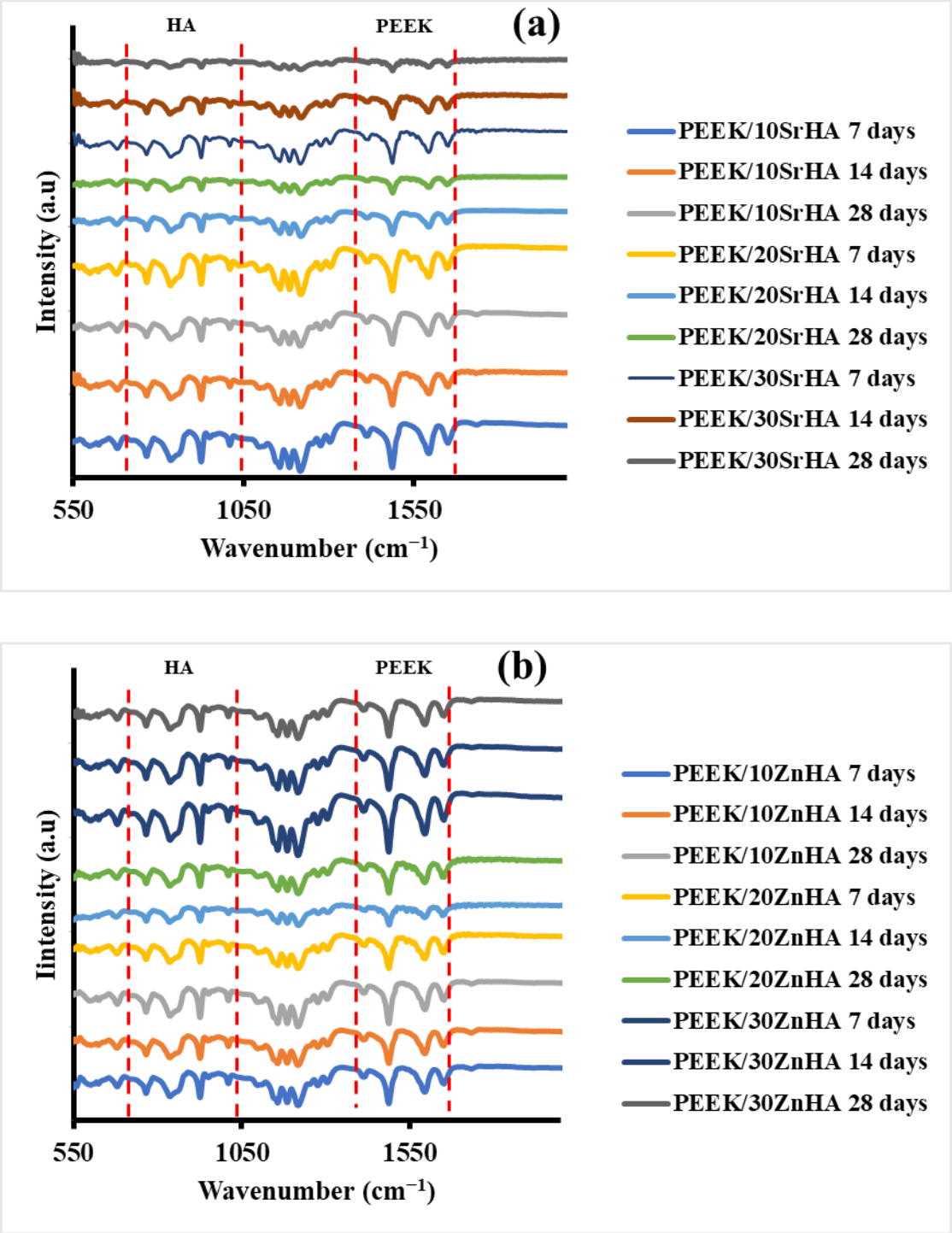

Figure 36 FTIR analysis of the samples s after immersion in SBF for 7, 14 and 28 days

6.2.7 Mechanical performance

The mechanical performance of the 3D printed samples was evaluated by tensile testing and impact testing. The effect of SBF immersion on the tensile properties was also determined.

6.2.7.1 Tensile testing

Tensile strengths of the samples were measured before and after the SBF immersion. The purpose of this study was to investigate the effect of apatite formation on the surface of 3D printed samples and immersion time.

6.2.7.1.1 Before SBF immersion

Results for tensile strength and Young's modulus of PEEK and its nanocomposites, before immersion in SBF, are shown in Figure 37. As seen in Figure 37, the tensile strength decreases while the Young's modulus increases as the amount of bioceramic increases from 0 to 30 wt.% [10, 237, 238]. The reduction in tensile strength with the addition of bioceramic may be due to weak interfacial adhesion and mismatch of stiffness between the particles and the polymer matrix which can induce stresses and weak points within the nanocomposites [310]. When load is applied, the poor interfacial bond can result in premature crack formation and rupture at lower levels of stress [238, 310, 326]. This phenomenon was more prominent at higher loading levels. In this study, the tensile strength of PEEK was measured at 75.1 MPa. In comparison with pure PEEK, the tensile strength decreased approximately by 7.9 %, 25.0 %, 31.5 % with the addition of 10, 20, 30 wt.% of SrHA, respectively. Similarly, the tensile strength decreased approximately by 11.8 %, 19.7 %, 32.3 % with the addition of 10, 20, 30 wt.% ZnHA, respectively. The examples of stress-strain graphs of few samples have been provided in Supplementary Information. On the other hand, the Young's modulus increased with the addition of SrHA and ZnHA to the PEEK matrix. Hence, the changes in the mechanical properties were more dependent on the doped HA content compared to the nature of the doping elements. The tensile strength and Young's modulus of cortical bone is in the range of 50-150 MPa [327] and 2-8 GPa [328], respectively. Hence, the samples produced by 3D printing in this study have adequate strength and modulus suitable for orthopaedic implants. However, the samples containing 10 wt.% and 20 wt.% ZnHA and SrHA can be considered as better options in this respect [10, 237, 238].

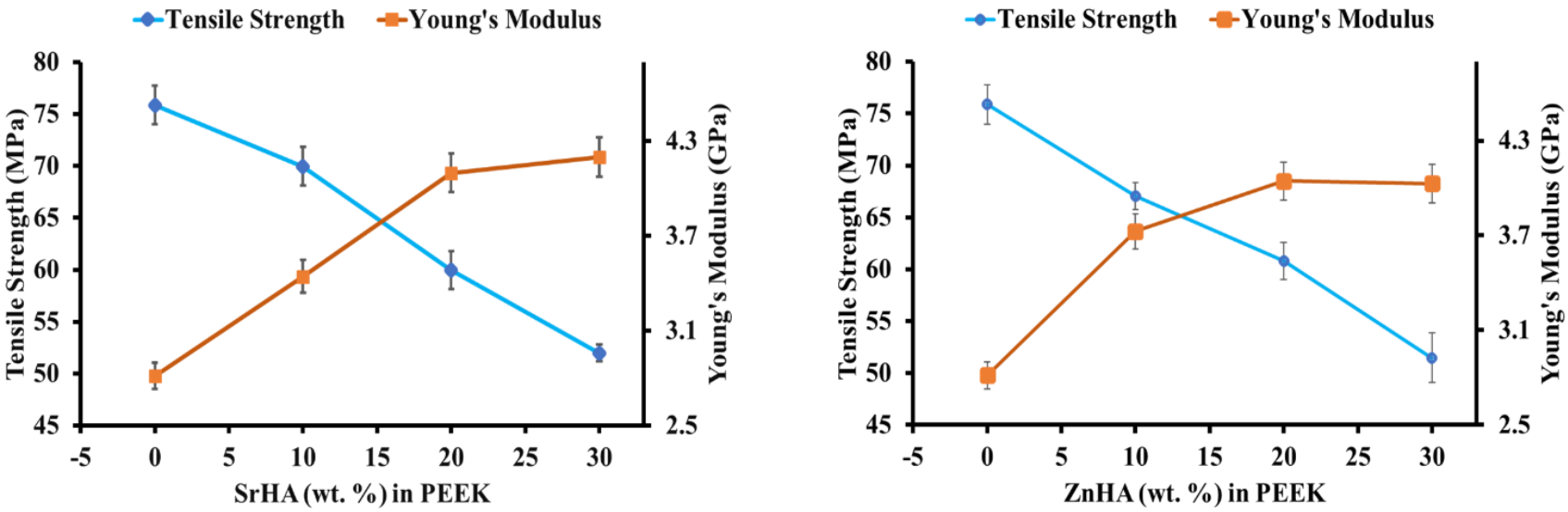

Figure 37 The effect of bioceramic particles on tensile strength and Young's modulus of PEEK and its nanocomposites

6.2.7.1.2 After SBF immersion

The mechanical test results after immersion in SBF are shown in Figure 38. It was observed that there was not any significant change in the tensile strength after 28 days of immersion in the SBF. The slight variation of tensile strengths was observed that could be due to either the inconsistency in 3D printing or crystallinity. It can be observed that the tensile strength decreases slightly after 7 days and 14 days of immersion in SBF by 5.9 % and 8.4 % for SrHA and 4.9 % and 6.7 % for ZnHA, respectively. However, no further decrease in tensile strength is observed after 28 days of immersion in SBF.

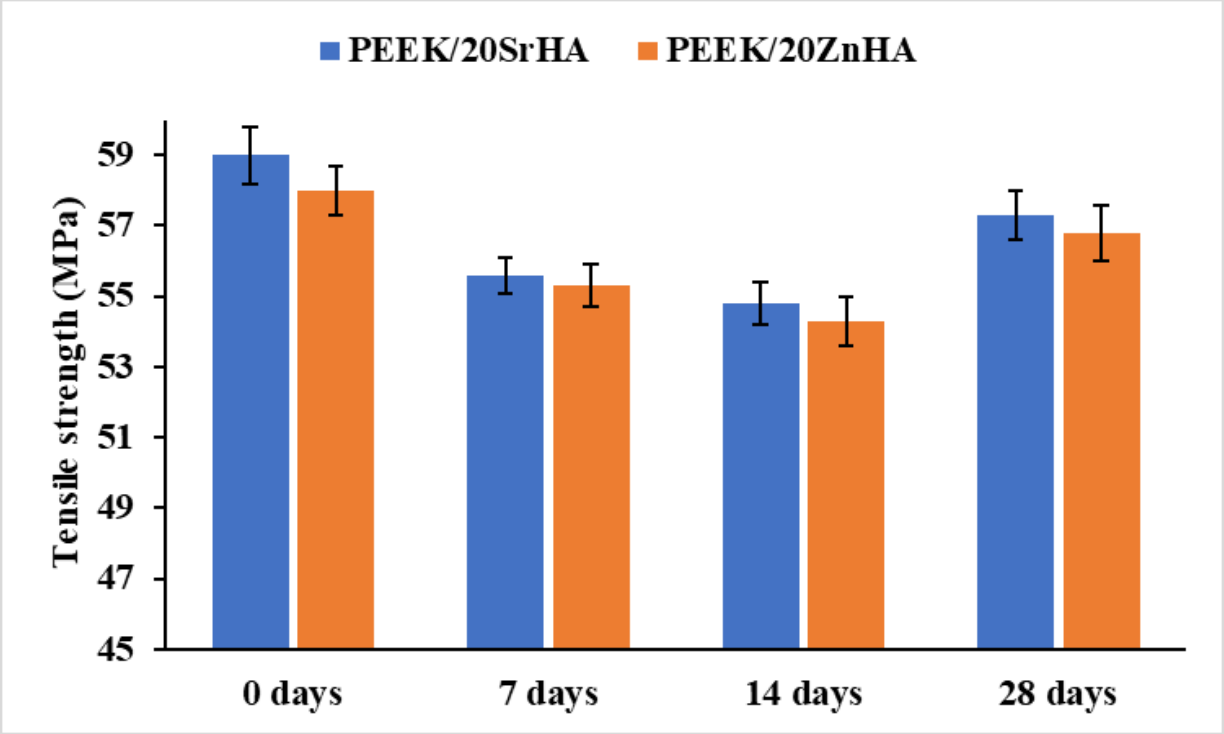

Figure 38 Tensile testing results of samples containing 20 wt.% of bioceramic particles after immersion in SBF for 7, 14, 28 days

6.2.7.2 Impact testing

The impact strength of PEEK and its nanocomposites are shown in Figure 39. The impact strength of PEEK is measured as 14.1 kJ/m^2 and it decreases as the percentage of bioceramic particles increases. This may be an indication of weak bonding between the bioceramic particles and PEEK matrix, resulting in crack initiation and propagation in the region of impact. Hence, samples containing ceramic particles absorbed less energy before break as compared to pure PEEK. This phenomenon was more prominent as the weight percentage of bioceramic was increased. In this study, by incorporating 10, 20 and 30 wt.% bioceramic the impact strength was measured as 11.1 kJ/m^2, 9.0 kJ/m^2, 5.2 kJ/m^2 for SrHA samples and 10.3 kJ/m^2, 8.4 kJ/m^2, 4.0 kJ/m^2 for ZnHA samples, respectively. The amount of energy absorbed by the skull bone is reported as in the range of 3 to 9 kJ/m^2 and depends on the age of patient, type of cranial bone as well as loading rate [59]. In this study, the measured values for PEEK and its nanocomposites fall within that range.

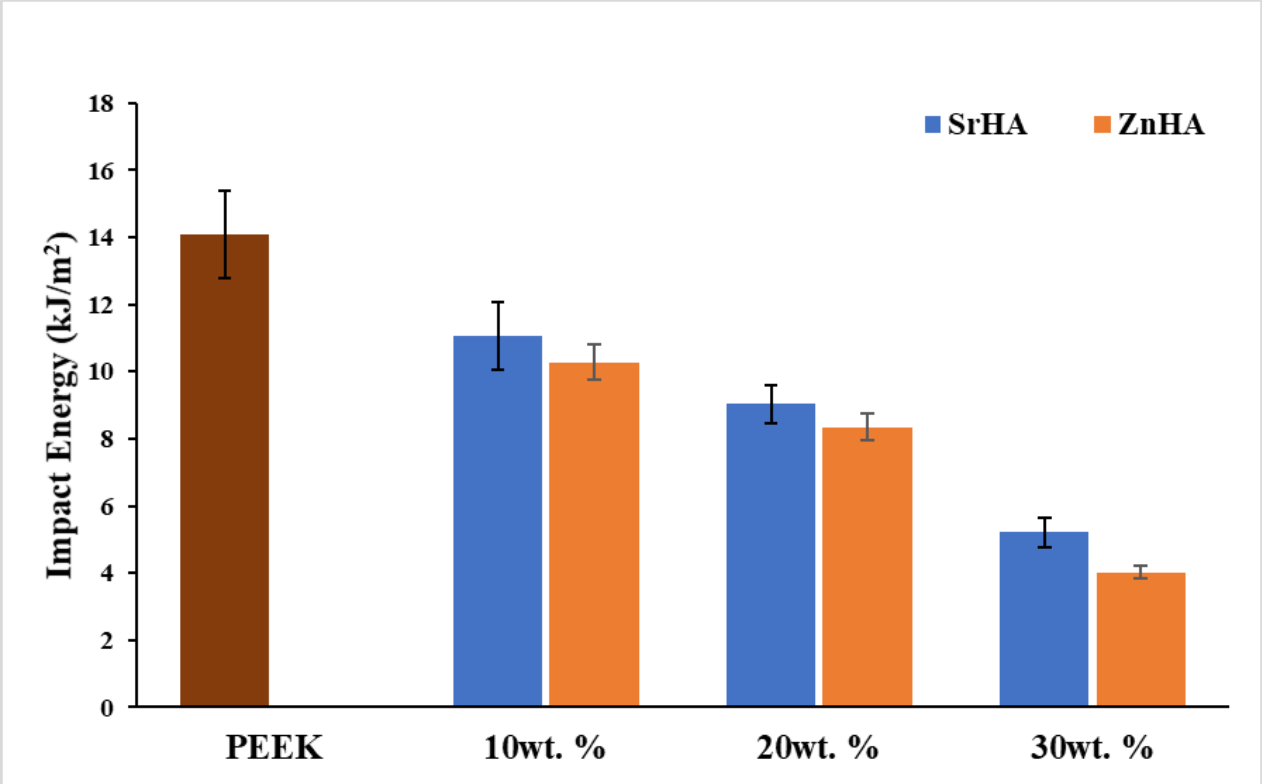

Figure 39 Izod Impact strength of PEEK and its nanocomposites at different weight percentages of bioceramic particles measured from unnotched samples according to ISO 180:2000

6.3 Discussion

In this chapter, the 3D printing of PEEK with doped-HA nanocomposites has been described. The results presented here illustrate that the FFF 3D printing can be used successfully to fabricate PEEK/doped HA composites up to 30 wt.% and addresses the significant gap in the knowledge. In order to consider a material acceptable for orthopedic implant, the material chosen for 3D printing firstly must be printable, have enough structural and mechanical strength intended for particular application and must be biocompatible [7, 329]. The PEEK composites were successfully fabricated using 3D printing technology up to 30 wt.% under the optimized parameters employed here and it is worth to note here that the slight agglomeration was observed in SEM and μCT analysis with 30 wt.% of particles. This could be due to the fact that the PEEK has high viscosity even at high temperature [330].

In this study, the morphology of the top surface of 3D printed samples was observed *via* SEM. The SEM images confirmed the presence of bioceramic particles and their distribution on the polymer top surface. It was observed that the bioceramic particles were uniformly distributed in PEEK contained 10 and 20 wt.% without significant agglomeration and surface did not contain any major surface defects such as pores or voids. However, as the bioceramic weight percent increased to 30 %, agglomeration of the particles had seen. During the processing of PEEK, some of the bioceramic particles were encapsulated in PEEK matrix and some exposed at the surface [315]. Generally, the surface of pure PEEK is hydrophobic and is not suitable for attaching biomolecules and proteins. The presence of bioceramic particles on the surface of the filament increases its hydrophilicity [10, 228] by acting as bioactive sites for apatite formation, cell attachment and soft tissue adhesion to the surface [258]. The 3D printing of the PEEK with more than 30 wt.% of bioceramic particles would be more problematic due to the higher agglomeration that could block the nozzle and making 3D printing difficult. Additionally, the presence of bioceramic particles increase the viscosity of the polymer at higher temperature [330]. Hence, it would be difficult for material to flow and make the 3D printing more challenging.

The inside distribution of bioceramic particles was observed via μ-CT. The scans showed that the bioceramic particles were uniformly distributed internally as detected on the top surfaces via SEM. The sample of pure PEEK did not contain any particles, as expected. The homogenous dispersion of the bioceramic particles were detected in PEEK composites. The samples contained

10 and 20 wt.% particles, the distribution was more uniform while in 30 wt.% samples there were agglomeration detected [237]. The particle sizes and degree of agglomeration not changed much as was detected in the µ-CT of filaments. Overall, the porosity was detected as less than 2 % with least porosity detected in pure PEEK samples. However, there was not any regular trend of porosity was observed with the weight percent of bioceramic particles.

The elemental analysis and distribution of the bioceramic particles were detected by EDX analysis. In the pure PEEK sample, no other element was detected other than carbon and oxygen, as expected due to the organic nature of PEEK polymer. However, doped-HA particles were detected on the surfaces of composites samples and the distribution of the doped-HA particles were observed via mapping analysis. The mapping results showed that the least amount of bioceramic particles with uniform distribution were present on the surfaces of the samples contained 10 wt.% doped-HA. The highest number of particles were detected in mapping of composite samples contained 30 wt.% bioceramic particles and some degree of agglomeration was also detected. The results were corroborated with SEM and µ-CT results. Hence, as the weight percent increased from 20 %, the agglomeration started which could affect the properties of the samples.

The hydrophilicity of the PEEK surface can be increased with bioceramic particles either by coating of suitable material or making a composite. However, most coating materials are bioresorbable and are not available for longer period during implantation while the amount of bioceramic particles cannot be increased in composites. In this study, both techniques were used and observed their combine effect. The contact angles of composite samples were measured by water droplet. It was observed that the highest contact angle for pure PEEK was measured i.e., 85°. That was due to hydrophobic nature of PEEK surface that did not allow the water droplet to spread over its surface. The hydrophilicity was improved in the composite samples due to the presence of bioceramic particles on the surfaces of the samples [10]. It was observed that the hydrophilicity is directly related to the amount of bioceramic particles. The results showed that the contact angle was decreased to 73.6° and 77.7° for PEEK/10SrHA and PEEK/10ZnHA samples, respectively. It was further decreased with 20 wt.% of bioceramic particles. Hence, lowest angles were detected for the samples contained 30 wt.% of bioceramic particles. This confirmed that the surface wettability was improved as the bioceramic weight percent increased. It was believed that the samples contained 30 wt.% of bioceramic particles would show maximum bioactivity.

Furthermore, the PEEK samples contained 20 wt.% SrHA and ZnHA were selected to coat with PEG_{1000}-DOPA. Pure PEEK samples were used as a reference. The samples were coated by dip coating technique and then dried. The results showed that the hydrophilicity of pure PEEK sample and PEEK/10SrHA sample was tremendously improved with measured contact angles as 20° and 9°, respectively. However, the PEEK/10ZnHA showed peculiar behavior as the hydrophilicity of PEEK/10ZnHA sample was not much affected. The reason could be that the nature of ZnHA particles which did not allow to set PEG_{1000}-DOPA coating on its surface and hence showed a higher contact angle.

The XRD results have confirmed that the 3D printed sample of PEEK was a pure PEEK, no peaks represented the HA peaks and all the peaks matched with the PEEK powder spectra which confirmed that there were not any additional phases present. The data match with the spectra reported in the literature [255, 256]. The peaks of HA were detected in samples containing 10, 20, 30 wt.% of bioceramic particles, as expected. The intensities of peaks corresponded to PEEK polymer were decreased while intensities of doped-HA peaks were increased as the weight percent of the bioceramic particles were increased. The peak positioning and relative intensities of bioceramic particles were accordance to ICDD files # 09-0432 and 00-09-169. It has been discussed in chapter 4 that the peak broadening was due to the presence of Sr and Zn, both elements inhibit crystal growth [293]. The results showed that there were not any additional phases were present other than PEEK, β-TCP and doped-HA after the 3D printing process.

PEEK has received considerable attention in clinical applications because of its excellent mechanical properties, stability and excellent processability. However, PEEK-based implants are biologically inert. In this perspective, the inclusion of inorganic phases into the polymeric matrix aims to enhance PEEK bioactive characteristics. Bioactivity is a prominent feature that manifest with the formation of a HA-like layer on the surface of a material and thus predicts its bone-bonding ability [331]. In this study, the bioactivity of 3D printed PEEK-based composites was analysed through the SBF immersion method and then evaluated *via* physico-chemical analysis such as SEM, EDX, XRD and FTIR. The 3D printed samples were immersed for 7, 14, 28 days in SBF. A sample of PEEK with 10 wt.% of pure HA used as a control to study the effect of doping elements on bioactivity. The surface of pure PEEK samples did not show any sign of apatite formation after 7 days which was expected due to the inert nature of PEEK polymer [10]. It was

observed that small islands of precipitates started forming after 7 days of immersion on the surfaces of PEEK composites. It was observed via SEM images, the extent of those small apatite islands was increased on the surfaces of the samples that contained higher percentage of bioceramic particles. The morphology and EDX results suggested that these small islands of precipitates were apatite particles which started depositing on PEEK composites [10, 261]. The mechanism of apatite formation on the surface of PEEK composite can be explained by the electrostatic interaction between Ca^{+2} on PEEK/doped-HA surface and anions in SBF solution. Initial nucleation of apatite particles starts due to the capturing of anions (HPO_4^{-2}, OH^{-1}) from the SBF solution by Ca^{+2}. Thus, forming metastable phase of calcium hydrogen phosphate which grows and converts into a stable bone-like apatite phase [12]. The growth of apatite precursors was observed as time as well as weight percent dependent and increased after 14 days of immersion, both in terms of size and numbers. The comparison of the results clearly shown that after 14 days of immersion more apatite was formed on the samples contained 20 wt.% of bioceramic particles as compared to the surface of composite contained 10 wt.% bioceramic particles. The similar trend was observed with sample contained 30 wt.% bioceramic particles i.e., more apatite formation found after 14 days on 30 wt.% samples as compared to 10 and 20 wt.% composites. After 28 days, all composite samples showed a significant amount of apatite precipitates on their surface; whereas as expected no apatite formation was detected on the surface of pure PEEK. In addition, based on EDX spectra after 28 days in immersion, the small islands on the surfaces of PEEK composites showed apatite characteristics as demonstrated by the Ca/P ratios. The Ca/P ratios was calculated by dividing the atomic % of Ca and P at different time points. The Ca/P ratios from EDX results suggest that the particles formed after 7 days of immersion are apatite as their ratios are nearly similar to theoretical value i.e., 1.67 [332]. Similarly, the Ca/P ratios of 14 days and 28 days samples are also nearly equal to the theoretical value of stoichiometric HA (Ca/P=1.67). Hence, this demonstrates that the inclusion of bioceramic particles (SrHA and ZnHA), within the pure PEEK matrix supports the formation of an apatite-like layer on its surface [261]. No considerable differences in terms of apatite formation have been detected among the pure HA and its doped forms as reported by the EDX analysis, thus suggesting the promise for them all to be used as bioactive phases. Similar phenomenon has also been reported elsewhere in which researchers have demonstrated the improvement of bioactivity in PEEK polymer by incorporating bioactive ceramics. However, the production route adopted to manufacture bioactive PEEK

composites has been mainly conventional [13, 226, 227, 259, 315, 316]. Conventional technologies such as injection molding, extrusion etc., have inherent limitations, which include length of the processes, costs and lack of customization while 3D printing allows the fabrication of parts with freedom of design and a range of materials with tailorable properties. Overall, these results suggest the suitability of the manufacturing approach for the fabrication of 3D printed bioactive composites based on PEEK, and the possibility to further extend its use in bone regeneration scenarios. Additionally, no major variation in the peaks were found as compared to the spectra of original samples before immersion which could confirm the presence of apatite layer through XRD and FTIR. This could be either due to the thinness of apatite layer or the detection was done on the surface where apatite was not present. Although, the presence of apatite had confirmed via SEM analysis. Hence, this proved that XRD and FTIR equipment are not sensitive enough to detect apatite on the surfaces.

The results of tensile testing data showed that the tensile strength of the composite samples decreased and Young's moduli increased as the percentage of the bioceramic particles in PEEK matrix increased. For pure PEEK, the tensile strength was measured as 75.1 MPa and it was decreased to 51 MPa by the addition of 30 wt.% bioceramic particles. The reduction in tensile strength was due to the bioceramic nature of the particles which act as stress concentrators in the PEEK matrix due to their poor interfacial adhesion with the PEEK polymer [310, 326]. The tensile strength can be enhanced if the interaction between bioceramic particles and PEEK polymer can be increased. In a study, Ma et al. prepared PEEK/HA composite using an in-situ polymerization process and reported that the tensile strength was improved due to the strong interfacial bonding between the HA and PEEK [333], as compared to samples mixed physically [10]. The tensile strength of the PEEK, and its composites were measured higher than the lower range of human cortical bone (50 MPa) [327]. Overall, the Young's modulus of PEEK was increased with the addition of bioceramic particles. This could be the fact that the pure HA is a brittle and the Young's modulus of bulk HA is very high i.e. approximately 130 GPa [334], while the modulus of PEEK is low (2-3 GPa), as a result the composite has an increased value of modulus due to the presence of bioceramic particles [335]. Below the percolation threshold, the other factors affect the mechanical properties of a polymer composite are the size of filler material [336] and % crystallinity [337]. In this study, the modulus increased from 2.9 GPa to 4.1 GPa for pure PEEK and PEEK with 30 wt.% particles, respectively. Considering the results, it is believed that further

increase in bioceramic weight percent will increase the modulus, however that would decrease the tensile strength and also would be difficult to process via 3D printing. The composite contained 30 wt.% of bioceramic particles had highest modulus but lowest tensile strength. The tensile strength of the 30 wt.% bioceramic particles was still higher than 50 MPa, however, it was very close to the lower range of human cortical bone. In a previous study, upto 50 wt.% HA was loaded to prepare PEEK/HA composite, however, 15 to 30 wt.% HA showed good mechanical properties [11]. In another study, 80 wt.% of calcium sulphate was loaded into the PEEK matrix for bone repair applications, again the best composition was 20 wt.% for optimum mechanical performance of the composite [338]. In this study, PEEK with 10 wt.% showed the best mechanical performance, however, it has hypothesized that the composite would show lowest bioactivity which we will discuss in later section. There are several other printing parameters other than bioceramic weight percent that affect the mechanical properties of the 3D printed parts [339]. The other parameters include printing temperature, chamber temperature and the print bed temperature. In this study, the printing temperature of the nozzle had set well above the melting point of the PEEK (343 °C) and its composites. This was due to the higher temperature reduces viscosity and improves flowability so lower the chances of nozzle blockage. Additionally, higher temperature ensures the sufficient melting of the material to improve print quality by fusing layers together and fill any voids [340]. In this study, the samples were printed in a closed chamber to avoid heat wastage and with temperature controls. That also slowed down the cooling rate of 3D printed samples and hence improved the degree of crystallinity. The degree of crystallinity affects the mechanical properties of the samples because the samples which have higher degree of crystallinity usually have higher mechanical properties [341]. Generally, the considerable difference between nozzle temperature and chamber temperature cause warping in the 3D printed parts. Hence, higher chamber temperature allows rapid and good crystallization of the samples [342]. In this study, the highest recommended chamber temperature was used (80 °C) and the degree of crystallinity was measured between 29 to 32 % which was close to the reported value [343]. Hence, due to the combination of printing temperature, print-bed temperature and chamber temperature, the good quality 3D printed samples were prepared without shrinkage and with minimum porosity. Additionally, the printhead nozzle diameter and layer thickness also influence the mechanical properties of the 3D printed samples. Generally, good mechanical properties are achieved by using lower diameter nozzle and lower layer thickness. In this study, 0.5 mm diameter

nozzle was used, that also ensured the smooth flowability of polymer contained bioceramic particles without the nozzle blockage. Additionally, the layer thickness used in this study was 0.2 mm to ensure the layer completely fused together and filling any gaps present. In the literature, 0.3 mm layer thickness was used to 3D print samples and achieved best mechanical properties [343, 344]. It was reported that the high layer thickness reduces the mechanical properties of 3D printed parts [344]. Furthermore, the mechanical performance of the 3D printed parts is influenced by print orientation, raster angle and print speed. Commonly, the best mechanical properties are achieved when samples are printed in horizontal direction with raster angle 0 while worst and intermediate properties are measured when raster angle was 90° and 45° [343]. In this study, all the samples were printed horizontally with raster angle 0°. However, -45°, +45° were used for printing infill pattern. The printing speed is inversely proportional to the mechanical properties, higher printing speed produces low mechanical strength parts and low printing speed produces high strength parts. During printing at high speed, the layers do not get enough time to properly diffuse and crystallize [344]. In this study an intermediate printing speed was used i.e., 30 millimeter per seconds. The exemplars of stress-strain graphs have been given in supplementary information in Figure 40.

PEEK composite samples with 20 wt.% of bioceramic particles (PEEK/20SrHA and PEEK/20ZnHA) were selected to study the effect of apatite layer on mechanical properties. As per author's knowledge, this has been studied the first time so there is a lack of literature. It is important study which will tell us how mechanical properties of bioactive implant varied when put in human body and interact with body fluid. Initially, the tensile strengths of the samples before immersion were 58 and 59 MPa for PEEK/20SrHA and PEEK/ZnHA samples, respectively. It was noted that after the first 7 days of immersion approximately 5 % tensile strength was reduced in both samples. Moreover, no further reduction in strength was measured after 14 days. However, after 28 days a slight improvement in the mechanical strength was observed, however, it was not greater that the initial tensile strengths of the samples. The overall strength of the samples can be considered as constant with a little change in the properties. The slight variation in the strength could be due to the print consistency and crystallinity.

Commonly, craniofacial injuries arise due to the impact loading such as road accident or in sports. It is vital to investigate the impact behavior of the 3D printed parts. The impact strength

of human cranial bone depends of various factors such as type of bone, age of person and rate of the loading [345]. The results obtained closely matched with the impact strength of skull bone reported in the literature i.e., 3 to 9 kJ/m^2 [59]. Saha and Hayes [345] measured the impact strengths of fresh and embalmed skull bones and reported the impact strength as 18 kJ/m^2 and 14 kJ/m^2, respectively. Delille et al. [328] measured the mechanical properties of different types of cranial bones. They had tested nineteen specimens (5 frontal, 8 parietal, 2 temporal, 1 occipital, 2 on the coronal suture and 1 on the sagittal suture) from each 20 skulls from un-embalmed cadavers. They have found that each type of bone had different mechanical properties. In this study, it was observed that the impact energy decreased as the weight percent of bioceramic particles in PEEK increased. This could be due to the poor adhesion between bioceramic particles and PEEK polymer. These particles act as stress raisers and reason to break the sample early. The presence of more particles provides more defected sites which in a result break the sample early. As discussed in previous section that the tensile strength was slightly decreased after 7 days of immersion in SBF and improved after 28 days of immersion. This could also be hypothesized for impact strength that after longer period, the impact strength of implant would be improved. However, further studies are required to investigate the effect of SBF on mechanical properties for longer immersion time.

7 Chapter 7: Conclusions and Recommendations for Future Work

7.1 Conclusions

In this study, PEEK and its nanocomposites with SrHA and ZnHA up to 30 wt.% have been processed successfully by novel route i.e., FFF 3D printing, and the parameters for filament extrusion and 3D printing processes were optimized. SrHA and ZnHA nanoparticles were synthesized by wet-chemical precipitation method. XRD analysis confirmed the presence of β-TCP along with HA in sintered powders. Additionally, 1.75 mm diameter filaments were obtained via extrusion. Micro-CT and SEM analysis suggested a uniform distribution of bioceramic particles in PEEK filaments. Three-dimensional-printed samples were successfully fabricated via FFF and characterized via XRD, SEM, DSC, water contact angle, tensile testing before and after SBF immersion and impact testing. SEM showed that the bioceramic particles were uniformly distributed on the surfaces and played a role in the bioactivity of the samples in SBF. DSC results showed the melting points and crystallinity of nanocomposites increased by the addition of bioceramic particles up to 30 wt.% from 343 °C to 355 °C and 27.7% to 34.6%, respectively. In the presence of bioceramic particles, the surface hydrophilicity of nanocomposites, as indicated by water contact angle values was considerably improved from 85° to 55° which further decreased to 10° after coating with PEG_{1000}-DOPA. Moreover, it was observed that the tensile of PEEK decreased from 75 MPa to 51 MPa with the addition of SrHA and ZnHA up to 30 wt.%, which could be attributed to the weak attachment between PEEK and bioceramic particles and their brittle nature. However, the elastic modulus and bioactivity -as indicated by SBF immersion studies- increased with the addition of bioceramic particles, due to the stiffness and bioactive nature of the particles, respectively. Samples containing 20 wt.% bioceramic were selected for tensile testing after SBF immersion. There was no considerable change in mechanical properties were detected. In addition, impact strength decreased from 14 kJ/m^2 to 4 kJ/m^2 by the addition of bioceramic particles up to 30 wt.% and in the range of impact strength of human skull bone. Overall, the study showed that PEEK/SrHA and PEEK/ZnHA nanocomposites can be successfully processed via FFF, and the resulting 3D-printed nanocomposites have great potential for use in manufacturing craniomaxillofacial implants.

7.2 Recommendations for Future Work

There are following recommendations for future research:

- Although, optimization of extrusion and 3D printing has been reported, still there is a room for improvement in print quality and mechanical properties. Hence, 3D printing parameters such as bed temperature, chamber temperature, printhead temperature, etc., can be further optimized to obtain samples with improved mechanical properties.
- The coating of PEG_{1000}-DOPA has demonstrated positive effect on the hydrophilicity of the samples. Hence, the effect of PEG_{1000}-DOPA coating on the mechanical properties such as tensile strength, impact strength, elastic modulus, and biological properties such as apatite layer formation ability in SBF, cell attachment, cell proliferation, can be evaluated in future.
- Further biological studies such as pre-osteoblast cells attachment, proliferation and cytotoxicity can be performed on the 3D printed samples to assess the cell responses and cytotoxicity of the samples.
- The effect of SBF on mechanical properties has been calculated for up to 28 days for the first time in this study. However, a long-term evaluation is required to study the effect of SBF solution on the mechanical properties of the samples. This would be important and give vital information about the mechanical behaviour of implant in human body.
- Functionally graded structures can be produced which are porous from inside while dense from outside to mimic the human bone. Furthermore, as it has been concluded that presence of HA or doped-HA is essential for biological activities however it has negative effect on the mechanical properties. The concentration of HA or doped-HA could be varied such that HA would be printed only in outer surface while inner surface would remain pure PEEK polymer to obtain maximum mechanical as well as biological properties.

8 Supplementary Information

8.1 Tensile testing graphs

The stress-strain graphs which are obtained after tensile testing are given below as exemplar:

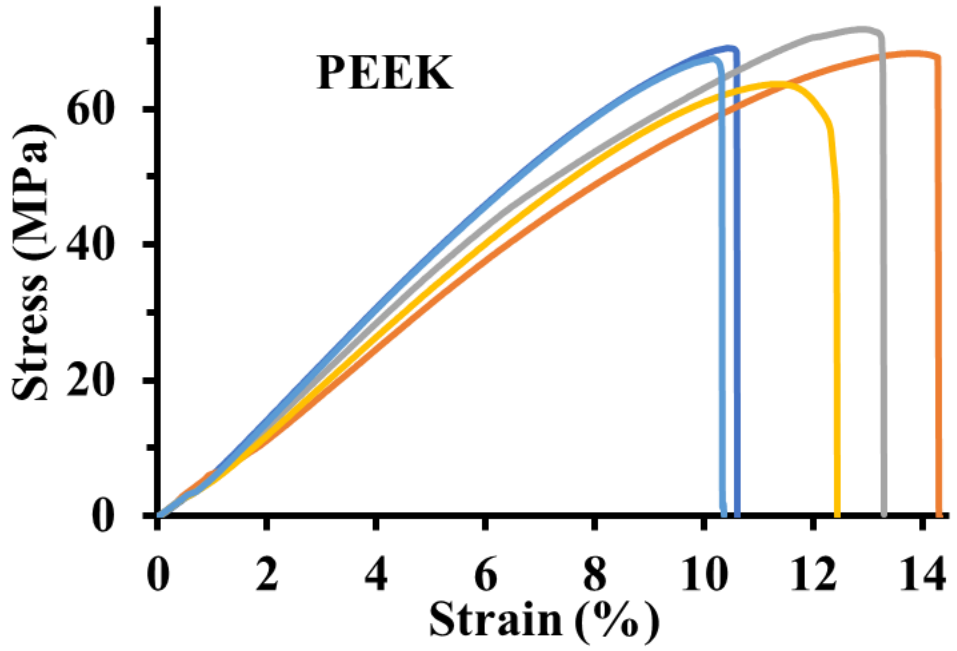

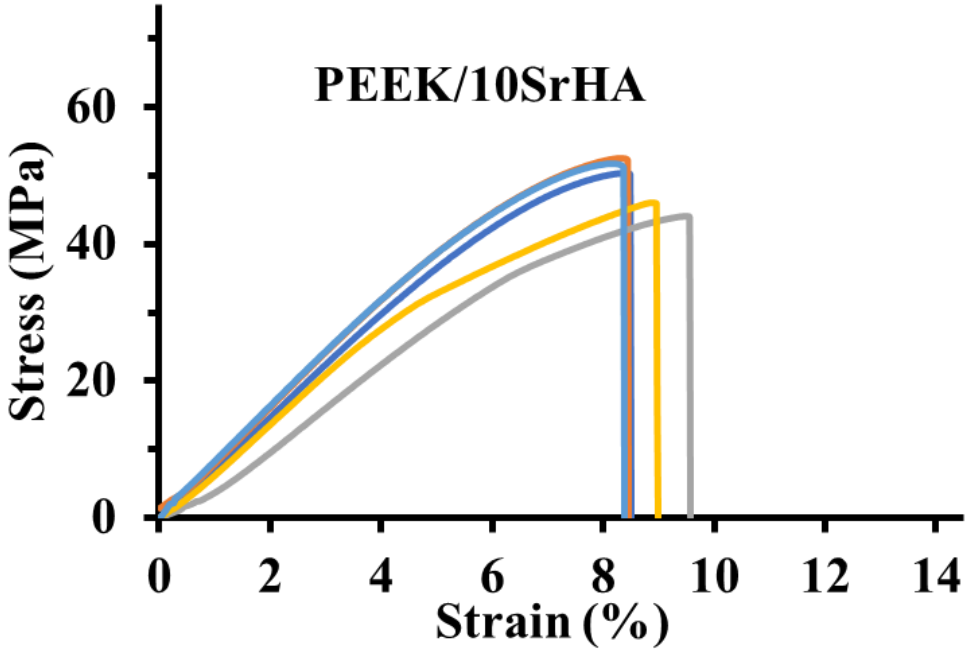

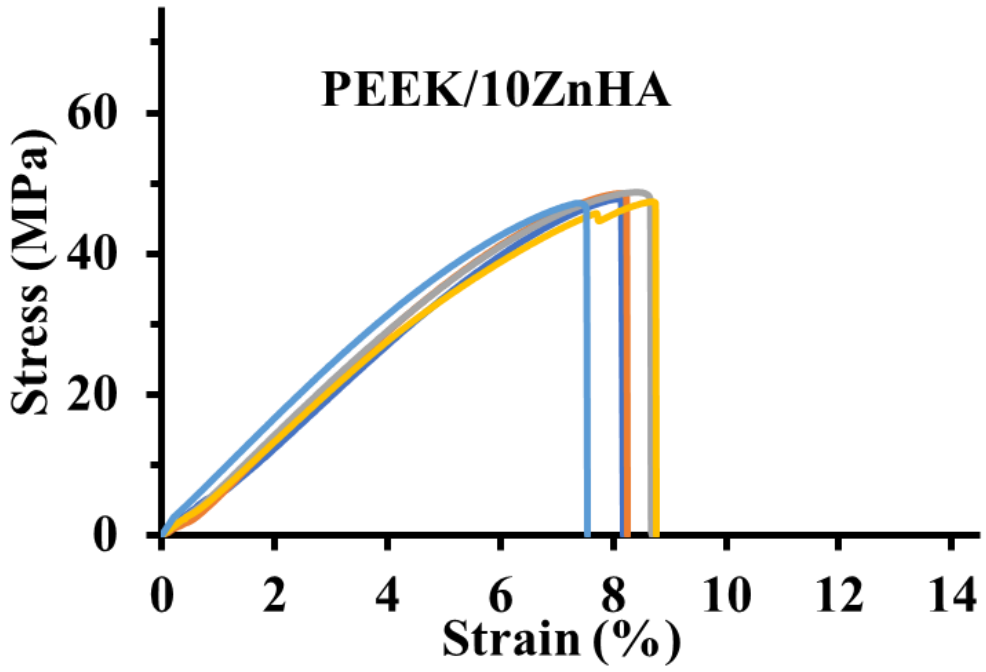

Figure 40 Stress-strain curves of tensile testing of 3D printed PEEK, PEEK/10SrHA and PEEK/10ZnHA, total 5 specimen were tested for each sample

9 References

1. Carter, R., *The brain book: An illustrated guide to its structure, functions, and disorders*. 2019: Dorling Kindersley Ltd.
2. Rommel, S.A., D.A. Pabst, and W.A. McLellan, *Skull anatomy*, in *Encyclopedia of marine mammals*. 2009, Elsevier. p. 1033-1047.
3. Luo, Y., et al., *Cutting Behavior of Cortical Bone in Different Bone Osteon Cutting Angles and Depths of Cut.* Chinese Journal of Mechanical Engineering, 2022. **35**(1): p. 1-12.
4. Nauth, A., et al., *Critical-size bone defects: is there a consensus for diagnosis and treatment?* Journal of orthopaedic trauma, 2018. **32**: p. S7-S11.
5. Jindal, S., et al., *3D printed composite materials for craniofacial implants: current concepts, challenges and future directions.* The International Journal of Advanced Manufacturing Technology, 2021. **112**(3): p. 635-653.
6. Fraile-Martínez, O., et al., *Applications of Polymeric Composites in Bone Tissue Engineering and Jawbone Regeneration.* Polymers, 2021. **13**(19): p. 3429.
7. Jung, H.-D., et al., *Enhanced bioactivity of titanium-coated polyetheretherketone implants created by a high-temperature 3D printing process.* Biofabrication, 2019. **11**(4): p. 045014.
8. Han, X., et al., *Carbon fiber reinforced PEEK composites based on 3D-printing technology for orthopedic and dental applications.* Journal of clinical medicine, 2019. **8**(2): p. 240.
9. Noiset, O., Y.-J. Schneider, and J. Marchand-Brynaert, *Fibronectin adsorption or/and covalent grafting on chemically modified PEEK film surfaces.* Journal of Biomaterials Science, Polymer Edition, 1999. **10**(6): p. 657-677.
10. Ma, R. and D. Guo, *Evaluating the bioactivity of a hydroxyapatite-incorporated polyetheretherketone biocomposite.* Journal of Orthopaedic Surgery and Research, 2019. **14**(1): p. 32.
11. Oladapo, B.I., et al., *3D printing of PEEK–cHAp scaffold for medical bone implant.* Bio-Design and Manufacturing, 2021. **4**(1): p. 44-59.

12. Yu, S., et al., *In vitro apatite formation and its growth kinetics on hydroxyapatite/polyetheretherketone biocomposites.* Biomaterials, 2005. **26**(15): p. 2343-2352.
13. Zhao, M., et al., *Response of human osteoblast to n-HA/PEEK—quantitative proteomic study of bio-effects of nano-hydroxyapatite composite.* Scientific reports, 2016. **6**(1): p. 1-13.
14. Fathi, M., A. Hanifi, and V. Mortazavi, *Preparation and bioactivity evaluation of bone-like hydroxyapatite nanopowder.* Journal of materials processing technology, 2008. **202**(1-3): p. 536-542.
15. Graziani, G., M. Boi, and M. Bianchi, *A review on ionic substitutions in hydroxyapatite thin films: Towards complete biomimetism.* Coatings, 2018. **8**(8): p. 269.
16. Huang, Z., et al., *Strontium/Chitosan/Hydroxyapatite/Norcantharidin Composite That Inhibits Osteosarcoma and Promotes Osteogenesis In Vitro.* BioMed research international, 2020. **2020**.
17. Porter, A., et al., *Comparison of in vivo dissolution processes in hydroxyapatite and silicon-substituted hydroxyapatite bioceramics.* Biomaterials, 2003. **24**(25): p. 4609-4620.
18. Stipniece, L., et al., *Characterization of Mg-substituted hydroxyapatite synthesized by wet chemical method.* Ceramics International, 2014. **40**(2): p. 3261-3267.
19. Thian, E., et al., *Zinc-substituted hydroxyapatite: a biomaterial with enhanced bioactivity and antibacterial properties.* Journal of Materials Science: Materials in Medicine, 2013. **24**(2): p. 437-445.
20. Deng, Y., et al., *Effect of surface roughness on osteogenesis in vitro and osseointegration in vivo of carbon fiber-reinforced polyetheretherketone–nanohydroxyapatite composite.* International journal of nanomedicine, 2015. **10**: p. 1425.
21. Ventola, C.L., *Medical applications for 3D printing: current and projected uses.* Pharmacy and Therapeutics, 2014. **39**(10): p. 704.
22. Rinaldi, M., et al., *Additive layer manufacturing of poly (ether ether ketone) via FDM.* Composites Part B: Engineering, 2018. **145**: p. 162-172.
23. Valentan, B., et al., *Processing poly (ether etherketone) an a 3D printer for thermoplastic modelling.* Materiali in tehnologije, 2013. **47**(6): p. 715-721.

24. Pisula, J., et al., *An analysis of polymer gear wear in a spur gear train made using FDM and FFF methods based on tooth surface topography assessment.* Polymers, 2021. **13**(10): p. 1649.
25. Low, Z.-X., et al., *Perspective on 3D printing of separation membranes and comparison to related unconventional fabrication techniques.* Journal of membrane science, 2017. **523**: p. 596-613.
26. Guo, P., et al., *Study on microstructure, mechanical properties and machinability of efficiently additive manufactured AISI 316L stainless steel by high-power direct laser deposition.* Journal of Materials Processing Technology, 2017. **240**: p. 12-22.
27. Guo, N. and M.C. Leu, *Additive manufacturing: technology, applications and research needs.* Frontiers of Mechanical Engineering, 2013. **8**(3): p. 215-243.
28. Heller, M., et al., *Applications of patient-specific 3D printing in medicine.* International journal of computerized dentistry, 2016. **19**(4): p. 323-339.
29. Raffaini, P. and L. Manfredi, *Chapter 15 - Project management*, in *Endorobotics*, L. Manfredi, Editor. 2022, Academic Press. p. 337-358.
30. Ismail, A., *Mathematical description for human knee joint geometry and its effect on lubrication mechanisms.* International Review of Mechanical Engineering, 2010. **4**(6): p. 761-779.
31. Visscher, D.O., et al., *Advances in bioprinting technologies for craniofacial reconstruction.* Trends in biotechnology, 2016. **34**(9): p. 700-710.
32. Siswanto, W.A. and C.S. Hua, *Strength analysis of human skull on high speed impact.* Corrosion Detection in 'T'Bend Oil Pipelines Based on Fuzzy Implementation, 2012. **3**: p. 1508.
33. Dewan, M.C., et al., *Estimating the global incidence of traumatic brain injury.* Journal of neurosurgery, 2018. **130**(4): p. 1080-1097.
34. Sanan, A. and S.J. Haines, *Repairing holes in the head: a history of cranioplasty.* Neurosurgery, 1997. **40**(3): p. 588-603.
35. Servadei, F. and C. Iaccarino, *The therapeutic cranioplasty still needs an ideal material and surgical timing.* World neurosurgery, 2015. **83**(2): p. 133.
36. Shah, A.M., H. Jung, and S. Skirboll, *Materials used in cranioplasty: a history and analysis.* Neurosurgical focus, 2014. **36**(4): p. E19.

37. Goldstein, J.A., J.T. Paliga, and S.P. Bartlett, *Cranioplasty: indications and advances.* Current opinion in otolaryngology & head and neck surgery, 2013. **21**(4): p. 400-409.
38. Dewan, M.C., et al., *Estimating the global incidence of traumatic brain injury.* J Neurosurg, 2018: p. 1-18.
39. Maas, A.I., et al., *Traumatic brain injury: integrated approaches to improve prevention, clinical care, and research.* The Lancet Neurology, 2017. **16**(12): p. 987-1048.
40. Davis, T. and A. Ings, *Head injury: triage, assessment, investigation and early management of head injury in children, young people and adults (NICE guideline CG 176).* Archives of disease in childhood - Education & practice edition, 2015. **100**(2): p. 97-100.
41. Marincowitz, C., et al., *Evaluation of the impact of the NICE head injury guidelines on inpatient mortality from traumatic brain injury: an interrupted time series analysis.* BMJ open, 2019. **9**(6): p. e028912.
42. *Grand View Research, Inc.* https://www.grandviewresearch.com/press-release/global-cmf-devices-market.
43. Sahoo, D., et al., *Development of skull fracture criterion based on real-world head trauma simulations using finite element head model.* Journal of the mechanical behavior of biomedical materials, 2016. **57**: p. 24-41.
44. Restak, R., *Fixing the brain, mysteries of the mind.* Washington, DC: National Geographic Society, 2000. **256**.
45. Dwivedi, G. and S. Dwivedi, *Sushruta-the clinician-teacher par excellence.* Indian Journal of Chest Diseases and Allied Sciences, 2007. **49**(4): p. 243.
46. Tsoucalas, G. and M. Sgantzos, *Paul of Aegina (ca 625-690 AD), and his orthopaedic surgical reconstruction of the preternatural fingers.* International Orthopaedics, 2017. **41**(1): p. 211-216.
47. Bonfield, C.M., A.R. Kumar, and P.C. Gerszten, *The history of military cranioplasty.* Neurosurgical focus, 2014. **36**(4): p. E18.
48. Moghaddam, N., et al., *Survival after trepanation—Early cranial surgery from Late Iron Age Switzerland.* International Journal of Paleopathology, 2015. **11**: p. 56-65.

49. Janecka, I.P., *New reconstructive technologies in skull base surgery: role of titanium mesh and porous polyethylene.* Archives of Otolaryngology–Head & Neck Surgery, 2000. **126**(3): p. 396-401.
50. Dujovny, M., et al., *Cranioplasty: cosmetic or therapeutic?* Surgical neurology, 1997. **47**(3): p. 238-241.
51. Wehmöller, M., et al. *CAD/CAM-prefabricated titanium implants for large skull defects—clinical experience with 166 patients from 1994 to 2000*. in *International Congress Series*. 2004. Elsevier.
52. Poukens, J., et al., *A classification of cranial implants based on the degree of difficulty in computer design and manufacture.* The International Journal of Medical Robotics and Computer Assisted Surgery, 2008. **4**(1): p. 46-50.
53. McElhaney, J.H., et al., *Mechanical properties of cranial bone.* Journal of biomechanics, 1970. **3**(5): p. 495-511.
54. Boskey, A.L., *Bone composition: relationship to bone fragility and antiosteoporotic drug effects.* BoneKEy reports, 2013. **2**.
55. Feerick, E.M. and J.P. McGarry, *Cortical bone failure mechanisms during screw pullout.* Journal of biomechanics, 2012. **45**(9): p. 1666-1672.
56. Rho, J.-Y., L. Kuhn-Spearing, and P. Zioupos, *Mechanical properties and the hierarchical structure of bone.* Medical engineering & physics, 1998. **20**(2): p. 92-102.
57. Evans, F.G., *Mechanical properties of bone*. 1973: Thomas Springfield:.
58. Snyder, S.M. and E. Schneider, *Estimation of mechanical properties of cortical bone by computed tomography.* Journal of Orthopaedic Research, 1991. **9**(3): p. 422-431.
59. Motherway, J.A., et al., *The mechanical properties of cranial bone: The effect of loading rate and cranial sampling position.* Journal of Biomechanics, 2009. **42**(13): p. 2129-2135.
60. Khoury, F. and R. Buchmann, *Surgical therapy of peri-implant disease: a 3-year follow-up study of cases treated with 3 different techniques of bone regeneration.* J Periodontol, 2001. **72**(11): p. 1498-508.
61. Esposito, M., et al., *Interventions for replacing missing teeth: bone augmentation techniques for dental implant treatment.* Cochrane Database Syst Rev, 2008(3): p. Cd003607.

62. Hallman, M. and A. Thor, *Bone substitutes and growth factors as an alternative/complement to autogenous bone for grafting in implant dentistry.* Periodontol 2000, 2008. **47**: p. 172-92.
63. Artico, M., et al., *Bone autografting of the calvaria and craniofacial skeleton: historical background, surgical results in a series of 15 patients, and review of the literature.* Surgical neurology, 2003. **60**(1): p. 71-79.
64. Raulo, Y. and J. Baruch, *Use of the calvarium for bone grafting in cranio-maxillo-facial surgery.* Chirurgie; memoires de l'Academie de chirurgie, 1990. **116**(4-5): p. 359-362.
65. Keating, J.F., A.H. Simpson, and C.M. Robinson, *The management of fractures with bone loss.* J Bone Joint Surg Br, 2005. **87**(2): p. 142-50.
66. Parthasarathy, J., *3D modeling, custom implants and its future perspectives in craniofacial surgery.* Annals of maxillofacial surgery, 2014. **4**(1): p. 9-18.
67. Silber, J.S., et al., *Donor site morbidity after anterior iliac crest bone harvest for single-level anterior cervical discectomy and fusion.* Spine (Phila Pa 1976), 2003. **28**(2): p. 134-9.
68. Tavares, A., et al., *Metal Injection Molding for Production of Biodegradable Implants: An Analysis of the Potential of Pure Iron for Application in Stents.* American Journal of Materials Science, 2019. **9**(2): p. 36-43.
69. Durand, J.-L., D. Renier, and D. Marchac. *The history of cranioplasty*. in *Annales de chirurgie plastique et esthetique*. 1997.
70. Abhay, S. and S.J. Haines, *Repairing holes in the head: a history of cranioplasty.* Neurosurgery, 1997. **40**(3): p. 588-603.
71. Harris, D.A., et al., *History of synthetic materials in alloplastic cranioplasty.* Neurosurgical focus, 2014. **36**(4): p. E20.
72. Ballard, N. and J.M. Asua, *Radical polymerization of acrylic monomers: An overview.* Progress in Polymer Science, 2018. **79**: p. 40-60.
73. Malis, L.I., *Titanium mesh and acrylic cranioplasty.* Neurosurgery, 1989. **25**(3): p. 351-355.
74. Karunakaran, K., et al., *Rapid manufacturing of metallic objects.* Rapid Prototyping Journal, 2012. **18**(4): p. 264-280.
75. Pilliar, R.M., *Metallic biomaterials*, in *Biomedical materials*. 2009, Springer. p. 41-81.

76. Manuel de A. Monteiro Ramos, A. and J. António Simões, *CAD-CAM-RTV–lost-wax casting technology for medical implants.* Rapid Prototyping Journal, 2009. **15**(3): p. 211-215.
77. Pilliar, R., *Powder metal-made orthopedic implants with porous surface for fixation by tissue ingrowth.* Clinical orthopaedics and related research, 1983(176): p. 42-51.
78. Lopez-Esteban, S., et al., *Bioactive glass coatings for orthopedic metallic implants.* Journal of the European Ceramic Society, 2003. **23**(15): p. 2921-2930.
79. Bobyn, J., et al., *The optimum pore size for the fixation of porous-surfaced metal implants by the ingrowth of bone.* Clinical orthopaedics and related research, 1980(150): p. 263-270.
80. Rothen-Weinhold, A., et al., *Injection-molding versus extrusion as manufacturing technique for the preparation of biodegradable implants.* European journal of pharmaceutics and biopharmaceutics, 1999. **48**(2): p. 113-121.
81. Yalcin, B. and S.E. Amos, *3 - Hollow Glass Microspheres in Thermoplastics*, in *Hollow Glass Microspheres for Plastics, Elastomers, and Adhesives Compounds*, S.E. Amos and B. Yalcin, Editors. 2015, William Andrew Publishing: Oxford. p. 35-105.
82. Joffe, J.M., et al., *Computer-generated titanium cranioplasty: report of a new technique for repairing skull defects.* British journal of neurosurgery, 1992. **6**(4): p. 343-350.
83. Blake, D.P., *The use of synthetics in cranioplasty: a clinical review.* Military medicine, 1994. **159**(6): p. 466-469.
84. Hench, L. and E. Ethridge, *Biomaterials, an Interfacial Approach, Biophysics and Bioengineering Series Vol. 4*. 1982, Academic Press, New York.
85. Black, S.P., *Reconstruction of the supraorbital ridge using aluminum.* Surg Neurol, 1978. **9**(2): p. 121-8.
86. Jorgenson, D.S., et al., *Detection of titanium in human tissues after craniofacial surgery.* Plast Reconstr Surg, 1997. **99**(4): p. 976-9; discussion 980-1.
87. Hille, G.H., *Titanium for surgical implants.* J MATER, 1966. **1**(2): p. 373-383.
88. Branemark, P.-I., *Osseointegration and its experimental background.* J prosthet Dent, 1983. **50**: p. 399-410.
89. Niinomi, M. and M. Nakai, *Titanium-based biomaterials for preventing stress shielding between implant devices and bone.* International journal of biomaterials, 2011. **2011**.

90. Huiskes, R., H. Weinans, and B. Van Rietbergen, *The relationship between stress shielding and bone resorption around total hip stems and the effects of flexible materials.* Clinical orthopaedics and related research, 1992: p. 124-134.
91. Noyama, Y., et al., *Bone loss and reduced bone quality of the human femur after total hip arthroplasty under stress-shielding effects by titanium-based implant.* Materials transactions, 2012. **53**(3): p. 565-570.
92. Raffa, M.L., et al., *Stress shielding at the bone-implant interface: Influence of surface roughness and of the bone-implant contact ratio.* Journal of Orthopaedic Research®, 2021. **39**(6): p. 1174-1183.
93. Taddei, E.B., et al., *Production of new titanium alloy for orthopedic implants.* Materials Science and Engineering: C, 2004. **24**(5): p. 683-687.
94. Disegi, J.A., *Titanium alloys for fracture fixation implants.* Injury, 2000. **31**: p. D14-D17.
95. Arabnejad, S., et al., *Fully porous 3D printed titanium femoral stem to reduce stress-shielding following total hip arthroplasty.* Journal of Orthopaedic Research, 2017. **35**(8): p. 1774-1783.
96. Oh, I.-H., et al., *Mechanical properties of porous titanium compacts prepared by powder sintering.* Scripta Materialia, 2003. **49**(12): p. 1197-1202.
97. Shi, J., et al., *Design and fabrication of graduated porous Ti-based alloy implants for biomedical applications.* Journal of Alloys and Compounds, 2017. **728**: p. 1043-1048.
98. Shanjani, Y., et al., *Solid freeform fabrication and characterization of porous calcium polyphosphate structures for tissue engineering purposes.* Journal of Biomedical Materials Research Part B: Applied Biomaterials, 2010. **93**(2): p. 510-519.
99. Petrovic, V., et al., *Additive manufacturing solutions for improved medical implants*, in *Biomedicine*. 2012, IntechOpen.
100. Parthasarathy, J., B. Starly, and S. Raman, *A design for the additive manufacture of functionally graded porous structures with tailored mechanical properties for biomedical applications.* Journal of Manufacturing Processes, 2011. **13**(2): p. 160-170.
101. Chang, C.-H., et al., *3D printing bioceramic porous scaffolds with good mechanical property and cell affinity.* PloS one, 2015. **10**(11): p. e0143713.
102. Spiessl, B., *Erfahrungen mit dem AO-Besteck bei Kieferbruchbehandlungen.* Schweiz Mschr Zahnmed, 1969. **79**(2): p. 112-113.

103. Kuroda, D., et al., *Corrosion behavior of nickel-free high nitrogen austenitic stainless steel in simulated biological environments.* Materials Transactions, 2002. **43**(12): p. 3100-3104.
104. Bal, W., H. Kozłowski, and K.S. Kasprzak, *Molecular models in nickel carcinogenesis.* Journal of Inorganic Biochemistry, 2000. **79**(1): p. 213-218.
105. Adams, K., et al., *In vitro and in vivo evaluation of antibiotic diffusion from antibiotic-impregnated polymethylmethacrylate beads.* Clin Orthop Relat Res, 1992(278): p. 244-52.
106. Aydin, S., et al., *Cranioplasty: Review of materials and techniques.* Journal of neurosciences in rural practice, 2011. **2**(2): p. 162-167.
107. Diker, N., et al., *Effects of Hyaluronic Acid and Hydroxyapatite/Beta-tricalcium Phosphate in Combination on Bone Regeneration of a Critical-size Defect in an Experimental Model.* J Craniofac Surg, 2018. **29**(4): p. 1087-1093.
108. Fan, H., et al., *Efficacy of prevascularization for segmental bone defect repair using beta-tricalcium phosphate scaffold in rhesus monkey.* Biomaterials, 2014. **35**(26): p. 7407-15.
109. Iwasashi, M., et al., *Bone Regeneration and Remodeling within a Unidirectional Porous Hydroxyapatite Bone Substitute at a Cortical Bone Defect Site: Histological Analysis at One and Two Years after Implantation.* Materials (Basel, Switzerland), 2015. **8**(8): p. 4884-4894.
110. Valimaki, V.V. and H.T. Aro, *Molecular basis for action of bioactive glasses as bone graft substitute.* Scand J Surg, 2006. **95**(2): p. 95-102.
111. Sasaki, G., et al., *Induced membrane technique using beta-tricalcium phosphate for reconstruction of femoral and tibial segmental bone loss due to infection: technical tips and preliminary clinical results.* Int Orthop, 2018. **42**(1): p. 17-24.
112. Sumer, M., et al., *Autogenous cortical bone and bioactive glass grafting for treatment of intraosseous periodontal defects.* Eur J Dent, 2013. **7**(1): p. 6-14.
113. Daga, D., et al., *Tentpole technique for bone regeneration in vertically deficient alveolar ridges: A prospective study.* Journal of oral biology and craniofacial research, 2018. **8**(1): p. 20-24.
114. Jardini, A.L., et al., *Cranial reconstruction: 3D biomodel and custom-built implant created using additive manufacturing.* J Craniomaxillofac Surg, 2014. **42**(8): p. 1877-84.

115. https://www.chemtube3d.com/sshydroxyapatite/, Access date (11 September 2022).
116. Swiatkowska, I., N. Martin, and A.J. Hart, *Blood titanium level as a biomarker of orthopaedic implant wear.* Journal of Trace Elements in Medicine and Biology, 2019. **53**: p. 120-128.
117. Golz, T., et al., *Temperature elevation during simulated polymethylmethacrylate (PMMA) cranioplasty in a cadaver model.* J Clin Neurosci, 2010. **17**(5): p. 617-22.
118. Eppley, B.L., *Biomechanical testing of alloplastic PMMA cranioplasty materials.* Journal of Craniofacial Surgery, 2005. **16**(1): p. 140-143.
119. Abuzayed, B., et al., *Reconstruction of growing skull fracture with in situ galeal graft duraplasty and porous polyethylene sheet.* J Craniofac Surg, 2009. **20**(4): p. 1245-9.
120. Abuzayed, B., et al., *Aneurysmal frontal bone cyst in a child with history of acute lymphoblastic leukemia: a case of rare location and history.* J Pediatr Hematol Oncol, 2010. **32**(1): p. e1-3.
121. Kucukyuruk, B., et al., *Intraosseous meningioma: a rare tumor reconstructed with porous polyethylene.* J Craniofac Surg, 2010. **21**(3): p. 936-9.
122. Couldwell, W.T., et al., *Cranioplasty with the Medpor porous polyethylene Flexblock implant.* Journal of neurosurgery, 1994. **81**(3): p. 483-486.
123. Suwanprateeb, J., et al., *Manufacturing of Porous Polyethylene Ocular Implant by Three Dimensional Printing.* King Mongkut's University of Technology North Bangkok International Journal of Applied Science and Technology, 2010. **3**(4): p. 23-28.
124. Kurtz, S.M. and J.N. Devine, *PEEK biomaterials in trauma, orthopedic, and spinal implants.* Biomaterials, 2007. **28**(32): p. 4845-69.
125. Dandy, L.O., et al., *Accelerated degradation of Polyetheretherketone (PEEK) composite materials for recycling applications.* Polymer Degradation and Stability, 2015. **112**: p. 52-62.
126. Krätzig, T., et al., *Carbon fiber–reinforced PEEK versus titanium implants: an in vitro comparison of susceptibility artifacts in CT and MR imaging.* Neurosurgical Review, 2021. **44**(4): p. 2163-2170.
127. Ponnappan, R.K., et al., *Biomechanical evaluation and comparison of polyetheretherketone rod system to traditional titanium rod fixation.* The Spine Journal, 2009. **9**(3): p. 263-267.

128. Manea, A., et al., *Sterilization protocol for porous dental implants made by Selective Laser Melting.* Clujul medical (1957), 2018. **91**(4): p. 452-457.
129. Godara, A., D. Raabe, and S. Green, *The influence of sterilization processes on the micromechanical properties of carbon fiber-reinforced PEEK composites for bone implant applications.* Acta Biomaterialia, 2007. **3**(2): p. 209-220.
130. Kumar, A., et al., *Effects of sterilization cycles on PEEK for medical device application.* Bioengineering, 2018. **5**(1): p. 18.
131. Kurtz, S.M., *Chemical and radiation stability of PEEK*, in *PEEK biomaterials handbook.* 2012, Elsevier. p. 75-79.
132. Najeeb, S., et al., *Applications of polyetheretherketone (PEEK) in oral implantology and prosthodontics.* Journal of prosthodontic research, 2016. **60**(1): p. 12-19.
133. Zhao, F., D. Li, and Z. Jin, *Preliminary investigation of poly-ether-ether-ketone based on fused deposition modeling for medical applications.* Materials, 2018. **11**(2): p. 288.
134. Goldsmith, D., A. Horowitz, and G. Orentlicher, *Facial skeletal augmentation using custom facial implants.* Atlas Oral Maxillofac Surg Clin North Am, 2012. **20**(1): p. 119-34.
135. Williams, D.F., A. McNamara, and R.M. Turner, *Potential of polyetheretherketone (PEEK) and carbon-fibre-reinforced PEEK in medical applications.* Journal of Materials Science Letters, 1987. **6**(2): p. 188-190.
136. Arima, Y. and H. Iwata, *Effect of wettability and surface functional groups on protein adsorption and cell adhesion using well-defined mixed self-assembled monolayers.* Biomaterials, 2007. **28**(20): p. 3074-82.
137. Hanasono, M.M., N. Goel, and F. DeMonte, *Calvarial reconstruction with polyetheretherketone implants.* Ann Plast Surg, 2009. **62**(6): p. 653-5.
138. Li, H., et al., *The effects on polyetheretherketone and polyethersulfone of electron and/spl gamma/irradiation.* IEEE transactions on dielectrics and electrical insulation, 1999. **6**(3): p. 295-303.
139. Zheng, Z., et al., *Strategies to improve bioactive and antibacterial properties of polyetheretherketone (PEEK) for use as orthopedic implants.* Materials Today Bio, 2022: p. 100402.

140. Hyun, J.S., et al., *The seed and the soil: optimizing stem cells and their environment for tissue regeneration.* Annals of plastic surgery, 2013. **70**(2): p. 235-239.
141. Zhang, X., et al., *Polymer-ceramic spiral structured scaffolds for bone tissue engineering: effect of hydroxyapatite composition on human fetal osteoblasts.* PloS one, 2014. **9**(1): p. e85871.
142. Ji, Y., X. Yu, and H. Zhu, *Fabrication of Mg Coating on PEEK and Antibacterial Evaluation for Bone Application.* Coatings, 2021. **11**(8): p. 1010.
143. Shannon, A. and I. Manolakis, *A Facile Route to Bio-Inspired Supramolecular Oligo (Ethylene Glycol) Catecholates.* Macromolecular Chemistry and Physics, 2019. **220**(3): p. 1800412.
144. Ma, Z., et al., *Biologically Modified Polyether Ether Ketone as Dental Implant Material.* Frontiers in Bioengineering and Biotechnology, 2020. **8**(1397).
145. Xian, P., et al., *Polydopamine (PDA) mediated nanogranular-structured titanium dioxide (TiO2) coating on polyetheretherketone (PEEK) for oral and maxillofacial implants application.* Surface and Coatings Technology, 2020. **401**: p. 126282.
146. Wiącek, A.E., et al., *Effect of low-temperature plasma on chitosan-coated PEEK polymer characteristics.* European Polymer Journal, 2016. **78**: p. 1-13.
147. Smitha, S., et al., *Synthesis of biocompatible hydrophobic silica–gelatin nano-hybrid by sol–gel process.* Colloids and surfaces B: Biointerfaces, 2007. **55**(1): p. 38-43.
148. Lee, B.P., J.L. Dalsin, and P.B. Messersmith, *Synthesis and gelation of DOPA-modified poly (ethylene glycol) hydrogels.* Biomacromolecules, 2002. **3**(5): p. 1038-1047.
149. Dalby, M.J., et al., *Optimizing HAPEX™ topography influences osteoblast response.* Tissue Engineering, 2002. **8**(3): p. 453-467.
150. *https://invibio.com/en/materials-solutions.* Access Date 15 September 2022.
151. Skinner, H., *Biominerals.* Mineralogical Magazine, 2005. **69**(5): p. 621-641.
152. Šupová, M., *Substituted hydroxyapatites for biomedical applications: a review.* Ceramics international, 2015. **41**(8): p. 9203-9231.
153. Capuccini, C., et al., *Strontium-substituted hydroxyapatite coatings synthesized by pulsed-laser deposition: in vitro osteoblast and osteoclast response.* Acta Biomaterialia, 2008. **4**(6): p. 1885-1893.

154. Rau, J.V., et al., *Physicochemical investigation of pulsed laser deposited carbonated hydroxyapatite films on titanium.* ACS applied materials & interfaces, 2009. **1**(8): p. 1813-1820.
155. Mróz, W., et al., *Structural studies of magnesium doped hydroxyapatite coatings after osteoblast culture.* Journal of Molecular Structure, 2010. **977**(1-3): p. 145-152.
156. Clemens, J., et al., *Healing of gaps around calcium phosphate-coated implants in trabecular bone of the goat.* Journal of Biomedical Materials Research: An Official Journal of The Society for Biomaterials and The Japanese Society for Biomaterials, 1997. **36**(1): p. 55-64.
157. Li, L., et al., *Comparison study of biomimetic strontium-doped calcium phosphate coatings by electrochemical deposition and air plasma spray: morphology, composition and bioactive performance.* Journal of Materials Science: Materials in Medicine, 2012. **23**(10): p. 2359-2368.
158. Xue, W., et al., *Preparation and cell–materials interactions of plasma sprayed strontium-containing hydroxyapatite coating.* Surface and Coatings technology, 2007. **201**(8): p. 4685-4693.
159. Boyd, A.R., et al., *Strontium-substituted hydroxyapatite coatings deposited via a co-deposition sputter technique.* Materials Science and Engineering: C, 2015. **46**: p. 290-300.
160. Pereiro, I., et al., *Pulsed laser deposition of strontium-substituted hydroxyapatite coatings.* Applied Surface Science, 2012. **258**(23): p. 9192-9197.
161. Ozeki, K., et al., *Characterization of Sr-substituted hydroxyapatite thin film by sputtering technique from mixture targets of hydroxyapatite and strontium apatite.* Bio-medical materials and engineering, 2014. **24**(2): p. 1447-1456.
162. Reginster, J.-Y., *Cardiac concerns associated with strontium ranelate.* Expert opinion on drug safety, 2014. **13**(9): p. 1209-1213.
163. Bolland, M.J. and A. Grey, *Ten years too long: strontium ranelate, cardiac events, and the European Medicines Agency.* Bmj, 2016. **354**.
164. Dorozhkin, S.V., *Calcium orthophosphate coatings, films and layers.* Progress in Biomaterials, 2012. **1**(1): p. 1.

165. Khandare, A.L., et al., *Health risk assessment of heavy metals and strontium in groundwater used for drinking and cooking in 58 villages of Prakasam district, Andhra Pradesh, India.* Environmental Geochemistry and Health, 2020. **42**(11): p. 3675-3701.
166. Musgrove, M., *The occurrence and distribution of strontium in US groundwater.* Applied Geochemistry, 2021. **126**: p. 104867.
167. Cohen-Solal, M., *Strontium overload and toxicity: impact on renal osteodystrophy.* Nephrol Dial Transplant, 2002. **17 Suppl 2**: p. 30-4.
168. Pathak, P. and D.K. Gupta, *Strontium contamination in the environment*. 2020: Springer.
169. Aimaiti, A., et al., *Low-dose strontium stimulates osteogenesis but high-dose doses cause apoptosis in human adipose-derived stem cells via regulation of the ERK1/2 signaling pathway.* Stem Cell Res Ther, 2017. **8**(1): p. 282.
170. Bogya, E.S., Z. Károly, and R. Barabás, *Atmospheric plasma sprayed silica–hydroxyapatite coatings on magnesium alloy substrates.* Ceramics International, 2015. **41**(4): p. 6005-6012.
171. Agnew, U.M. and T.L. Slesinger, *Zinc toxicity.* 2020.
172. Lee, J.-H., et al., *Cytotoxicity and anti-inflammatory effects of zinc ions and eugenol during setting of ZOE in immortalized human oral keratinocytes grown as three-dimensional spheroids.* Dental Materials, 2016. **32**(5): p. e93-e104.
173. Shen, X., et al., *Fabrication of magnesium/zinc-metal organic framework on titanium implants to inhibit bacterial infection and promote bone regeneration.* Biomaterials, 2019. **212**: p. 1-16.
174. Yu, Y., et al., *Multifunctions of dual Zn/Mg ion co-implanted titanium on osteogenesis, angiogenesis and bacteria inhibition for dental implants.* Acta biomaterialia, 2017. **49**: p. 590-603.
175. Prasad, A.S., *Zinc: an antioxidant and anti-inflammatory agent: role of zinc in degenerative disorders of aging.* Journal of Trace Elements in Medicine and Biology, 2014. **28**(4): p. 364-371.
176. Brauer, D.S., et al., *Benefits and drawbacks of zinc in glass ionomer bone cements.* Biomedical Materials, 2011. **6**(4): p. 045007.

177. Okada, M., et al., *Shareability of antibacterial and osteoblastic-proliferation activities of zinc-doped hydroxyapatite nanoparticles in vitro.* Journal of Biomedical Materials Research Part B: Applied Biomaterials, 2022. **110**(4): p. 799-805.
178. Aina, V., et al., *Cytotoxicity of zinc-containing bioactive glasses in contact with human osteoblasts.* Chemico-Biological Interactions, 2007. **167**(3): p. 207-218.
179. Barceloux, D.G., *Zinc.* J Toxicol Clin Toxicol, 1999. **37**(2): p. 279-92.
180. Su, Y., et al., *Enhanced cytocompatibility and antibacterial property of zinc phosphate coating on biodegradable zinc materials.* Acta biomaterialia, 2019. **98**: p. 174-185.
181. Wazir, S.M. and I. Ghobrial, *Copper deficiency, a new triad: anemia, leucopenia, and myeloneuropathy.* J Community Hosp Intern Med Perspect, 2017. **7**(4): p. 265-268.
182. Bianchi, M., et al., *Surface morphology, tribological properties and in vitro biocompatibility of nanostructured zirconia thin films.* Journal of Materials Science: Materials in Medicine, 2016. **27**(5): p. 96.
183. György, E., et al., *Biocompatible Mn2+-doped carbonated hydroxyapatite thin films grown by pulsed laser deposition.* Journal of Biomedical Materials Research Part A: An Official Journal of The Society for Biomaterials, The Japanese Society for Biomaterials, and The Australian Society for Biomaterials and the Korean Society for Biomaterials, 2004. **71**(2): p. 353-358.
184. Babilotte, J., et al., *3D printed polymer-mineral composite biomaterials for bone tissue engineering: Fabrication and characterization.* J Biomed Mater Res B Appl Biomater, 2019.
185. Rachmiel, A., et al., *Reconstruction of complex mandibular defects using integrated dental custom-made titanium implants.* Br J Oral Maxillofac Surg, 2017. **55**(4): p. 425-427.
186. Oh, J.-h., *Recent advances in the reconstruction of cranio-maxillofacial defects using computer-aided design/computer-aided manufacturing.* Maxillofacial Plastic and Reconstructive Surgery, 2018. **40**(1): p. 2.
187. Owusu, J.A. and K. Boahene, *Update of patient-specific maxillofacial implant.* Curr Opin Otolaryngol Head Neck Surg, 2015. **23**(4): p. 261-4.

188. Zhao, L., P.K. Patel, and M. Cohen, *Application of virtual surgical planning with computer assisted design and manufacturing technology to cranio-maxillofacial surgery.* Archives of plastic surgery, 2012. **39**(4): p. 309-316.
189. Bhatia, A. and A.K. Sehgal, *Additive manufacturing materials, methods and applications: A review.* Materials Today: Proceedings, 2021.
190. Yan, R., et al., *Electron beam melting in the fabrication of three-dimensional mesh titanium mandibular prosthesis scaffold.* Scientific reports, 2018. **8**(1): p. 750.
191. Yan, C., et al., *Ti–6Al–4V triply periodic minimal surface structures for bone implants fabricated via selective laser melting.* Journal of the mechanical behavior of biomedical materials, 2015. **51**: p. 61-73.
192. Yánez, A., et al., *Gyroid porous titanium structures: a versatile solution to be used as scaffolds in bone defect reconstruction.* Materials & Design, 2018. **140**: p. 21-29.
193. Larosa, M.A., et al., *Microstructural and mechanical characterization of a custom-built implant manufactured in titanium alloy by direct metal laser sintering.* Advances in Mechanical Engineering, 2014. **6**: p. 945819.
194. El-Hajje, A., et al., *Physical and mechanical characterisation of 3D-printed porous titanium for biomedical applications.* Journal of Materials Science: Materials in Medicine, 2014. **25**(11): p. 2471-2480.
195. Mishinov, S., et al. *Cranioplasty with individual titanium implants*. in *AIP Conference Proceedings*. 2017. AIP Publishing.
196. Park, E.-K., et al., *Cranioplasty enhanced by three-dimensional printing: custom-made three-dimensional-printed titanium implants for skull defects.* Journal of Craniofacial Surgery, 2016. **27**(4): p. 943-949.
197. Carneiro, O.S., A.F. Silva, and R. Gomes, *Fused deposition modeling with polypropylene.* Materials & Design, 2015. **83**: p. 768-776.
198. Shankhwar, N., et al., *Chapter 24 - Tissue engineered products—Translational avenues*, in *Tissue Engineering*, C.P. Sharma, et al., Editors. 2022, Academic Press. p. 575-625.
199. Jafari, A., et al., *Latest Advances in 3D Bioprinting of Cardiac Tissues.* Advanced Materials Technologies, 2022: p. 2101636.

200. McIlwraith, C.W., et al., *27 - Equine Joint Disease: Present and Future Directions in Research*, in *Joint Disease in the Horse (Second Edition)*, C.W. McIlwraith, et al., Editors. 2016, W.B. Saunders: Edinburgh. p. 376-398.
201. Bourell, D., et al., *Fused deposition modeling of patient-specific polymethylmethacrylate implants.* Rapid Prototyping Journal, 2010.
202. Kempin, W., et al., *Assessment of different polymers and drug loads for fused deposition modeling of drug loaded implants.* European Journal of Pharmaceutics and Biopharmaceutics, 2017. **115**: p. 84-93.
203. Kang, H.-W., et al., *A 3D bioprinting system to produce human-scale tissue constructs with structural integrity.* Nature biotechnology, 2016. **34**(3): p. 312.
204. Obregon, F., et al., *Three-dimensional bioprinting for regenerative dentistry and craniofacial tissue engineering.* Journal of Dental Research, 2015. **94**(9_suppl): p. 143S-152S.
205. Roskies, M., et al., *Improving PEEK bioactivity for craniofacial reconstruction using a 3D printed scaffold embedded with mesenchymal stem cells.* Journal of biomaterials applications, 2016. **31**(1): p. 132-139.
206. Parthasarathy, J., *3D modeling, custom implants and its future perspectives in craniofacial surgery.* Annals of maxillofacial surgery, 2014. **4**(1): p. 9.
207. Parthasarathy, J., et al., *Mechanical evaluation of porous titanium (Ti6Al4V) structures with electron beam melting (EBM).* Journal of the mechanical behavior of biomedical materials, 2010. **3**(3): p. 249-259.
208. Harrysson, O., et al. *Evaluation of titanium implant components directly fabricated through electron beam melting technology*. in *Materials and Processes for Medical Devices Conference, Boston*. 2006.
209. Chrcanovic, B.R., T. Albrektsson, and A. Wennerberg, *Platform switch and dental implants: A meta-analysis.* Journal of dentistry, 2015. **43**(6): p. 629-646.
210. Sinn, D.P., J.E. Cillo Jr, and B.A. Miles, *Stereolithography for craniofacial surgery.* Journal of Craniofacial Surgery, 2006. **17**(5): p. 869-875.
211. Zeng, Y., et al., *3D printing of hydroxyapatite scaffolds with good mechanical and biocompatible properties by digital light processing.* Journal of materials science, 2018. **53**(9): p. 6291-6301.

212. Grant, G.T., *Direct digital manufacturing.* Clinical Applications of Digital Dental Technology, 2015: p. 41-56.
213. Gonzalez, J., et al., *Characterization of ceramic components fabricated using binder jetting additive manufacturing technology.* Ceramics International, 2016. **42**(9): p. 10559-10564.
214. Gokuldoss, P.K., S. Kolla, and J. Eckert, *Additive manufacturing processes: Selective laser melting, electron beam melting and binder jetting—Selection guidelines.* Materials, 2017. **10**(6): p. 672.
215. Ionita, C.N., et al. *Challenges and limitations of patient-specific vascular phantom fabrication using 3D Polyjet printing*. in *Medical Imaging 2014: Biomedical Applications in Molecular, Structural, and Functional Imaging*. 2014. International Society for Optics and Photonics.
216. Gu, Q., et al., *Three-dimensional bio-printing.* Science China Life Sciences, 2015. **58**(5): p. 411-419.
217. Torstrick, F.B., et al., *Getting PEEK to Stick to Bone: The Development of Porous PEEK for Interbody Fusion Devices.* Techniques in orthopaedics (Rockville, Md.), 2017. **32**(3): p. 158-166.
218. Scotchford, C.A., et al., *Use of a novel carbon fibre composite material for the femoral stem component of a THR system: in vitro biological assessment.* Biomaterials, 2003. **24**(26): p. 4871-4879.
219. Liao, C., Y. Li, and S.C. Tjong, *Polyetheretherketone and Its Composites for Bone Replacement and Regeneration.* Polymers, 2020. **12**(12): p. 2858.
220. Panayotov, I.V., et al., *Polyetheretherketone (PEEK) for medical applications.* Journal of Materials Science: Materials in Medicine, 2016. **27**(7): p. 118.
221. Keaveny, T.M. and W.C. Hayes, *Mechanical properties of cortical and trabecular bone.* Bone, 1993. **7**: p. 285-344.
222. Seal, B., T. Otero, and A. Panitch, *Polymeric biomaterials for tissue and organ regeneration.* Materials Science and Engineering: R: Reports, 2001. **34**(4-5): p. 147-230.
223. Zioupos, P. and J. Currey, *Changes in the stiffness, strength, and toughness of human cortical bone with age.* Bone, 1998. **22**(1): p. 57-66.

224. Lee, W.T., et al., *Stress shielding and fatigue limits of poly-ether-ether-ketone dental implants.* Journal of Biomedical Materials Research Part B: Applied Biomaterials, 2012. **100**(4): p. 1044-1052.
225. Rahmitasari, F., et al., *PEEK with reinforced materials and modifications for dental implant applications.* Dentistry journal, 2017. **5**(4): p. 35.
226. Wang, L., et al., *Polyetheretherketone/nano-fluorohydroxyapatite composite with antimicrobial activity and osseointegration properties.* Biomaterials, 2014. **35**(25): p. 6758-6775.
227. Wong, K., et al., *Mechanical properties and in vitro response of strontium-containing hydroxyapatite/polyetheretherketone composites.* Biomaterials, 2009. **30**(23-24): p. 3810-3817.
228. Lee, J.H., et al., *In vitro and in vivo evaluation of the bioactivity of hydroxyapatite-coated polyetheretherketone biocomposites created by cold spray technology.* Acta biomaterialia, 2013. **9**(4): p. 6177-6187.
229. Kim, I.Y., et al., *Bioactive composites consisting of PEEK and calcium silicate powders.* J Biomater Appl, 2009. **24**(2): p. 105-18.
230. Kuo, M., et al., *PEEK composites reinforced by nano-sized SiO2 and Al2O3 particulates.* Materials Chemistry and Physics, 2005. **90**(1): p. 185-195.
231. Wu, X., et al., *Nano-TiO2/PEEK bioactive composite as a bone substitute material: in vitro and in vivo studies.* International journal of nanomedicine, 2012. **7**: p. 1215.
232. Cuan-Urquizo, E., et al., *Characterization of the Mechanical Properties of FFF Structures and Materials: A Review on the Experimental, Computational and Theoretical Approaches.* Materials, 2019. **12**(6): p. 895.
233. Rahman, K.M., T. Letcher, and R. Reese. *Mechanical properties of additively manufactured peek components using fused filament fabrication*. in *ASME 2015 International Mechanical Engineering Congress and Exposition*. 2015. American Society of Mechanical Engineers.
234. Berretta, S., K. Evans, and O. Ghita, *Additive manufacture of PEEK cranial implants: Manufacturing considerations versus accuracy and mechanical performance.* Materials & Design, 2018. **139**: p. 141-152.

235. Roskies, M.G., et al., *Three-dimensionally printed polyetherketoneketone scaffolds with mesenchymal stem cells for the reconstruction of critical-sized mandibular defects.* The Laryngoscope, 2017. **127**(11): p. E392-E398.
236. Wu, W., et al., *Influence of layer thickness and raster angle on the mechanical properties of 3D-printed PEEK and a comparative mechanical study between PEEK and ABS.* Materials, 2015. **8**(9): p. 5834-5846.
237. Rodzeń, K., et al., *The Direct 3D Printing of Functional PEEK/Hydroxyapatite Composites via a Fused Filament Fabrication Approach.* Polymers, 2021. **13**(4): p. 545.
238. Zheng, J., et al., *Effects of printing path and material components on mechanical properties of 3D-printed polyether-ether-ketone/hydroxyapatite composites.* Journal of the Mechanical Behavior of Biomedical Materials, 2021. **118**: p. 104475.
239. Tan, K.H., et al., *Scaffold development using selective laser sintering of polyetheretherketone–hydroxyapatite biocomposite blends.* Biomaterials, 2003. **24**(18): p. 3115-3123.
240. Tan, K., et al., *Fabrication and characterization of three-dimensional poly (ether-ether-ketone)/-hydroxyapatite biocomposite scaffolds using laser sintering.* Proceedings of the Institution of Mechanical Engineers, Part H: Journal of Engineering in Medicine, 2005. **219**(3): p. 183-194.
241. Vaezi, M. and S. Yang, *A novel bioactive PEEK/HA composite with controlled 3D interconnected HA network.* International journal of Bioprinting, 2015. **1**(1): p. 66-76.
242. Williams, D., *Polyetheretherketone for long-term implantable devices.* Medical device technology, 2008. **19**(1): p. 8, 10-1.
243. Ma, R. and T. Tang, *Current strategies to improve the bioactivity of PEEK.* International journal of molecular sciences, 2014. **15**(4): p. 5426-5445.
244. Briem, D., et al., *Response of primary fibroblasts and osteoblasts to plasma treated polyetheretherketone (PEEK) surfaces.* Journal of Materials Science: Materials in Medicine, 2005. **16**(7): p. 671-677.
245. Wang, H., et al., *Mechanical and biological characteristics of diamond-like carbon coated poly aryl-ether-ether-ketone.* Biomaterials, 2010. **31**(32): p. 8181-8187.
246. Barkarmo, S., et al., *Nano-hydroxyapatite-coated PEEK implants: a pilot study in rabbit bone.* Journal of Biomedical Materials Research Part A, 2013. **101**(2): p. 465-471.

247. Hahn, B.-D., et al., *Osteoconductive hydroxyapatite coated PEEK for spinal fusion surgery.* Applied Surface Science, 2013. **283**: p. 6-11.
248. Rabiei, A. and S. Sandukas, *Processing and evaluation of bioactive coatings on polymeric implants.* Journal of Biomedical Materials Research Part A, 2013. **101**(9): p. 2621-2629.
249. Yao, C., D. Storey, and T.J. Webster, *Nanostructured metal coatings on polymers increase osteoblast attachment.* International journal of nanomedicine, 2007. **2**(3): p. 487.
250. Cook, S. and A. Rust-Dawicki, *Preliminary evaluation of titanium-coated PEEK dental implants.* The Journal of oral implantology, 1995. **21**(3): p. 176-181.
251. Han, C.-M., et al., *The electron beam deposition of titanium on polyetheretherketone (PEEK) and the resulting enhanced biological properties.* Biomaterials, 2010. **31**(13): p. 3465-3470.
252. Ha, S.-W., et al., *NaOH treatment of vacuum-plasma-sprayed titanium on carbon fibre-reinforced poly (etheretherketone).* Journal of Materials Science: Materials in Medicine, 1997. **8**(12): p. 881-886.
253. Dictionary, https://www.dictionary.com/browse/in-vitro.
254. Ma, R., et al., *Mechanical performance and in vivo bioactivity of functionally graded PEEK–HA biocomposite materials.* Journal of sol-gel science and technology, 2014. **70**(3): p. 339-345.
255. Ma, R., et al., *Preparation, characterization, in vitro bioactivity, and cellular responses to a polyetheretherketone bioactive composite containing nanocalcium silicate for bone repair.* ACS applied materials & interfaces, 2014. **6**(15): p. 12214-12225.
256. Rodzeń, K., et al., *The Surface Characterisation of Fused Filament Fabricated (FFF) 3D Printed PEEK/Hydroxyapatite Composites.* Polymers, 2021. **13**(18): p. 3117.
257. Han, X., et al., *An In Vitro Study of Osteoblast Response on Fused-Filament Fabrication 3D Printed PEEK for Dental and Cranio-Maxillofacial Implants.* Journal of clinical medicine, 2019. **8**(6): p. 771.
258. Zhao, M., et al., *Response of human osteoblast to n-HA/PEEK—quantitative proteomic study of bio-effects of nano-hydroxyapatite composite.* Scientific reports, 2016. **6**: p. 22832.

259. Sikder, P., et al., *Bioactive amorphous magnesium phosphate-polyetheretherketone composite filaments for 3D printing.* Dental Materials, 2020. **36**(7): p. 865-883.
260. Chan, K.W., et al., *Preparation of polyetheretherketone composites with nanohydroxyapatite rods and carbon nanofibers having high strength, good biocompatibility and excellent thermal stability.* RSC advances, 2016. **6**(23): p. 19417-19429.
261. Roy, P. and R. Sailaja, *Mechanical, thermal and bio-compatibility studies of PAEK-hydroxyapatite nanocomposites.* Journal of the mechanical behavior of biomedical materials, 2015. **49**: p. 1-11.
262. Wong, K.L., et al., *Mechanical properties and in vitro response of strontium-containing hydroxyapatite/polyetheretherketone composites.* Biomaterials, 2009. **30**(23): p. 3810-3817.
263. Abu Bakar, M.S., et al., *Tensile properties, tension–tension fatigue and biological response of polyetheretherketone–hydroxyapatite composites for load-bearing orthopedic implants.* Biomaterials, 2003. **24**(13): p. 2245-2250.
264. Hahn, B.-D., et al., *Osteoconductive hydroxyapatite coated PEEK for spinal fusion surgery.* Applied Surface Science, 2013. **283**: p. 6-11.
265. Ma, R., et al., *Mechanical properties and in vivo study of modified-hydroxyapatite/polyetheretherketone biocomposites.* Materials Science and Engineering: C, 2017. **73**: p. 429-439.
266. Mahjoubi, H., et al., *Surface phosphonation enhances hydroxyapatite coating adhesion on polyetheretherketone and its osseointegration potential.* Acta Biomaterialia, 2017. **47**: p. 149-158.
267. Lowry, N., et al., *Synthesis and characterisation of nanophase hydroxyapatite co-substituted with strontium and zinc.* Ceramics International, 2018. **44**(7): p. 7761-7770.
268. Eufinger, H., et al., *Reconstruction of craniofacial bone defects with individual alloplastic implants based on CAD/CAM-manipulated CT-data.* Journal of Cranio-Maxillofacial Surgery, 1995. **23**(3): p. 175-181.
269. Kokubo, T. and H. Takadama, *How useful is SBF in predicting in vivo bone bioactivity?* Biomaterials, 2006. **27**(15): p. 2907-2915.

270. Kokubo, T. and H. Takadama, *Implants for Surgery–In vitro Evaluation for Apatite-Forming Ability of Implant Materials; ISO 23317.* International Organization for Standardization (ISO): Geneva, Switzerland, 2012. **31**: p. 1996-1944.
271. Mathieu, L., P.-E. Bourban, and J.-A. Månson, *Processing of homogeneous ceramic/polymer blends for bioresorbable composites.* Composites Science and Technology, 2006. **66**(11-12): p. 1606-1614.
272. Muralithran, G. and S. Ramesh, *The effects of sintering temperature on the properties of hydroxyapatite.* Ceramics International, 2000. **26**(2): p. 221-230.
273. Scalera, F., et al., *Sintering of magnesium-strontium doped hydroxyapatite nanocrystals: Towards the production of 3D biomimetic bone scaffolds.* Journal of Biomedical Materials Research Part A, 2020. **108**(3): p. 633-644.
274. Zeng, H. and W.R. Lacefield, *XPS, EDX and FTIR analysis of pulsed laser deposited calcium phosphate bioceramic coatings: the effects of various process parameters.* Biomaterials, 2000. **21**(1): p. 23-30.
275. Lian, H., L. Zhang, and Z. Meng, *Biomimetic hydroxyapatite/gelatin composites for bone tissue regeneration: Fabrication, characterization, and osteogenic differentiation in vitro.* Materials & Design, 2018. **156**: p. 381-388.
276. Goranova, K.L., A.K. Kattenhøj Sloth Overgaard, and I. Gitsov, *Hydroxyapatite-poly(d,l-lactide) Nanografts. Synthesis and Characterization as Bone Cement Additives.* Molecules, 2021. **26**(2): p. 424.
277. Akindoyo, J.O., et al., *Characterization and elemental quantification of natural hydroxyapatite produced from cow bone.* Chemical Engineering & Technology, 2019. **42**(9): p. 1805-1815.
278. Ahmad, A., et al., *Stability of Amorphous PEEK in Organic Solvents.* Journal of the Chemical Society of Pakistan, 2018. **40**(4): p. 810-818.
279. Coates, J., *Interpretation of infrared spectra, a practical approach.* Encyclopedia of analytical chemistry: applications, theory and instrumentation, 2006.
280. Díez-Pascual, A.M. and A.L. Díez-Vicente, *Poly (3-hydroxybutyrate)/ZnO bionanocomposites with improved mechanical, barrier and antibacterial properties.* International journal of molecular sciences, 2014. **15**(6): p. 10950-10973.

281. El Boujaady, H., et al., *Adsorption of a textile dye on synthesized calcium deficient hydroxyapatite (CDHAp): kinetic and thermodynamic studies.* J. Mater. Environ. Sci, 2016. **7**(11): p. 4049-4063.
282. Siddiqi, S.A., et al., *Mesenchymal stem cell (MSC) viability on PVA and PCL polymer coated hydroxyapatite scaffolds derived from cuttlefish.* RSC Advances, 2016. **6**(39): p. 32897-32904.
283. Pantasri, T., S. Seet, and P. Suwanna. *Preparation of strontium-and/or zinc-doped hydroxyapatite nanoparticles and their polycaprolactone composite fibrous scaffolds*. in *Journal of Physics: Conference Series*. 2017. IOP Publishing.
284. Norhidayu, D., I. Sopyan, and S. Ramesh. *Development of zinc doped hydroxyapatite for bone implant applications*. in *ICCBT 2008 Conference*. 2008.
285. Bianchi, M., et al., *Strontium doped calcium phosphate coatings on poly (etheretherketone)(PEEK) by pulsed electron deposition.* Surface and Coatings Technology, 2017. **319**: p. 191-199.
286. Meenan, B., et al., *Evaluation of the quality of calcium phosphate bioceramics via a study of the effects of thermal processing.* Key Engineering Materials, 2001. **192**.
287. Roveri, N., B. Palazzo, and M. Iafisco, *The role of biomimetism in developing nanostructured inorganic matrices for drug delivery.* Expert Opinion on Drug Delivery, 2008. **5**(8): p. 861-877.
288. Ramesh, S., et al., *Characterization of biogenic hydroxyapatite derived from animal bones for biomedical applications.* Ceramics International, 2018. **44**(9): p. 10525-10530.
289. Khorasani, F., M. Khavarpour, and M.S. Lamuki, *The study of morphology and grain size of hydroxyapatite/zeolite nanocomposite using SEM and TEM analyses.* Specialty Journal of Chemistry, 2019. **4**(1): p. 1-8.
290. Bakan, F., *A Systematic Study of the Effect of pH on the Initialization of Ca-deficient Hydroxyapatite to β-TCP Nanoparticles.* Materials, 2019. **12**(3): p. 354.
291. Kavitha, M., et al., *Solution combustion synthesis and characterization of strontium substituted hydroxyapatite nanocrystals.* Powder technology, 2014. **253**: p. 129-137.
292. El Idrissi, B.C., et al., *A novel method to synthesize nanocrystalline hydroxyapatite: Characterization with x-ray diffraction and infrared spectroscopy.* IOSR Journal of Applied Chemistry, 2014. **7**(5): p. 107-112.

293. Boyd, A.R., et al., *The influence of target stoichiometry on early cell adhesion of co-sputtered calcium–phosphate surfaces.* Journal of Materials Science: Materials in Medicine, 2013. **24**(12): p. 2845-2861.
294. Gebhardt, A., J. Kessler, and L. Thurn, *3D-Drucken: Grundlagen und Anwendungen des additive manufacturing (AM)*. 2016: Carl Hanser Verlag GmbH Co KG.
295. Diegel, O., A. Nordin, and D. Motte, *A practical guide to design for additive manufacturing*. 2019: Springer.
296. Comelli, C.A., et al., *PEEK filament characteristics before and after extrusion within fused filament fabrication process.* Journal of Materials Science, 2022. **57**(1): p. 766-788.
297. Spoerk, M., et al., *Parametric optimization of intra-and inter-layer strengths in parts produced by extrusion-based additive manufacturing of poly (lactic acid).* Journal of applied polymer science, 2017. **134**(41): p. 45401.
298. Cardona, C., A. Curdes, and A. Isaacs, *Effects of Filament Diameter Tolerances in Fused Filament Fabrication.* IU Journal of Undergraduate Research, 2016. **2**: p. 44-47.
299. Lai, W., et al., *Hydroxyapatite/polyetheretherketone nanocomposites for selective laser sintering: Thermal and mechanical performances.* e-Polymers, 2020. **20**(1): p. 542-549.
300. Hay, J. and D. Kemmish, *Thermal decomposition of poly (aryl ether ketones).* Polymer, 1987. **28**(12): p. 2047-2051.
301. Perng, L., C. Tsai, and Y. Ling, *Mechanism and kinetic modelling of PEEK pyrolysis by TG/MS.* Polymer, 1999. **40**(26): p. 7321-7329.
302. Patel, P., et al., *Mechanism of thermal decomposition of poly(ether ether ketone) (PEEK) from a review of decomposition studies.* Polymer Degradation and Stability, 2010. **95**(5): p. 709-718.
303. Meenan, B., C. McClorey, and M. Akay, *Thermal analysis studies of poly (etheretherketone)/hydroxyapatite biocomposite mixtures.* Journal of Materials Science: Materials in Medicine, 2000. **11**(8): p. 481-489.
304. Alam, F., et al., *Additively manufactured polyetheretherketone (PEEK) with carbon nanostructure reinforcement for biomedical structural applications.* Advanced Engineering Materials, 2020. **22**(10): p. 2000483.

305. Hao, L., et al., *Enhancing the mechanical performance of poly (ether ether ketone)/zinc oxide nanocomposites to provide promising biomaterials for trauma and orthopedic implants.* RSC advances, 2018. **8**(48): p. 27304-27317.
306. Dey, S.K., et al., *Reversing and non-reversing effects of PEEK-HA composites on tuning cooling rate during crystallization.* Journal of Polymer Research, 2019. **26**(12): p. 1-16.
307. Seipenbusch, M., et al. *Interparticle forces in nanoparticle agglomerates*. in *Austria, Salzburg: Proceedings of European Aerosol Conference*. 2007.
308. Gosens, I., et al., *Impact of agglomeration state of nano- and submicron sized gold particles on pulmonary inflammation.* Part Fibre Toxicol, 2010. **7**(1): p. 37.
309. Fang, L., Y. Yan, and O. Agarwal, *Effects of Environmental Temperature and Humidity on the Geometry and Strength of Polycarbonate Specimens Prepared by Fused Filament Fabrication.* 2020. **13**(19).
310. Golbang, A., et al., *Production and characterization of PEEK/IF-WS2 nanocomposites for additive manufacturing: Simultaneous improvement in processing characteristics and material properties.* Additive Manufacturing, 2020. **31**: p. 100920.
311. Jonas, A. and R. Legras, *Thermal stability and crystallization of poly(aryl ether ether ketone).* Polymer, 1991. **32**(15): p. 2691-2706.
312. Temprom, L., et al., *Bioactivity, cytotoxicity and antibacterial evaluation of undoped, Zn-doped, Sr-doped, and Zn/Sr-codoped hydroxyapatites synthesized by a sol-gel method.* Chiang Mai J. Sci., 2016. **43**: p. 1-11.
313. Liu, J., et al., *The regulating effect of trace elements Si, Zn and Sr on mineralization of gelatin-hydroxyapatite electrospun fiber.* Colloids and Surfaces B: Biointerfaces, 2021. **204**: p. 111822.
314. Başţan, F.E., *Fabrication and characterization of an electrostatically bonded PEEK-Hydroxyapatite composites for biomedical applications.* Journal of Biomedical Materials Research Part B: Applied Biomaterials, 2020. **108**(6): p. 2513-2527.
315. Rego, B.T., et al., *Mechanical properties and stem cell adhesion of injection-molded poly (ether ether ketone) and hydroxyapatite nanocomposites.* Journal of Applied Polymer Science, 2015. **132**(14).

316. Ma, R. and D. Guo, *Evaluating the bioactivity of a hydroxyapatite-incorporated polyetheretherketone biocomposite.* Journal of orthopaedic surgery and research, 2019. **14**(1): p. 1-13.
317. Singhal, A., et al., *On nanoparticle aggregation during vapor phase synthesis.* Nanostructured materials, 1999. **11**(4): p. 545-552.
318. Elawadly, T., et al., *Can PEEK be an implant material? Evaluation of surface topography and wettability of filled versus unfilled PEEK with different surface roughness.* Journal of Oral Implantology, 2017. **43**(6): p. 456-461.
319. Huang, R., et al., *Sulfonation of poly (ether ether ketone)(PEEK): kinetic study and characterization.* Journal of applied polymer science, 2001. **82**(11): p. 2651-2660.
320. De Gennes, P.-G., *Wetting: statics and dynamics.* Reviews of modern physics, 1985. **57**(3): p. 827.
321. Surmenev, R.A., M.A. Surmeneva, and A.A. Ivanova, *Significance of calcium phosphate coatings for the enhancement of new bone osteogenesis – A review.* Acta Biomaterialia, 2014. **10**(2): p. 557-579.
322. Manzoor, F., et al., *3D printed PEEK/HA composites for bone tissue engineering applications: Effect of material formulation on mechanical performance and bioactive potential.* Journal of the Mechanical Behavior of Biomedical Materials, 2021. **121**: p. 104601.
323. Kaygili, O., et al., *The effect of simulating body fluid on the structural properties of hydroxyapatite synthesized in the presence of citric acid.* Progress in Biomaterials, 2016. **5**(3): p. 173-182.
324. Ghomi, H., M. Fathi, and H. Edris, *Preparation of nanostructure hydroxyapatite scaffold for tissue engineering applications.* Journal of sol-gel science and technology, 2011. **58**(3): p. 642-650.
325. Shuai, C., et al., *Characterization and bioactivity evaluation of (polyetheretherketone/polyglycolicacid)-hydroyapatite scaffolds for tissue regeneration.* Materials, 2016. **9**(11): p. 934.
326. Jeyachandran, P., et al., *Mechanical behaviour of additively manufactured bioactive glass/high density polyethylene composites.* Journal of the Mechanical Behavior of Biomedical Materials, 2020. **108**: p. 103830.

327. Hench, L.L., *An introduction to bioceramics*. Vol. 1. 1993: World scientific.
328. Delille, R., et al., *Experimental study of the bone behaviour of the human skull bone for the development of a physical head model.* International Journal of Crashworthiness, 2007. **12**(2): p. 101-108.
329. Xie, Z., et al., *3D Bioprinting in Tissue Engineering for Medical Applications: The Classic and the Hybrid.* Polymers, 2020. **12**(8): p. 1717.
330. Wang, L., et al., *Mechanical properties and microstructure of polyetheretherketone–hydroxyapatite nanocomposite materials.* Materials Letters, 2010. **64**(20): p. 2201-2204.
331. Kokubo, T., *Bioactive glass ceramics: properties and applications.* Biomaterials, 1991. **12**(2): p. 155-163.
332. Stanislavov, A.S., et al., *Structural features of hydroxyapatite and carbonated apatite formed under the influence of ultrasound and microwave radiation and their effect on the bioactivity of the nanomaterials.* Ultrasonics Sonochemistry, 2018. **42**: p. 84-96.
333. Ma, R., et al., *Characterization of in situ synthesized hydroxyapatite/polyetheretherketone composite materials.* Materials Letters, 2012. **71**: p. 117-119.
334. Meyers, M.A., et al., *Biological materials: structure and mechanical properties.* Progress in Materials Science, 2008. **53**(1): p. 1-206.
335. Oladapo, B.I., et al., *3D printing of PEEK–cHAp scaffold for medical bone implant.* Bio-Design and Manufacturing, 2020: p. 1-16.
336. Ji, X.L., et al., *Tensile modulus of polymer nanocomposites.* Polymer Engineering & Science, 2002. **42**(5): p. 983-993.
337. Humbert, S., et al., *A re-examination of the elastic modulus dependence on crystallinity in semi-crystalline polymers.* Polymer, 2011. **52**(21): p. 4899-4909.
338. Hughes, E.A. and L.M. Grover, *Characterisation of a novel poly (ether ether ketone)/calcium sulphate composite for bone augmentation.* Biomaterials research, 2017. **21**(1): p. 1-11.
339. Fan, D., U. Staufer, and A. Accardo, *Engineered 3D polymer and hydrogel microenvironments for cell culture applications.* Bioengineering, 2019. **6**(4): p. 113.

340. Wang, P., et al., *Effects of printing parameters of fused deposition modeling on mechanical properties, surface quality, and microstructure of PEEK.* Journal of Materials Processing Technology, 2019. **271**: p. 62-74.
341. Wu, W., et al., *Manufacture and thermal deformation analysis of semicrystalline polymer polyether ether ketone by 3D printing.* Materials Research Innovations, 2014. **18**(sup5): p. S5-12-S5-16.
342. Geng, P., et al., *Effect of thermal processing and heat treatment condition on 3D printing PPS properties.* Polymers, 2018. **10**(8): p. 875.
343. Cicala, G., et al., *Engineering thermoplastics for additive manufacturing: A critical perspective with experimental evidence to support functional applications.* Journal of applied biomaterials & functional materials, 2017. **15**(1): p. 10-18.
344. Wang, S., et al., *The crystal structure and drawing-induced polymorphism in poly (aryl ether ketone) s, 2. Poly (ether ether ketone ketone), PEEKK.* Macromolecular Chemistry and Physics, 1997. **198**(4): p. 969-982.
345. Saha, S. and W. Hayes, *Tensile impact properties of human compact bone.* Journal of biomechanics, 1976. **9**(4): p. 243-251.